IRAQI JOURNAL OF APPLIED PHYSICS

The *Iraqi Journal of Applied Physics (IJAP)* is a peer reviewed journal of high quality devoted to the publication of original research papers from applied physics and their broad range of applications. IJAP publishes quality original research papers, comprehensive review articles, survey articles, book reviews, dissertation abstracts in physics and its applications in the broadest sense. It is intended that the journal may act as an interdisciplinary forum for Physics and its applications. Innovative applications and material that brings together diverse areas of Physics are particularly welcome. Review articles in selected areas are published from time to time. It aims to disseminate knowledge; provide a learned reference in the field; and establish channels of communication between academic and research experts, policy makers and executives in industry, commerce and investment institutions. IJAP is a quarterly specialized periodical dedicated to publishing original papers, letters and reviews in: Applied & Nonlinear Optics, Applied Mechanics & Thermodynamics, Digital & Optical Communications, Electronic Materials & Devices, Laser Physics & Applications, Plasma Physics & Applications, Quantum Physics & Spectroscopy, Semiconductors & Optoelectronics, Solid State Physics & Applications, Alternative & Renewable Energy, and Environmental Science & Technology.

ISSN (Print): 1813-2065, ISSN (Online): 2309-1673

Editorial Office:
P. O. Box 88052, Baghdad 12631, IRAQ
Website: www.iraqiphysicsjournal.com
Emails: info@iraqiphysicsjournal.com, editor_ijap@yahoo.co.uk, ijap.editor@gmail.com,

SPONSORED AND PUBLISHED BY
AMERICAN QUALITY FOR SCIENTIFIC PUBLISHING INC.
1479 South De Gaulle Ct, Aurora, CO 80018, United States

IRAQI JOURNAL OF APPLIED PHYSICS

ISSN (Print): 1813-2065, ISSN (Online): 2309-1673

INSTRUCTIONS TO AUTHORS

CONTRIBUTIONS

Contributions to be published in this journal should be original research works, i.e., those not already published or submitted for publication elsewhere, individual papers or letters to editor.
Manuscripts should be submitted to the editor at the mailing address:

Iraqi Journal of Applied Physics, Editorial Board, P. O. Box 88052, Baghdad 12631, IRAQ
Website: www.iraqiphysicsjournal.com
Email: info@iraqiphysicsjournal.com, editor_ijap@yahoo.co.uk, ijap.editor@gmail.com

MANUSCRIPTS

Two hard copies with soft Word copy on a CD or DVD should be submitted to Editor in the following configuration:

- **One-column** Double-spaced one-side A4 size with 2.5 cm margins of all sides
- Times New Roman font (16pt bold for title, 14pt bold for names, 12pt bold for headings, 12pt regular for text)
- Manuscripts presented in English only are accepted.
- English abstract not exceed 150 words
- 4 keywords (at least) should be maintained on (PACS preferred)
- Author(s) should express all quantities in SI units
- Equations should be written in equation form (*italic* and symbolic) NOT in plain text
- Tables and Figures should be separated from text and placed in new pages after the references
- Charts should be indicated by the software used for generating them (e.g., Excel, MATLAB, Grapher, etc.)
- Figures and diagrams can be submitted in original colored forms for assessment and they will be returned to authors after provide printable copies
- Only original or high-resolution scanner photos are accepted
- For electronic submission, articles should be formatted with MS-Word software.

AUTHOR NAMES AND AFFILIATIONS

It is IJAP policy that all those who have participated significantly in the technical aspects of a paper be recognized as co-authors or cited in the acknowledgments. In the case of a paper with more than one author, correspondence concerning the paper will be sent to the first author unless staff is advised otherwise.
Author name should consist of first name, middle initial, last name. The author affiliation should consist of the following, as applicable, in the order noted:
- Company or college (with department name or company division), Postal address, City, Governorate or State, zip code, Country name, contacting telephone number, and e-mail

REFERENCES

The references should be brought at the end of the article, and numbered in the order of their appearance in the paper. The reference list should be cited in accordance with the following examples:
[1] X. Ning, R. Benford and M.R. Lovell, "On the Sliding Friction Characteristics of Unidirectional Continuous FRP Composites", *J. Tribol. Func. Mater.*, 124(1) (2002) 5-13.
[2] M. Barnes, "Stresses in Solenoids", *J. Appl. Phys.*, 48(5) (2001) 2000–2008.
[3] J. Jones, **"Contact Mechanics"**, Cambridge University Press (Cambridge, UK) (2000), Ch.6, p.56.
[4] Y. Lee, S.A. Korpela and R. Horne, "Structure of Multi-Cellular Natural Convection in a Tall Vertical Annulus", Proceedings of 7th International Heat Transfer Conference, U. Grigul et al., eds., Hemisphere (Washington DC), 2 (1982) 221–226.
[5] M. Hashish, "Waterjet Technology Development", High Pressure Technology, PVP-Vol. 406 (2000) 135-140.
[6] D.W. Watson, "Thermodynamic Analysis", ASME Paper No. 97-GT-288 (1997).
[7] C.Y. Tung, "Evaporative Heat Transfer in the Contact Line of a Mixture", Ph.D. thesis, Rensselaer Polytechnic Institute, Troy, NY (1982).

PROOFS

Authors will receive proofs of papers and are requested to return one corrected copy as a WORD file on a compact disc (CD) or by email. New materials inserted in the original text without Editor's permission may cause rejection of paper unless the handling editor is informed.

COPYRIGHT FORM

Author(s) will be asked to sign the IJAP Copyright Form and hence transfer copyrights of the article to the Journal soon after acceptance of it. This will ensure the widest possible dissemination of information.

OFFPRINTS

Authors will receive electronic offprint free of charge and any additional reprints can be ordered.

SUBSCRIPTION AND ORDERS

Annual fees (4 issues per year) of subscription are:
50 US$ for individuals inside Iraq; **200** US$ for institutions inside Iraq;
100 US$ for individuals abroad; **300** US$ for institutions abroad.

IRAQI JOURNAL OF APPLIED PHYSICS
Vol. 19, No. 3A, July-August 2023, pp. 3-10

Plasma Evolution within Streamer Discharge Channels at Transition between 2nd and 3rd Mode of Discharge

Sami A. Khalaf
Thamir H. Khalaf

Department of Physics, College of Science, University of Baghdad, Baghdad, IRAQ

The objective of this research is to investigate the evolution of the streamer discharge in transformer oil during the discharge and electrical breakdown stages. Observing the plasma's growth inside streamer discharge channels as the second Mode changes to the third Mode is the main goal of this investigation. This study provides details on the plasma channels, including the initiation time at which the streamer initially discharged, the velocity at which it expanded out, the streamer's radius, how it increased in size, and how it altered before it reached the cathode (plane electrode). The finite element method was used throughout this experiment using the Comsol Multiphysics program. The needle plate we used for the simulation has a fixed needle tip radius of 40 µm, with a gap of 1 mm, and the process's applied voltages are 300 kV.

Keywords: Numerical simulation; Plasma channels; Streamer discharge; Breakdown
Received: 18 February 2023; **Revised:** 07 March 2023; **Accepted:** 14 March 2023

1. Introduction

High-voltage electrical machinery and pulsed power systems typically employ transformer oil and other dielectric fluids. The electrical behaviors they exhibit in strong electric fields and potential breakdown processes give them significant practical value [1]. There have been theoretical and experimental research on the streamer shape, electric field, and velocity in liquid dielectrics for the past three decades [2-3]. Moreover, cutting-edge experimental methods have been used to study liquid breakdown and breakdown processes [4-7]. To comprehend the mechanics underlying electrical breakdown and lessen the possibility of it occurring, scientists and engineers have long examined the insulating characteristics of dielectric liquids, notably transformer oils [8]. This is due to the potential for extensive consequences of an insulation failure in an electric power apparatus. Its primary objective has been the creation of electrical streamers. When an extreme electric field stress of at least 1×10^8 V/m has been applied, these low-density conductive structures develop [9]. A streamer tends to become longer after it forms as it goes from the site of commencement to a grounding point. Persistent overexcitation may result in a streamer shorting the oil gap between the electrodes. As a result, an electrical breakdown will occur and an arc will form. The literature on streamers in dielectric liquids has grown significantly as a result of actual research that has been conducted extensively on the topic. The references [1] to [8] are indicative of this literature. Nevertheless, unlike the gaseous and solid phases, liquids have more complicated molecular structures and behaviors, and even the cleanest liquids include minute quantities of contaminants, which makes it challenging to identify the precise causes of electrical breakdown [7,8]. Researchers have experimentally discovered that the voltage input to the liquid (i.e., amplitude, polarity, waveform, duration, rising time, fall time, etc.) greatly affects the propagation properties of streamers [1-6]. According to experimental data, positive streamers from the positive electrode in transformer oil generally begin at lower applied voltages and spread farther and quicker than negative streamers [1,2]. The first, second, third, and fourth types of positive streamer propagation for lightning impulse voltage excitations in transformer oil have been identified.

The four modes all start at different amplitudes, with the first mode starting at the lowest and the fourth mode starting at the highest. As the streamer propagation velocity significantly rises, the third mode begins at the acceleration voltage V_a, whereas the second mode begins at the breakdown voltage Vb, which denotes a 50% chance of breakdown [6]. As a result, the streamer's form and velocity vary considerably with increased applied voltage, becoming more harmful and energetic.

As a result of its low propensity to result in a breakdown, the first mode is typically ignored in a pre-breakdown study [10]. The propagation velocity for second, third, and fourth mode streamers, on the other hand, are, respectively, in the range of 1 km/s, 10 km/s, and 100 km/s [2-6]. As the streamer transitions from the sluggish 2nd mode to the very energizing 4th mode, the applied voltage range for the 3rd mode region is lower than that of the 2nd mode. As a result, the 3rd mode streamer in transition presents a danger since it might quickly convert to the extraordinarily rapid 4th mode streamer with just a slight increase in applied voltage.

The first and second modes are the main topics of streamer data in the literature. With the development of measuring technology, experimental data for the quick-moving third mode and, to a lesser degree, the fourth mode, have recently expanded dramatically in quantity and quality. The researchers' ability to comprehend and formulate hypotheses about the underlying mechanisms that result in the creation of streamers and the various modes has improved as a consequence of the growth in empirical studies. For non-homogeneous dielectric liquids such as transformer oil, Biller hypothesized that ionization of the primary "ordinary" molecules produces faster modes than the equivalent of second mode streamers, which are associated with ionization of the "easily ionizable" molecules. While aromatic molecules are equally easily ionizable as naphthenic and paraffinic compounds, they have lower number densities [9,13] and ionization energies [11,12]. The bulk of transformer oil is made up of "ordinary" molecules, mostly naphthenic and paraffinic hydrocarbons.

2. Creating the Model

2.1 The Main Equations of the Model

Our study depends on four main equations that represent the continuity equations for positive ions as in equation (1), negative ions, in equation (2), and electrons represented by equation (3) in addition to Poisson's equation as in (4), where these four equations represent the governing equations for our work, by the hydrodynamic drift-diffusion model [14].

$$\frac{\partial \rho_p}{\partial t} + \nabla \cdot (\rho_p \mu_p \vec{E}) = G_F(|\vec{E}|) + \frac{\rho_p \rho_e R_{pe}}{q} + \frac{\rho_p \rho_n R_{pn}}{q} \quad (1)$$

$$\frac{\partial \rho_n}{\partial t} - \nabla \cdot (\rho_n \mu_n \vec{E}) = \frac{\rho_e}{\tau_a} - \frac{\rho_p \rho_n R_{pn}}{q} \quad (2)$$

$$\frac{\partial \rho_e}{\partial t} - \nabla \cdot (\rho_e \mu_e \vec{E}) = -G_F(|\vec{E}|) - \frac{\rho_p \rho_e R_{pe}}{q} - \frac{\rho_e}{\tau_a} \quad (3)$$

$$\nabla \cdot (\varepsilon \vec{E}) = \rho_e + \rho_p + \rho_n \quad (4)$$

In the previously stated equations, q is the electron charge; Ɛ is the relative permittivity of the dielectrics (the relative permittivity of the transformer oil is set to 2.2); E is the local electric field; and G (|E|) is the term describing the source of the insulating fluid's ionization in response to the electric field. R_{pe} and R_{pn} stand for the recombination rates of ions-ions, ions-electrons, and ions-ions in the insulating fluid, respectively, whereas μ_p, μ_e, and μ_n stand for the mobility of positive ions, electrons, and negative ions. The molecular ionization caused by the electric field in the transformer oil is difficult to describe with words. This ionization is what caused this charge source. The chemical complexity of the oil and the lack of a unified theory of liquid dielectrics make the issue more challenging [14]. Transformer oil produces positive and negative ions as well as free electrons as a result of field ionization that takes place during discharge. A free electron as well as positive and negative ions can be produced when an electron is raised into the conduction band of a neutral molecule by strong electric fields. Field ionization is the name given to this phenomenon. The Zener model was used by J. C. Devins et al. [15] to explain how streamer discharges spread in dielectric liquids. They found via their qualitative investigation that field ionization in liquids is inversely connected to the liquid molecules' ionization potentials and proportionate to the liquid's density [14, 15, 16].

$$G_F(|\vec{E}|) = \frac{q^2 n_0 a |\vec{E}|}{h} \exp\left(-\frac{\pi^2 m^* a \Delta^2}{q h^2 |\vec{E}|}\right) \quad (5)$$

The following terms are included in the equation: n_0, the number of density in ionizable transformer oil; Δ the electric energy needed to emit the molecules; h, the Planck constant; and m^*, the effective electron mass; a is the separation of molecules; q is the amount of electron's charge. The primary physical parameters required for the simulation model used in this investigation were found in the literature [17-20], as shown in Table (1).

Table (1) The most important parameters used in the model

Parameter	Symbol	Value
The number of density in ionizable transformer oil	n_0	1×10^{23} m^{-3}
The electric energy needed to emit the molecules	Δ	$8.5-50\sqrt{1.9528\times10^{-12}\,\lvert\vec{E}\rvert}$ eV
Separation of Molecules	a	3.0×10^{-10} m
Rate of ion-ion recombination	R_{pn}	1.64×10^{-17} m^{3}s^{-1}
Rate of ion-electron recombination	R_{pe}	1.64×10^{-17} m^{3}s^{-1}
Positive ion mobility	μ_p	1×10^{-9} m^{2}V^{-1}s^{-1}
Negative ion mobility	μ_n	1×10^{-9} m^{2}V^{-1}s^{-1}
Electron mobility	μ_e	1×10^{-4} m^{2}V^{-1}s^{-1}
Effective electron mass	m^*	$0.1\times m_e = 9.11\times10^{-32}$ kg

2.2 Simulation Domain

The discharge in transformer oil, the needle-plate electrode is designed based on IEC 60897 Standard [21]. The oil gap in the simulation is spaced 1 mm apart, and the spherical electrode has a radius of curvature of 6.35 mm while the needle electrode at the tip has a radius of curvature of 40 µm. The total domain dimensions are about r × z = 22 mm × 12.5 mm. It is possible to take advantage of the AutoCAD program to import the design that has been chosen and drawn into the Comsol Multiphysics program, where this is permitted. The domain has been designed, which consists of a needle, which represents the anode electrode, and a plate electrode (ground electrode), which represents the cathode electrode. Figure 1 (a), shows the used domain and (b), represents the distribution of the mesh on all the domains used. Noting that the dark black color represents a larger number of triangles along the

 ISSN (print) 1813-2065, (online) 2309-1673

electrodes and the axis of symmetry, which represents the activity area of the streamer discharge.

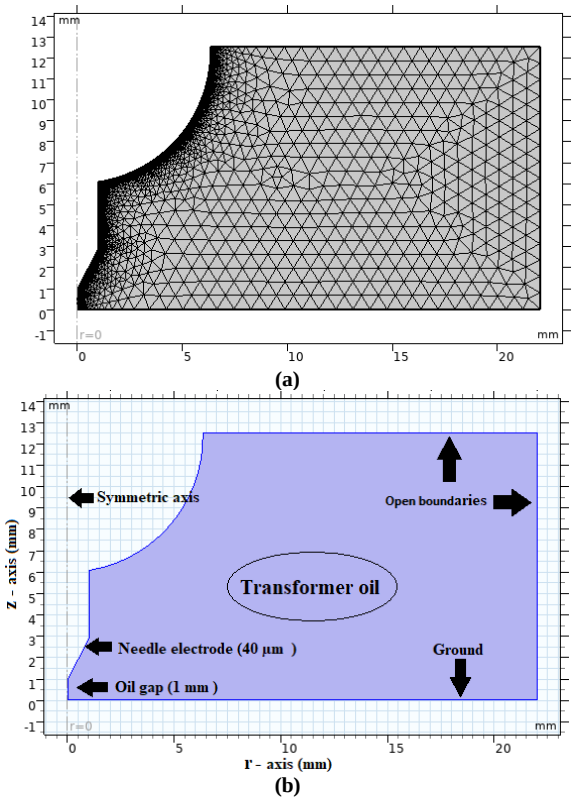

Fig. (1) (a) The model simulation computation region, and (b) Distributing of the mesh to the entire domain

2.3 Numerical Procedure and Boundary Condition

The boundary and spatial constraints for the equations must be established once the model's design has been added to the Comsol multiphysics program. The insulated walls are subject to the zero charge boundary condition, applied to ground V=0 is the plate-type electrode potential, whereas applied to $V=V_i$ is the needle-type electrode potential, and the Poisson equation characterizes an electrostatic process (4). The insulating walls have no impact on the electric field's lines. The standard lightning strike voltage described in IEC 600060-1 [22] can be subtracted from two exponential functions to get the voltage provided to the needle-type electrode.

$$V_i = KV_0\left(e^{-\frac{t}{\tau_1}} - e^{-\frac{t}{\tau_2}}\right) \qquad (6)$$

In this case, K serves as a nondimensional correction factor to keep K's maximum value at roughly the same level as V_0 [23]. Generally, subtracting two exponential functions τ_1 for the rising time and τ_2 for the falling time leads to a maximum value that isn't always equal to 1. Both the plate-type electrode potential and the needle-type electrode potential are set to the outflow boundary conditions for the three-carrier continuity equations, where the outer boundary does not have any flux boundary requirements (1-3). COMSOL Multiphysics version 6. 0 was used to solve the hydrodynamic model of the streamer discharge. To calculate Poisson's equation (4) and the carrier continuity equations (1-3), the modules "Electrostatic" and "Transport of Diluted Species" are used, respectively. Figure (2) represents the flowchart of the simulation process from start to end and obtaining the results.

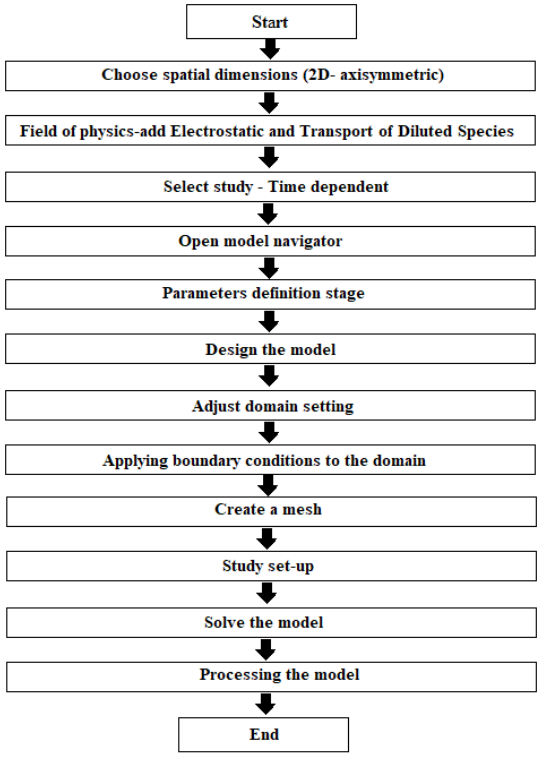

Fig. (2) Schematic of the simulation process

3. Results and Discussion

This simulation was designed to track and determine the evolution of the plasma inside its channels, where the needle-plate system was used during the simulation, the radius of curvature of the tip of the needle was 40 µm, and the curvature of the sphere was 6.35 mm, according to IEC 60897 Standard [21]. The gap between the two electrodes was filled with transformer oil and specified at 1 mm. When the electric field is larger than a threshold value (7.4 kV/mm), it has been shown that the streamer begins to form and propagate over the solution domain between the two electrodes. The second condition is that at the streamer's top edge, the electric field must be larger than the required level (200 kV/mm). [24,25]. The liquid's density reduces with heat, according to the electronic theory, providing electrons more energy before they hit a molecule. Following the impact that ionizes the molecule, two slowly moving electrons go across the field. A concentration of low-energy electrons begins to spread spherically toward the front of the streamer under the effect of the ensuing cloud of negative charge. [3,26,27]. Once a streamer has passed through a gap, it seems thicker and expands. As the area's density lowers, the rate of electron implication will

rise [28-30]. Electrons may be transported into the electrode bulk and released from the lattice if the electrical field is high enough. The required field strength may be between 10^7 and 10^8 V/m [31], depending on the electrode material.

According to the outcomes of the numerical analysis, field ionization is the fundamental reason for the commencement and spread of second and third-mode positive streamers. The simulation process's results demonstrated that the streamer discharge's propagation velocity increases gradually via the electric field starting at the time of streamer production, which occurs at a time of 32.4 ns and a voltage of 28.6 kV. Additionally, we found that the streamer's propagation velocity is 6.24 km/h during the first 50 ns at 300 kV and grows until the third mode change happens at 95 ns when it grows to 10.5 km/h as in table (2) below.

Table (2) Track the evolution of plasma channels through an electric field at 300 kV

Time (ns)	Streamer Length (mm)	Rate of Propagation Velocity (km/s)	Radius of Streamer (mm)	Modes	status
90	0.85	9.5	0.2	2nd	Stable
95	1	10.5	0.25	2rd	Unstable
100	1	10	0.29	2rd	Unstable
105	1	9.5	0.33	2nd	Stable
110	1	9.09	0.36	2nd	Stable
115	1	8.6	0.41	2nd	Stable
120	1	8.3	0.62	2nd	Stable
125	1	8	0.8	2nd	Stable

When the plasma channels reach the ground electrode, an electrical breakdown occurs, and a significant portion of the applied voltage is lost, leading to a significant decrease in the electric field. Subsequently, the propagation velocity starts to decrease again. Figure (3) shows the moment of transition between the second and third modes (3a) the streamer discharge at 90 ns for 300 kV and (3b) the streamer discharge at 90 ns for 300 kV. According to the results obtained, the streamer velocity increases to reach the highest value after it transits from the 2nd to the 3rd mode, and then it returns to 6.6 km/s, after that becomes 5 km/s, and starts to diminish due to electrical breakdown and loss of electrical potential. The electric field can also be represented for several periods by a one-dimensional diagram, as illustrated in Fig. (4).

Figure (5) represents the evolution of the streamer discharge, starting from its formation at the tip of the needle, passing through its transition from the 2nd to the 3rd mode, all the way to the ground electrode, and the occurrence of an electrical breakdown.

As for the results that we found, the drift velocity of the space charge density appears to be slower than it is in the rate of the velocity of the streamer due to the electric field, as the drift velocity of the streamer remains in a stable state within the second mode and there is no transition to the third mode, as in table 3.

Figure (6) represents the space charge density for two periods, 50 and 100 ns at 300 kV, while figure (7) represents the periodic time, one-dimensional development of space charge density.

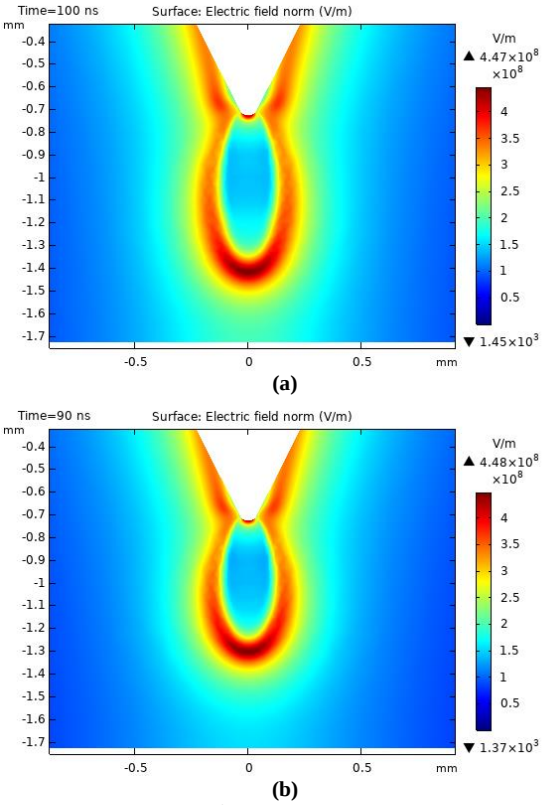

Fig. (3) The moment of transition to the third mode (a) the streamer discharge at 90 ns for 300 kV and (b) the streamer discharge at 100 ns for 300 kV

Table (3) Tracking the evolution of the space charge density at 300 kV

Time (ns)	Streamer Length (mm)	Drift Velocity (km/s)	Radius of Streamer (mm)	Modes	status
90	0.58	6.5	0.17	2nd	Stable
95	0.64	6.7	0.17	2nd	Stable
100	0.7	7.03	0.176	2nd	Stable
105	0.76	7.29	0.18	2nd	Stable
110	0.84	7.6	0.19	2nd	Stable
115	0.93	8.1	0.193	2nd	Stable
120	1	8.3	0.19	2nd	Stable
125	1	8	0.2	2nd	Stable

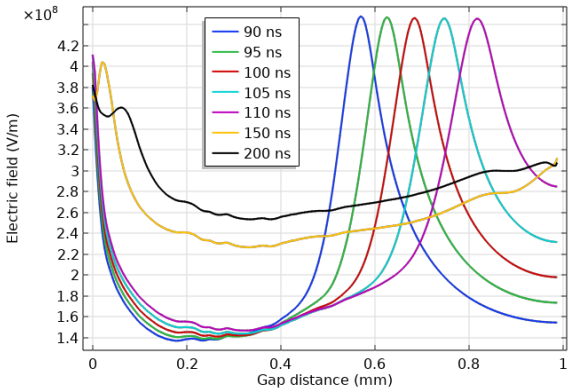

Fig. (4) The electric field represented for several periods by a 1D diagram

 ISSN (print) 1813-2065, (online) 2309-1673

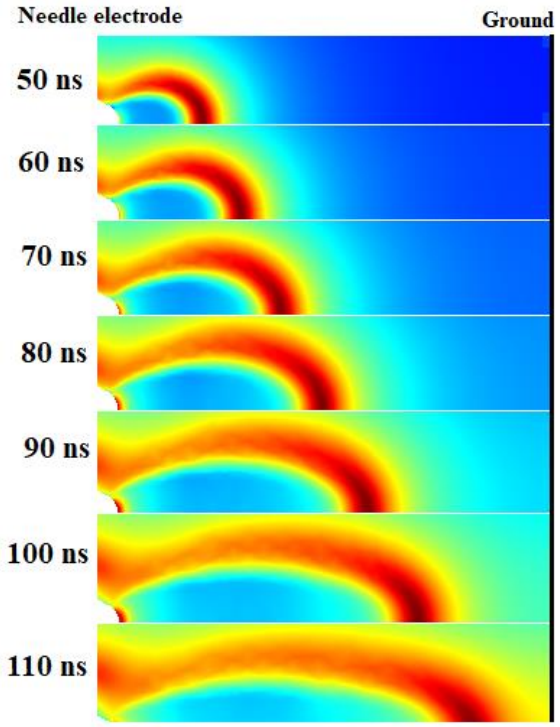

Fig. (5) The evolution of the streamer discharge at 300 kV for several periods

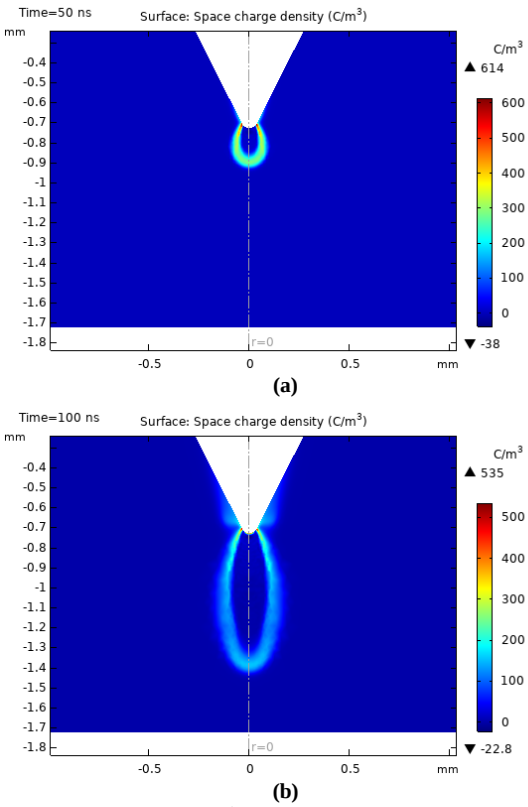

Fig. (6) The elongation of the space charge density (a) at 50 ns for 300 kV and (b) at 100 ns for 300 kV

Since the plasma channels only maintain their speed within the confines of the second mode and no transmission to the third mode occurs, the streamer formed by the positive ions is thinner than when it is formed under the influence of the electric field, and the rate of velocity is much slower than it is in the streamer formed through the electric field, as shown in table (4) below. The time chronology of the streamer's progression through the positive ions is depicted in Fig. (8).

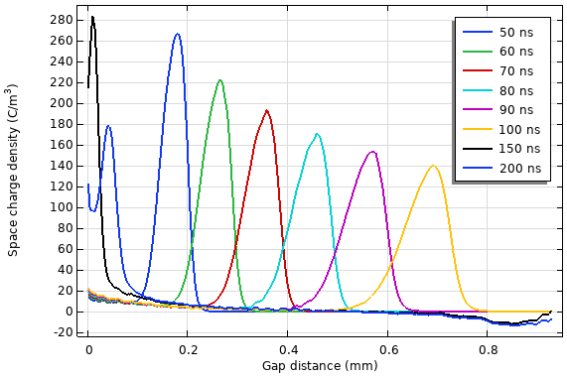

Fig. (7) Space charge density values changing according to changing periods in one dimension

Table (4) Tracking the evolution of the positive ions at 300 kV for several periods

Time (ns)	Streamer Length (mm)	Drift velocity (km/s)	The radius of the streamer (mm)	Modes	Status
90	0.57	6.3	0.13	2nd	Stable
95	0.63	6.6	0.14	2nd	Stable
100	0.69	6.9	0.15	2nd	Stable
105	0.74	7.1	0.156	2nd	Stable
110	0.81	7.4	0.16	2nd	Stable
115	0.9	7.8	0.163	2nd	Stable
120	1	8.3	0.167	2nd	Stable
125	1	8	0.16	2nd	Stable

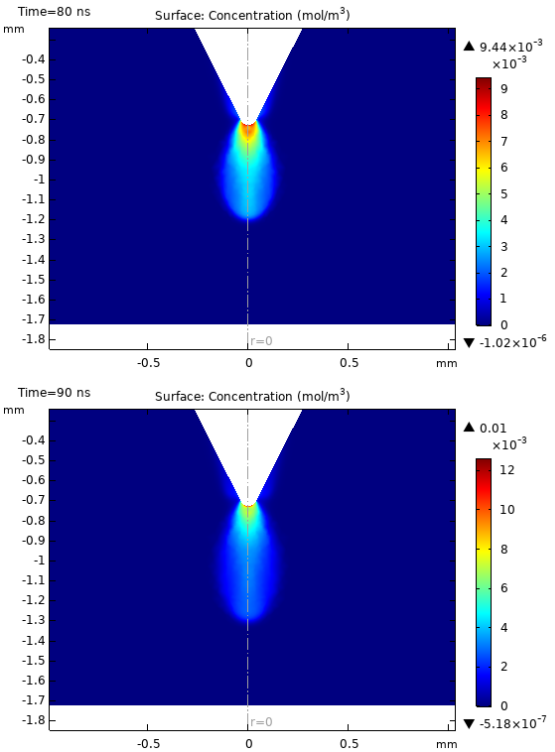

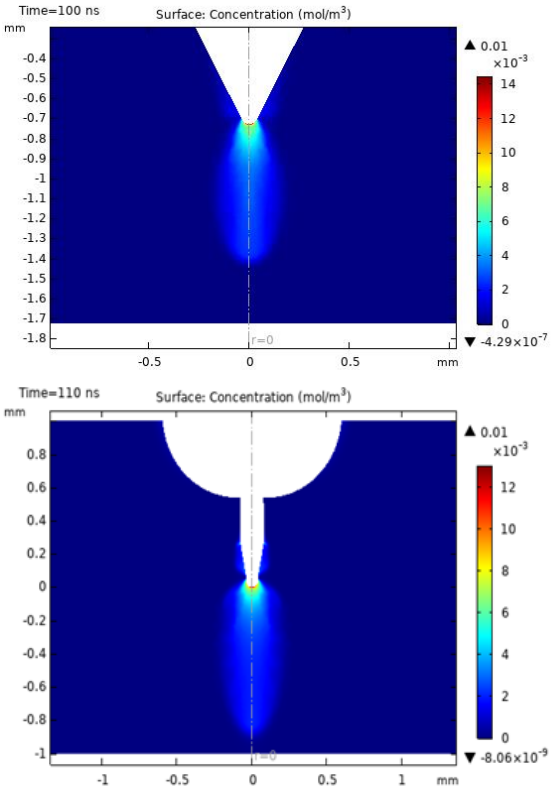

Fig. (8) Changes in positive ions during specific time intervals

Through the results obtained, we found that the propagation velocity, the length, and the radius of the streamer discharge during its formation under the influence of the concentration of negative ions, were close to the electron concentrations, as in table (5) below. Figure (9) represents some stages of the chronological sequence of the formation of the streamer under the influence of the concentration of negative ions, and figure (10) represents some of the stages of the evolution of the electrons.

Table (5) Tracking the evolution of the negative ions at 300 kV

Time (ns)	Streamer Length (mm)	Drift Velocity (km/s)	The radius of the streamer (mm)	Modes	Status
90	0.36	8	0.04	2nd	Stable
95	0.38	4.08	0.05	2nd	Stable
100	0.41	4.15	0. 06	2nd	Stable
105	0.44	4.24	0. 07	2nd	Stable
110	0.46	4.26	0. 076	2nd	Stable
115	0.49	4.31	0. 08	2nd	Stable
120	0.5	4.39	0. 08	2nd	Stable
125	0.54	4.34	0. 09	2nd	Stable

Table (6) Tracking the evolution of the electron concentrations at 300 kV

Time (ns)	Streamer Length (mm)	Drift Velocity (km/s)	The radius of the streamer (mm)	Modes	Status
90	0.54	6	0.09	2nd	Stable
95	0.59	6.2	0. 095	2nd	Stable
100	0.65	6.5	0. 095	2nd	Stable
105	0.71	6.7	0. 099	2nd	Stable
110	0.77	7.04	0. 099	2nd	Stable
115	0.88	7.6	0. 099	2nd	Stable
120	1	8.3	0. 099	2nd	Stable
125	1	8	0. 099	2nd	Stable

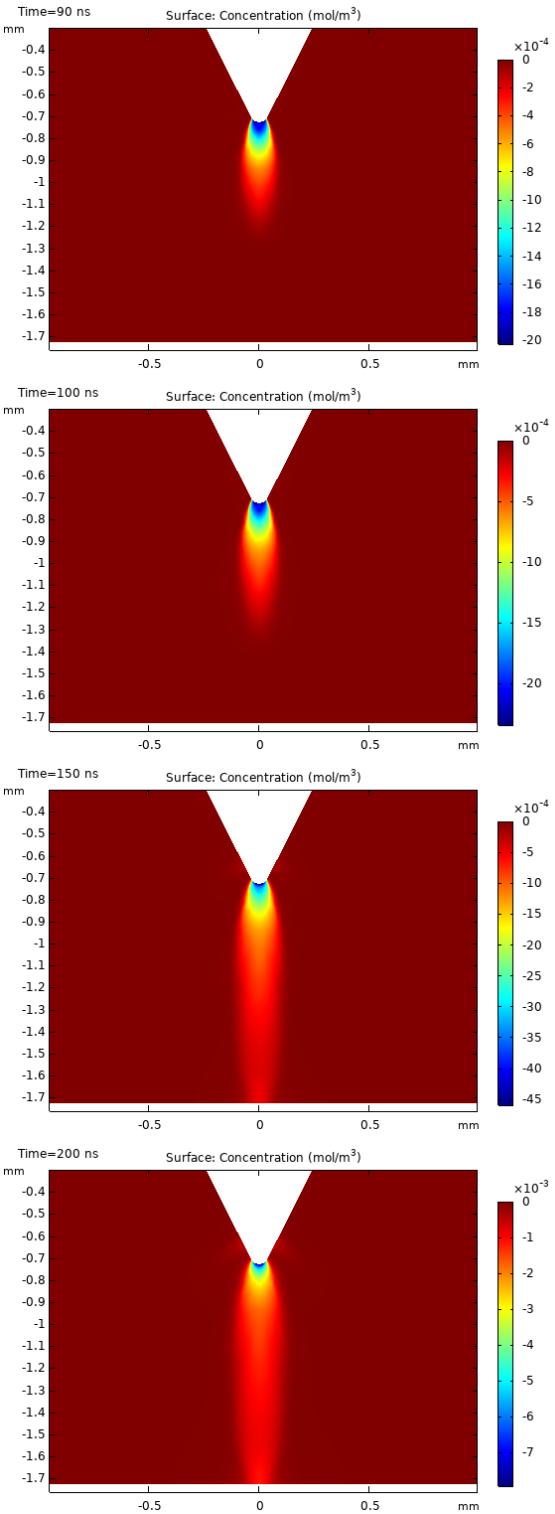

Fig. (9) Evolution of negative ions at specific periods

 ISSN (print) 1813-2065, (online) 2309-1673

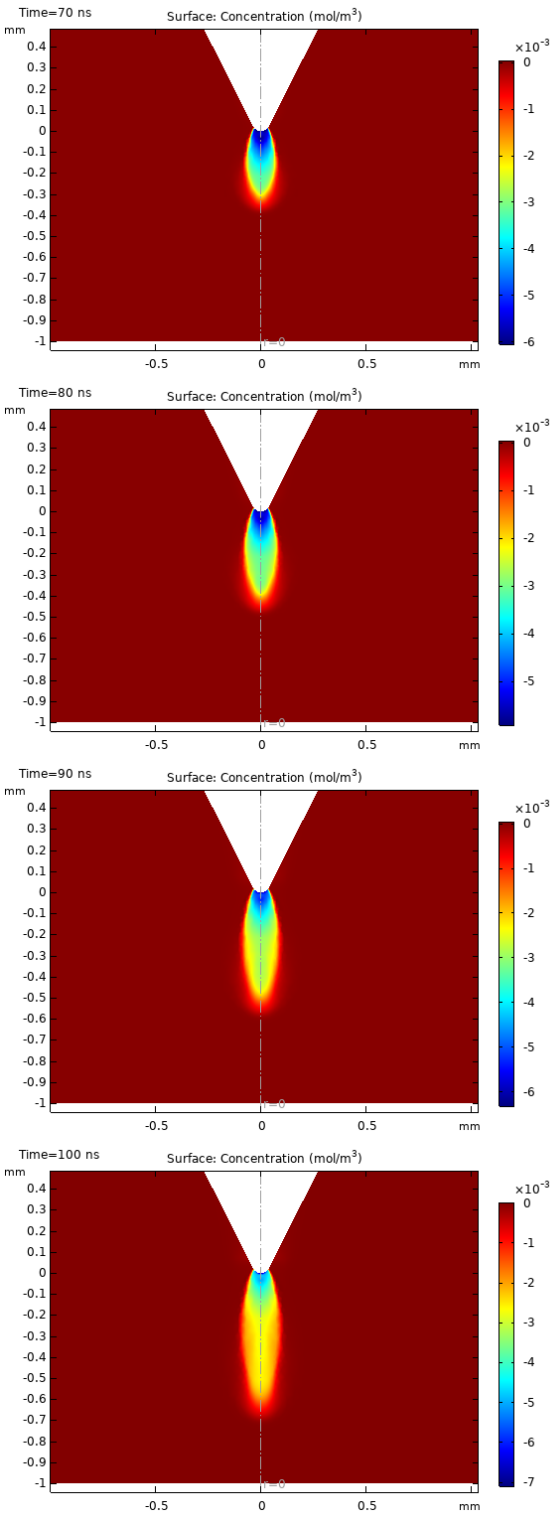

Fig. (10) Evolution of electron concentrations at specific periods

The rates of the velocity of the streamer discharge created by the electric field's influence, the velocity of the space charge density, the velocity of the positive ions, and the velocity of the negative ions and electrons are all compared in Fig. (11).

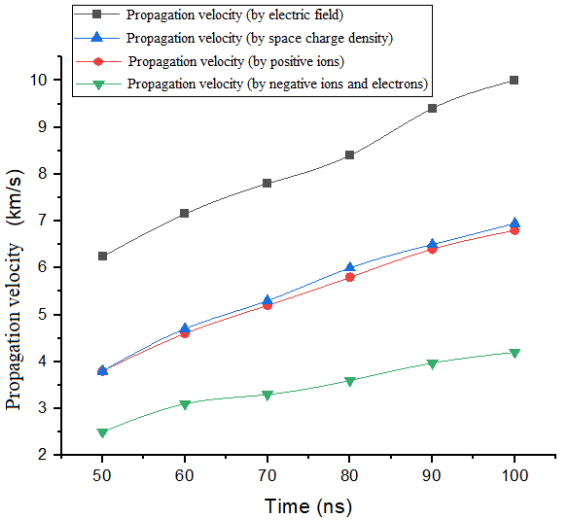

Fig. (11) Propagation velocity of the streamers' discharge at specific periods

4. Conclusion

The simulation's domain, which was created based on the IEC 60897 Standard [21], specifies how the needle-plate electrode arrangement should be set up. The radius of curvature of the spherical electrode is 6.35 mm, that of the needle electrode at the tip is 40 m, and the oil gap in the simulation is specified at 1 mm. The total domain boundaries are about r×z= 22mm×12.5mm. Our results showed that the lowest voltage needed to produce a streamer discharge occurred at 32.4 ns with a voltage of 28.6 kV. We observed from the data that there is an elongation, a change in velocity, and a change from the 2nd to the 3rd mode. The space charge density and the concentrations of positive ions, negative ions, and electrons all increase when a 300 kV voltage is applied.

References

[1] R.P. Joshi et al., "Aspects of plasma in water: streamer physics and applications", *Plasma Process. Polym.*, 6(11) (2009) 763-777.

[2] J.C. Devins, J.R. Stefan and R.J. Schwabe, "Breakdown and prebreakdown phenomena in liquids", *J. Appl. Phys.*, 52(7) (1981) 4531-4545.

[3] Y. Li et al., "Sub-microsecond streamer breakdown in transformer oil-filled short gaps", *IEEE Trans. on Dielect. Electric. Insul.*, 21(4) (2014) 1616-1626.

[4] R.E. Hebner, "Measurement of electrical breakdown in liquids", The liquid state and its electrical properties, (1988) 519-537.

[5] D.L. Linhjell, L. Lundgaard and G. Berg, "Streamer propagation under impulse voltage in long point-plane oil gaps", *IEEE Trans. on Dielect. Electric. Insul.*, 1(3) (1994) 447-458.

[6] Y.V. Torshin, "On the existence of leader discharges in mineral oil", *IEEE Trans. on Dielect. Electric. Insul.*, 2(1) (1995) 167-179.

[7] L. Lundgaard et al., "Propagation of positive and negative streamers in oil with and without pressboard

interfaces", *IEEE Trans. on Dielect. Electric. Insul.*, 5(3) (1998) 388-395.
[8] A. Beroual et al., "Propagation and structure of streamers in liquid dielectrics", *IEEE Electric. Insul. Mag.*, 14(2) (1998) 6-17.
[9] J.G. Hwang et al., "Modeling streamers in transformer oil: The transitional fast 3rd mode streamer", in *2009 IEEE 9th Int. Conf. on Properties and Applications of Dielectric Materials (July, 2009)*, 573-578.
[10] L. Costeanu and O. Lesaint, "On mechanisms involved in the propagation of subsonic positive streamers in cyclohexane", in *Proc. 2002 IEEE 14th Int. Conf. on Dielectric Liquids (ICDL 2002) (July, 2002)*, 143-146.
[11] M. Harada et al., "Ionization energies for solvated polycyclic aromatic hydrocarbons", *Chem. Phys. Lett.*, 303(5-6) (1999) 489-492.
[12] H.S. Smalø, P.O. Astrand and S. Ingebrigtsen, "Calculation of ionization potentials and electron affinities for molecules relevant for streamer initiation and propagation", *IEEE Trans. on Dielect. Electric. Insul.*, *17*(3) (2010) 733-741.
[13] D.R. Lide (ed.), **"CRC Handbook of Chemistry and Physics",** CRC Press (2004) 85.
[14] R. Morrow and N. Sato, "The discharge current induced by the motion of charged particles in time-dependent electric fields; Sato's equation extended", *J. Phys. D: Appl. Phys.*, 32(5) (1999) L20.
[15] J. Jadidian and M. Zahn, "Charge transport analysis in two-phase composite dielectric systems", *IEEE Trans. on Plasma Sci.*, 41(9) (2013) 2464-2474.
[16] A.F. Al-rawaf and T.H. Khalaf, "Simulation of positive streamer discharges in transformer oil", *IOP J. Phys.: Conf. Ser.*, 2322(1) (2022).
[17] F.M. O'Sullivan, "A model for the initiation and propagation of electrical streamers in transformer oil and transformer oil-based nanofluids", Diss., Massachusetts Institute of Technology (2007).
[18] J. Jadidian et al., "Effects of impulse voltage polarity, peak amplitude, and rise time on streamers initiated from a needle electrode in transformer oil", *IEEE Trans. on Plasma Sci.*, 40(3) (2012) 909-918.
[19] A.K. Bard and Q.A. Abbas, "Influence of Cylindrical Electrode Configuration on Plasma Parameters in a Sputtering System", *Iraqi J. Sci.*, (2022) 3412-3423.
[20] R.S. Mohammed, K.A. Aadim and K.A. Ahmed, "Spectroscopy Diagnostic of Laser Intensity Effect on Zn Plasma Parameters Generated by Nd:YAG Laser", *Iraqi J. Sci.*, (2022) 3711-3718.
[21] Methods for the Determination of the Lightning Impulse Breakdown Voltage of Insulating Liquids, IEC Std. 60897 (1987).
[22] High-Voltage Test Techniques - Part 1: General Definitions and Test Requirements, IEC Std. 60060-1 (2010).
[23] O. Schenk and K. Gärtner, "Solving unsymmetric sparse systems of linear equations with PARDISO", *Future Gen. Computer Syst.*, 20(3) (2004) 475-487.
[24] T. Aka-Ngnui and A. Beroual, "Modelling of multi-channel streamers propagation in liquid dielectrics using the computation electrical network", *J. Phys. D: Appl. Phys.*, 34(5) (2001) 794.
[25] B.M. Cox and W.T. Williams, "Field-emission sites on unpolished stainless steel", *J. Phys. D: Appl. Phys.*, 10(3) (1977) L5.
[26] T.H. Khalaf and D.A. Uamran, "Simulation Following for Initiation, Growth, and Branching of Streamer Discharge in a 3mm Transformer Oil Filled Gap", *Int. J. Appl. Eng. Res.*, 12(24) (2017) 14842-14848.
[27] T.N. Tran et al., "Numerical modeling of negative discharges in the air with experimental validation", *J. Phys. D: Appl. Phys.*, 44(1) (2010) 015203.
[28] P. Biller, "A simple qualitative model for the different types of streamers in dielectric liquids", *ICDL'96, 12th IEEE Int. Conf. on Conduc. Breakdown in Dielectric Liquids* (1996).
[29] J. Jadidian and M. Zahn, "Unipolar charge transport in oil-pressboard systems with planar, coaxial cylindrical and concentric spherical electrode geometries", *Proc. 2011 Int. Symp. on Electric. Insul. Mater*. (IEEE, 2011).
[30] I. Madshaven et al., "Modeling the transition to fast mode streamers in dielectric liquids", *2017 IEEE 19th Int. Conf. on Dielect. Liquids (ICDL,* 2017).
[31] D. Liu, Q. Liu and Z. Wang, "Modelling of second mode positive streamer in cyclohexane by considering optimized electron saturation velocity", *J. Phys. D: Appl. Phys.*, 54(11) (2021) 115502.

 ISSN (print) 1813-2065, (online) 2309-1673

IRAQI JOURNAL OF APPLIED PHYSICS
Vol. 19, No. 3A, July-August 2023, pp. 11-18

Effect of In_2O_3 and Eu_2O_3 Dopants on Morphology and Gas Sensing Properties of CeO_2 Thin Films

Mustafa M. Rasheed
Bushra A. Hasan

Department of Physics, College of Science, University of Baghdad, Baghdad, IRAQ

Pulsed-laser deposition (PLD) technique was used to prepare thin films from cerium oxide (CeO_2) doped with erbium and indium oxides. In order to characterize the morphology and sensing features, these films were deposited on glass and/or single silicon substrates, respectively, with erbium and indium oxides. The morphological investigation conducted using atomic force microscope has shown an increase in the non-regularity of particle diameter with increasing doping ratios of both oxides. The maximum particle diameter of 61.45nm was obtained for 9% Eu_2O_3-doped CeO_2. The surface roughness value of Eu_2O_3-doped ceria was higher than those of In_2O_3-doped ceria. The gas sensing measurements were done at various working temperatures (303, 373, 423 and 473K). These measurements in ambient of ammonia (NH_3) gas for undoped ceria/Pc-Si showed the highest sensitivity of 54 % at temperature 473K.

Keywords: CeO_2; Eu_2O_3 dopant; In_2O_3 dopant; Gas sensing; PLD
Received: 15 February 2023; **Revised:** 07 April 2023; **Accepted:** 14 April 2023

1. Introduction

Semiconductors were made to satisfy the latest requirements for gas sensors [1]. In terms of stability, sensitivity and selectivity for gas detection, semiconductor gas sensor performs well [2]. The sensing materials include semiconductor-metal-oxides such as titanium oxide, tin oxide, zinc oxide, cerium oxide (CeO_2), tungsten oxide and zirconium oxide [3]. Due to its unique features, which notably result from its 4f shells, CeO_2 can be specified as one of the rare-earth oxide materials that is used in numerous industries, such as optical material, catalysts and gas sensors [4]. Due to CeO_2 is non-toxic element, so is a commonly utilized catalyst to reduce toxic gases, such as NO_x, CO, hydrocarbons and etc., that emit from the automobile exhausts. This oxide is one of the useful sensing materials for reducing gases due to its enormous oxygen vacancies, high oxygen storage capacity and low redox potential between Ce^{3+} and Ce^{4+} [5]. Thin film of europium oxide (Eu_2O_3) has prospective uses in a wide range of contemporary applications, including telecommunication, microelectronic, optical and optoelectronic devices [6-7]. Indium oxide nanocrystals have the potential to play a significant role in the development of microelectronic devices for solar cell, gas sensor, flat-panel display, transparent conductor [8], and architectural glass. Sputtering, vacuum evaporation, spray pyrolysis, sol-gel process [9], pulsed-laser deposition (PLD), and other techniques have all been used to prepare In_2O_3 film with a variety of morphologies and crystal structures. Literature review shows lack of researches related to eurbium and indium oxide in doping cerium oxide and to be used a gas sensor. Therefore, this is a novel study on gas sensing were made from CeO_2 doped with Eu_2O_3 and In_2O_3 oxides using PLD on n-type single-crystalline silicon wafer and investigate the influence of doping ratio and working temperature on the sensing properties, which include sensitivity, response and recovery time.

2. Experimental Part

In this work CeO_2 material, Eu_2O_3 and In_2O_3 oxides have been used with high purity (0.999). Different compounds with various doping ratios based on atomic weight were weighted with the use of electronic balance with three digits after the point. The demand amount of CeO_2 doped with Eu_2O_3 and In_2O_3 compounds were put in a quartz ampoule of a length of approximately 25cm and internal diameter of ~8mm, which was evacuated to about 10^{-3} torr and heated at 1273 K and for one hour and cooled to room temperature at 303K. Then, material has been grinded and pressed in pellet shape with 1 cm in diameter and 0.5 cm in thickness. Based on dopant material, two types of samples of (CeO_2:Eu_2O_3 and CeO_2:In_2O_3) with a variety of the doping ratios (0, 0.03, 0.05, 0.07 and 0.09) have been synthesized using PLD technique. These films have been deposited on glass and silicon wafers after cleaning to remove any grease, dust and other impurities. Deposition process was performed under vacuum of $2x10^{-2}$ torr by using Nd:YAG laser beam (with energy of 500 mJ, pulse of 300 shots and frequency of 6 Hz) which is focused on the target. Gas sensing measurements have been conducted in air and in ambient of NH_3 gas as different work temperatures (303, 373, 423 and 473K). The following equation for reducing gases

was used to calculate the sensitivity regarding the reducing gas sensors:

$S = \frac{Ra-Rg}{Rg}$ for n-type (1)

$S = \frac{Rg-Ra}{Ra}$ for p-type (2)

where R_a and R_g are the resistance in the presence of air and detected gas, respectively

3. Result and Discussion

The surface roughness of thin films of pristine CeO_2 and (CeO_2:Eu_2O_3) with varying doping ratios (0%, 3%, 5%, 7%, and 9%) that deposited on glass substrate are shown in Fig. (1). Average surface roughness and average diameter of grains values for these samples are included in AFM parameters (roughness and mean diameter) and are displayed in table (1). The table shows a decrease in average diameter of 36.88 nm up to 31.01 nm at 3% doping ratio, then an increase as the doping ratio increases. The results showed a well pronounced increment of diameter at 9% doping ratio. The roughness that considered as main factor of determine the adsorption take place on any surface showed non regular variation by increasing of doping ratio. It was noticed that introducing of europium oxide increased the surface roughness and support the appearance of more CeO_2 sites on the surface of the fabricated thin films, indicating that Eu_2O_3 ions support nucleation and grain growth. It is well-known that Eu_2O_3 ions are chemically active and easily adsorbed onto the substrate surface and consequently attracting the CeO_2 molecules by van der Waals forces for fast nucleation. It can be deduced that thin films with high Eu_2O_3 doping formed more bonds with CeO_2, producing smaller grains and hence greater roughness [11,12].

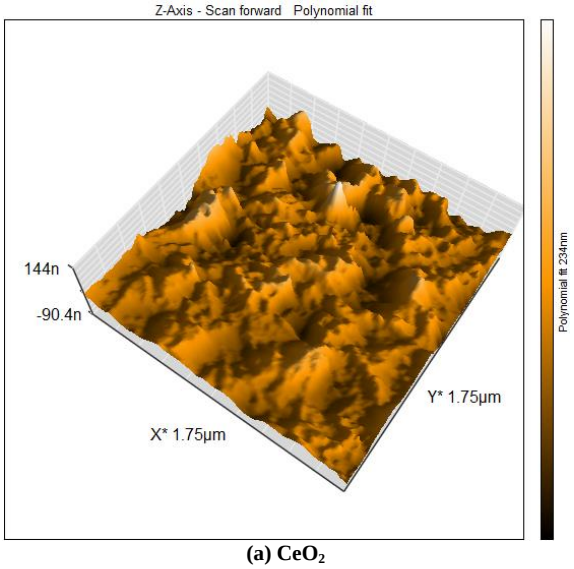

(a) CeO_2

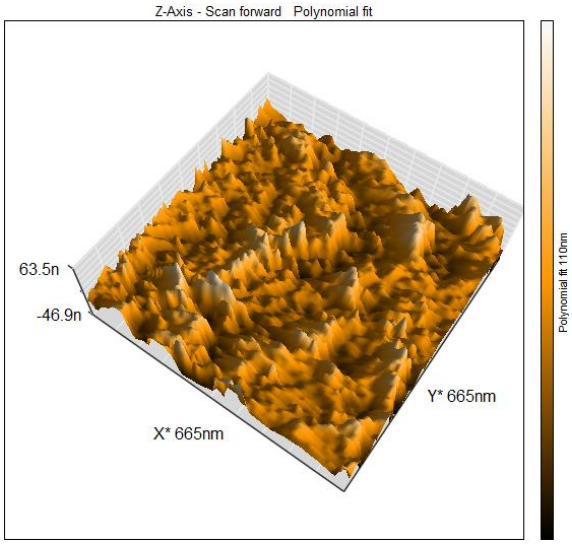

(b) CeO_2:3% Eu_2O_3

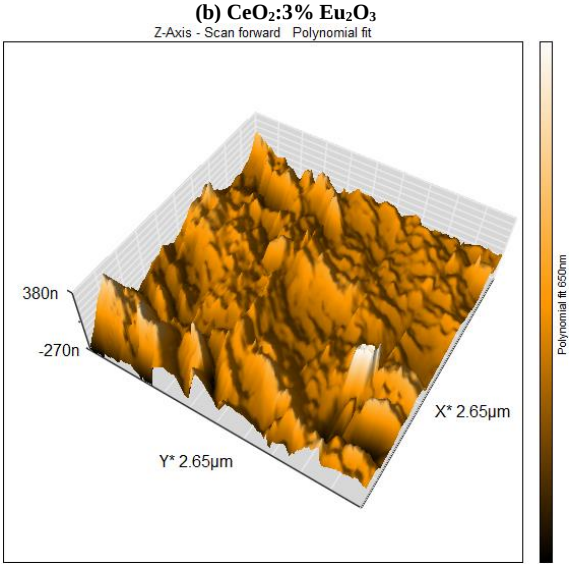

(c) CeO_2:5% Eu_2O_3

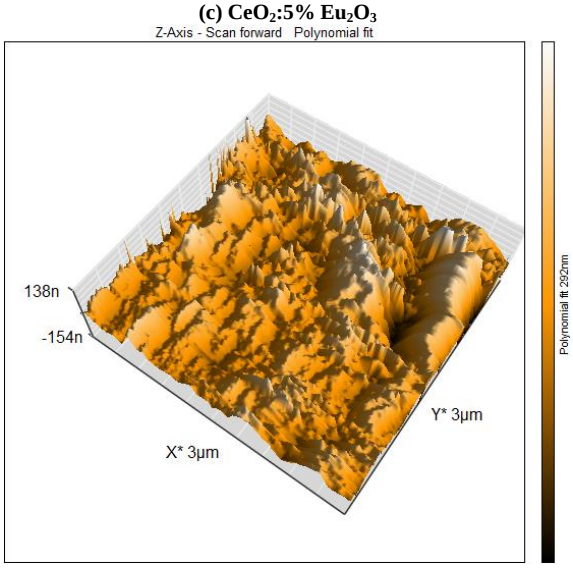

(d) CeO_2:7% Eu_2O_3

 ISSN (print) 1813-2065, (online) 2309-1673

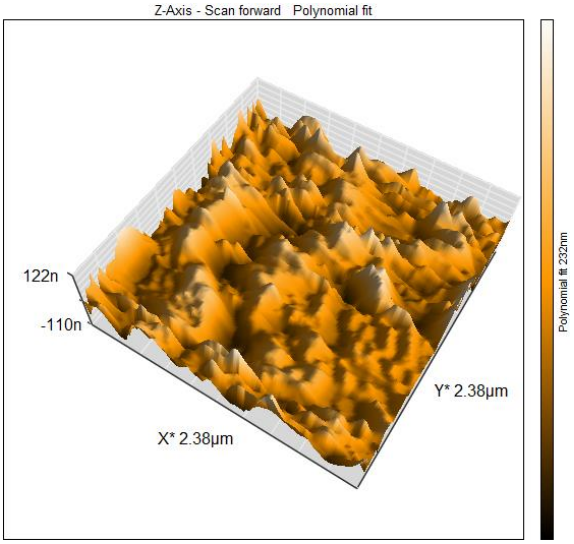

(e) CeO_2:9% Eu_2O_3

Fig. (1) AFM images of (a) pristine CeO_2 thin film, (b) CeO_2:3%Eu_2O_3, (c) CeO_2:5%Eu_2O_3, (d) CeO_2:7%Eu_2O_3, and (e) CeO_2:9%Eu_2O_3

Table (1) Roughness and mean diameter for pristine CeO_2 and (CeO_2:Eu_2O_3) thin films

Sample	Roughness (nm)	Mean diameter (nm)
CeO_2	17.35	36.88
CeO_2: 3% Eu_2O_3	36.99	31.01
CeO_2: 5% Eu_2O_3	28.17	37.46
CeO_2: 7% Eu_2O_3	15.59	36.20
CeO_2: 9% Eu_2O_3	6.970	61.45

AFM images for thin films of pristine CeO_2 and (CeO_2:In_2O_3) with varying doping ratios (0%, 3%, 5%, 7%, and 9%) deposited on glass substrate are shown in Fig. (2). Average roughness and average diameter values for such samples are included in AFM parameters and are displayed in table (2). It is noticed that the nanoparticles (NPs) developed in separated sharp peaks through smooth roughness that resembled saw teeth [13].

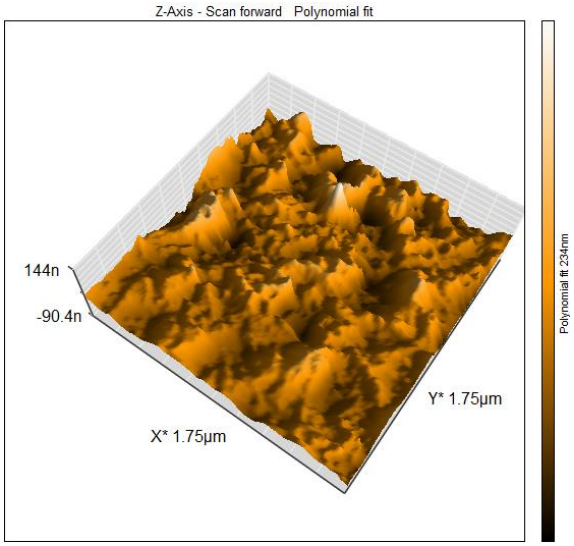

(a) CeO_2

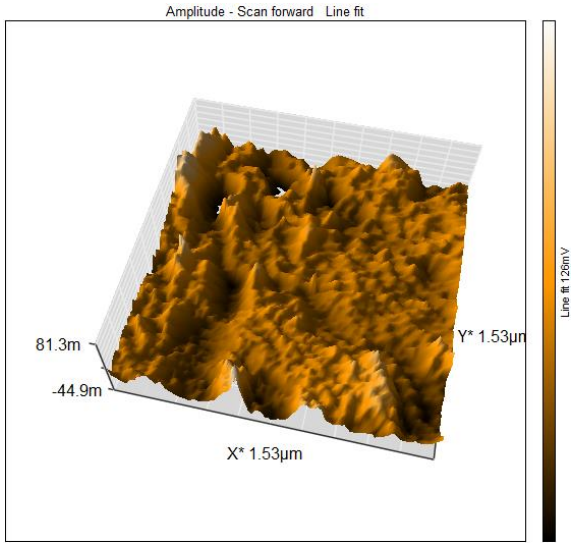

(b) CeO_2:3% In_2O_3

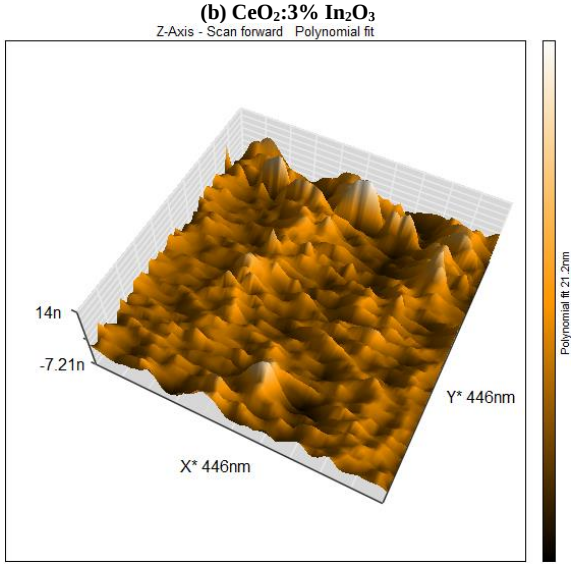

(c) CeO_2:5% In_2O_3

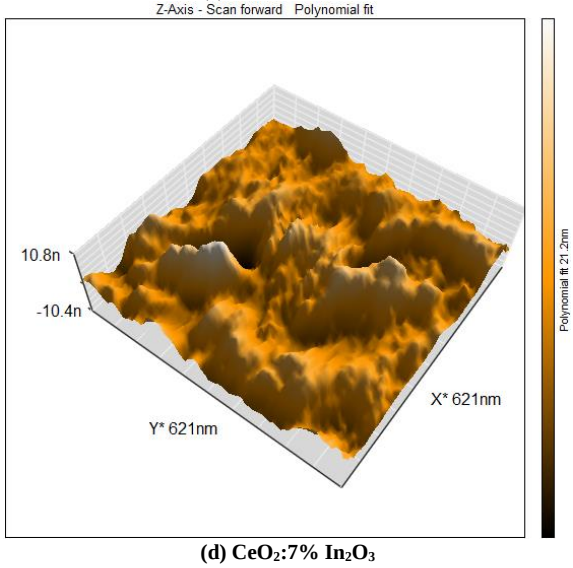

(d) CeO_2:7% In_2O_3

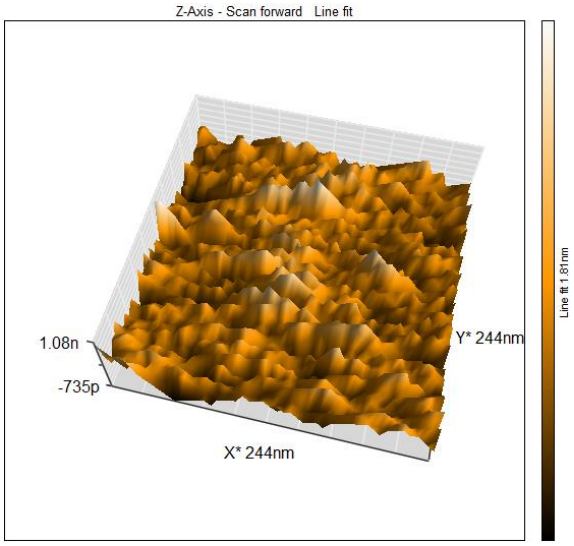

(e) CeO_2:9% In_2O_3

Fig. (2) AFM images of (a) pristine CeO_2 thin film, (b) CeO_2:3% In_2O_3, (c) CeO_2:5% In_2O_3, (d) CeO_2:7% In_2O_3, and (e) CeO_2:9% In_2O_3

Table (2) Roughness and mean diameter for pristine CeO_2 and (CeO_2:In_2O_3) thin films

Sample	Roughness (nm)	Mean diameter (nm)
CeO_2	17.35	36.88
CeO_2: 3% In_2O_3	17.94	50.62
CeO_2: 5% In_2O_3	31.26	42.38
CeO_2: 7% In_2O_3	14.84	43.77
CeO_2: 9% In_2O_3	0.2478	39.07

The resistance of (CeO_2:Eu_2O_3) to NH_3 gas at various temperatures (303, 373, 423, and 473K) was depicted in the figures (3-7) as a variation of electrical resistance with time. Except for the sensors with high operating temperatures and high doping ratios, all sensor cells demonstrated growing resistance as the sensors' exposure to detecting gas gave rise to the p-type semiconductors. When the detected gas interacts with the surface of the metal oxide film (essentially surface adsorbed oxygen ions), which results in a change the charge carrier concentration of the material. The change of carrier concentration serves to alter the conductivity (or resistivity) of the material. Mainly, electron is the majority of charge carrier for n-type semiconductor that interacts with a reducing gas an increase in conductivity occurs. Conversely, an oxidizing gas serves to deplete the sensing layer of charge carrying electrons, resulting in a decrease in conductivity. A p-type semiconductor is a material that conducts with positive holes being the majority charge carriers; hence, the opposite effects are observed with the material and showing an increase in conductivity in the presence of an oxidizing gas (where the gas has increased the number of positive holes). A resistance increase with a reducing gas is observed, where the negative charge introduced into the material reduces the positive (hole) charge carrier concentration [14-15]. Ceria at 423 and 473 K, respectively, doped with 7% and 9% Eu_2O_3, with existence of identified gas, have demonstrated a reduction in resistance, resulting in n-type semiconductors. The findings demonstrate that, particularly for high doping ratios, such as 0, 5, 7, and 9%, the sensitivity of gas sensing thin films rises with increasing operating temperature and the 5% doping ratio has shown the optimum sensitivity values. At 303K, which is referred to the ideal temperature, 5% Eu_2O_3-doped CeO_2 thin films have shown the highest sensitivity value (19.7%). The highest sensitivity was found for ceria material that traps free electrons at the surface and causes more extensive composite layer depletion as well as a larger reduction in conductance (increases in resistance) because of oxygen adsorption. As a result, the ceria material is superior to binary oxide sensors in terms of sensitivity [16]. Comparable to the findings of [17-19], agglomeration of particles into bigger grains causes a decrease in their catalytic activity, which is related to the severe reduction of sensitivity at high doping ratios (0.07, 0.09). Response and recovery times shown in table (1) decrease with increasing working temperature. The minimum value of response time was 11.7 s for 3% Eu_2O_3-doped ceria at 303 K. These results seem in contrast to the literature, such as Kai Sun et al. [20], who have synthesized chemi-resistive sensors based on CeO_2/ZnO heterojunction-nanorod-array using anodic electrode position coating and investigate gas-detecting characteristics. The fabricated sensor based on this CeO_2/ZnO heterojunction showed a much higher sensitivity to NO_2 at working temperature 393 K. They explained the enhancement in gas sensing characteristics due to the formation of built-in field due to heterojunction, which supplied more charge carriers and hence more target gases can be adsorbed. The obtained sensitivity was 49.3% at temperature of 393 K, which lower than our value (54.4%) at 473 K.

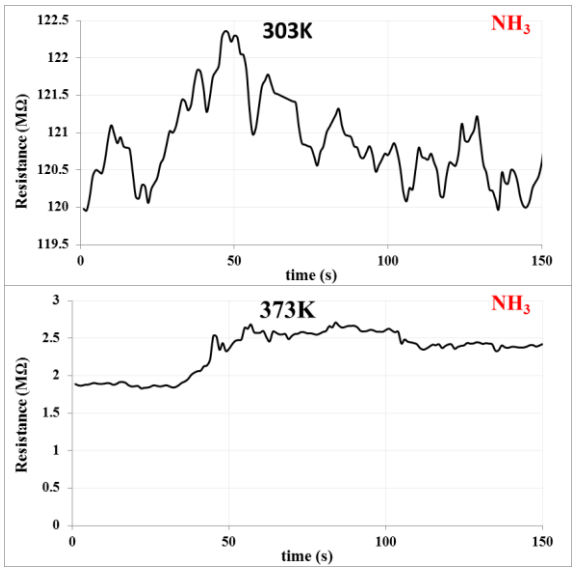

 ISSN (print) 1813-2065, (online) 2309-1673

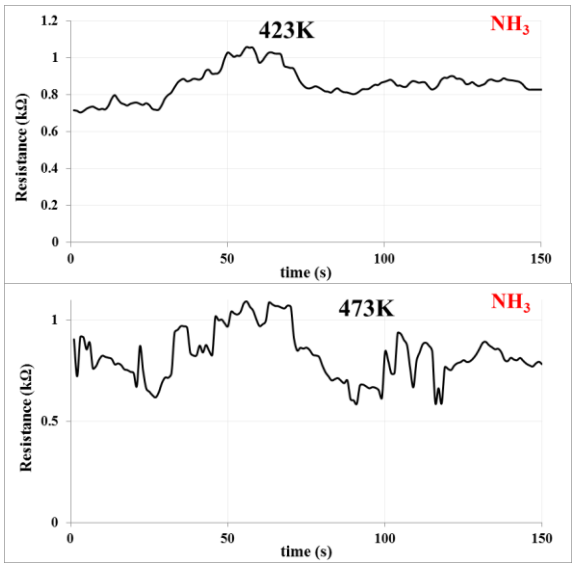

Fig. (3) The resistance versus time for pristine CeO_2/c-Si at 303, 373, 423 and 473K

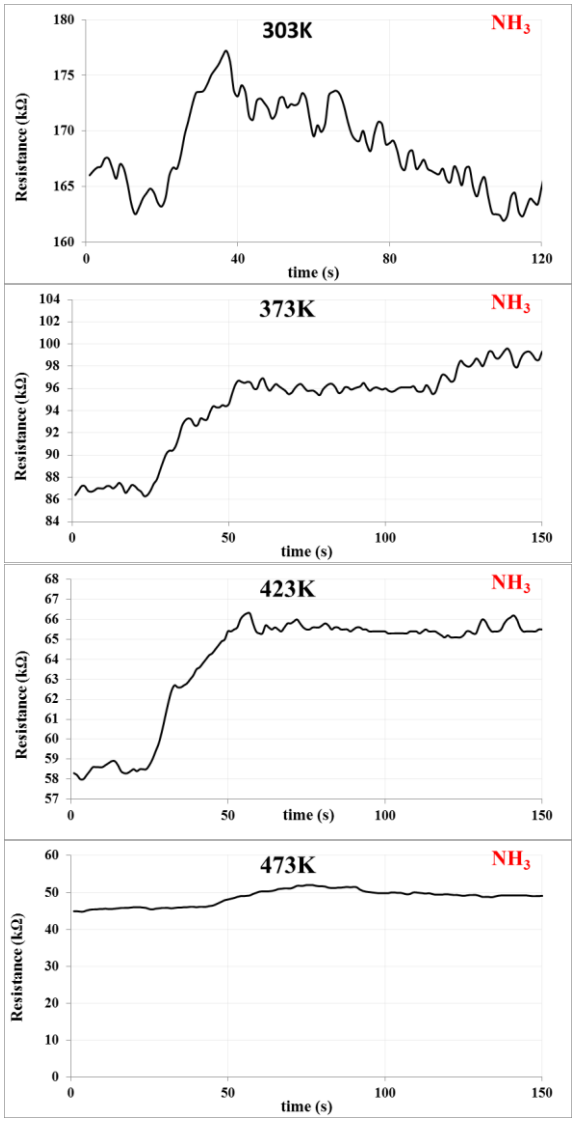

Fig. (4) The resistance versus time for (CeO_2:3%Eu_2O_3)/c-Si at 303, 373, 423 and 473K

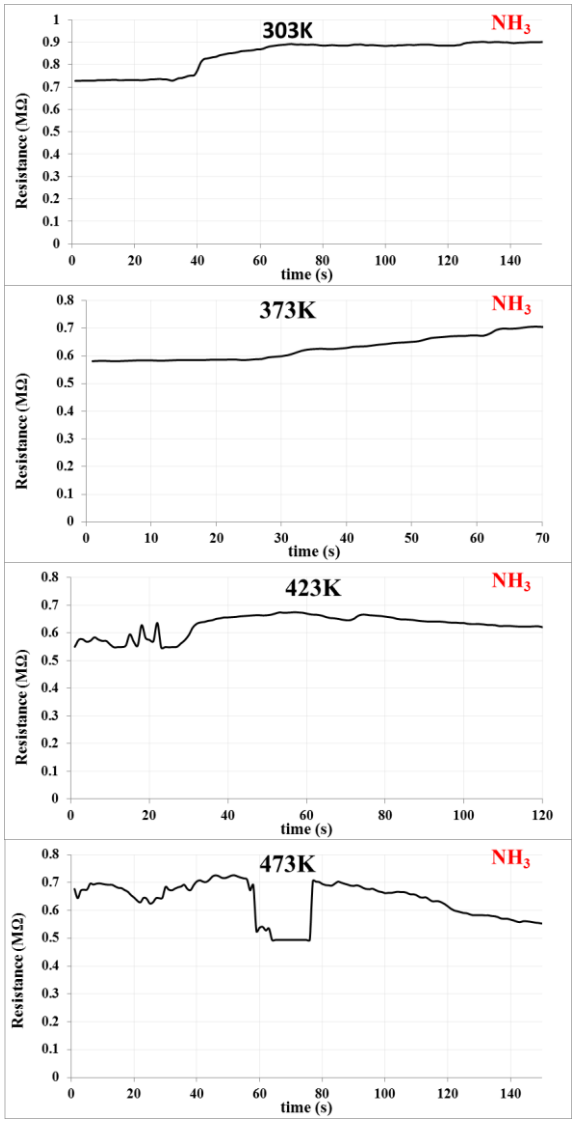

Fig. (5) The resistance versus time for (CeO_2:5%Eu_2O_3)/c-Si at 303, 373, 423 and 473K

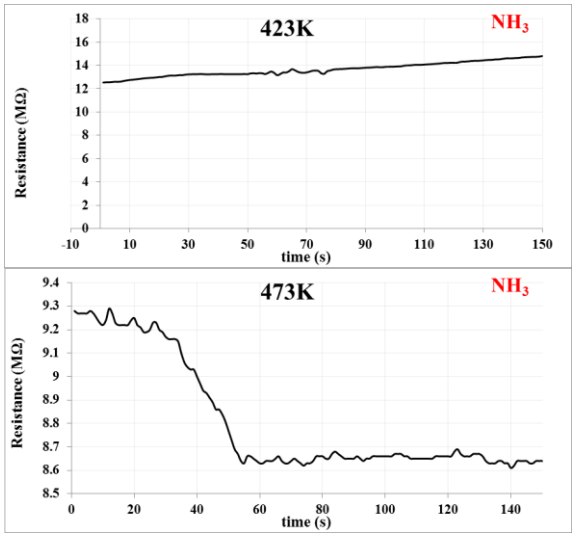

Fig. (6) The resistance versus time for (CeO_2:7%Eu_2O_3)/c-Si at 423 and 473K

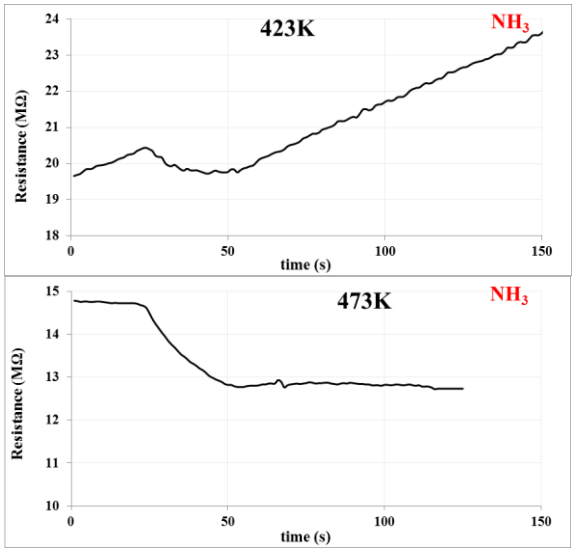

Fig. (7) The resistance versus time for (CeO_2:9%Eu_2O_3)/c-Si at 423 and 473K

Table (3) Values of sensitivity, response and recover times for pristine CeO_2 and (CeO_2: %Eu_2O_3)/c-Si

Doping Ratio (%)	Temperature (K)	Sensitivity (%)	Response Time (s)	Recovery Time (s)
0	303	29.7	30.6	85.5
	373	41.0	26.1	85.5
	423	39.1	28.8	49.5
	473	54.4	27.0	44.1
3	303	6.0	11.7	75.6
	373	11.3	29.7	87.3
	423	13.2	31.5	85.5
	473	13.3	39.6	52.2
5	303	19.7	31.5	123.3
	373	19.1	37.8	77.4
	423	18.2	28.8	42.3
	473	14.0	23.4	46.8
7	303	-	0.0	0.0
	373	-	0.0	0.0
	423	4.2	36.0	76.5
	473	5.8	25.2	87.3
9	303	-	0.0	0.0
	373	-	0.0	0.0
	423	2.4	24.3	92.7
	473	12.9	27.9	62.1

To test how well the prepared gas sensors could detect NH_3 gas, their resistance was measured as a function of time as in figures (8-11). The CeO_2:In_2O_3 sensors with doping ratios (0, 3, 5, 7 and 9%) similarly exhibited an increase in resistance as the sensors were exposed to the detecting gas, resulting in the formation of p-type semiconductors. The ratio of 7% In_2O_3 was the optimal doping ratio for sensor material which provided the highest sensitivity for NH_3. At working temperature of 373K, the sensor demonstrated good desorption and adsorption to NH_3 gas. The lowest response times were 1.6 s at 303 K temperature and 9% In_2O_3doped ceria. In_2O_3 clearly boosts sensitivity for sensors with low doping ratios while decreasing sensitivity for sensors with large doping ratios. The basic concept of increasing the sensitivity of semiconductor materials through doping with metal oxides was previously discussed by Hasan [21].

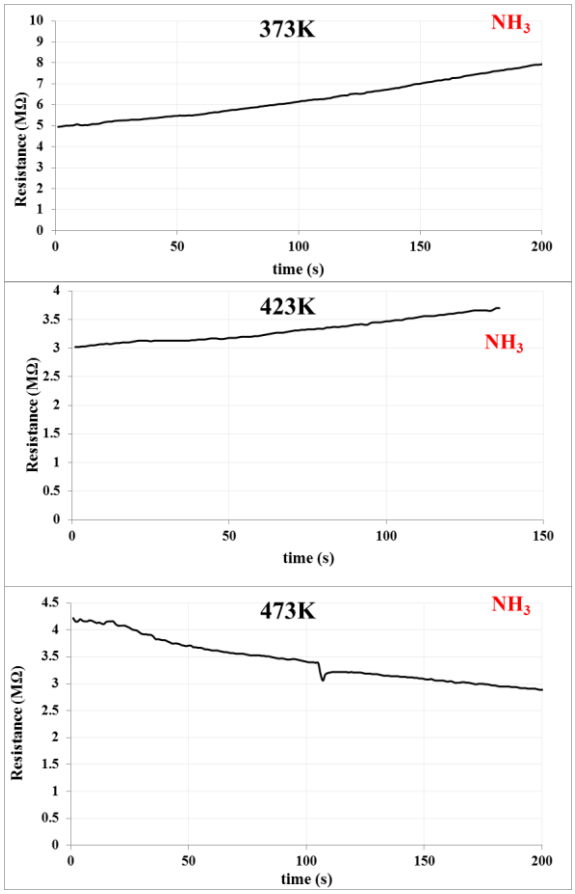

Fig. (8) The resistance versus time for (CeO_2:3%In_2O_3)/c-Si at 373, 423 and 473K

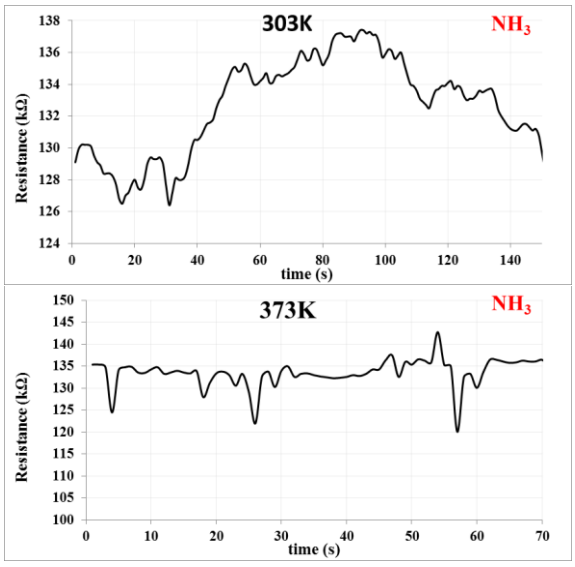

 ISSN (print) 1813-2065, (online) 2309-1673

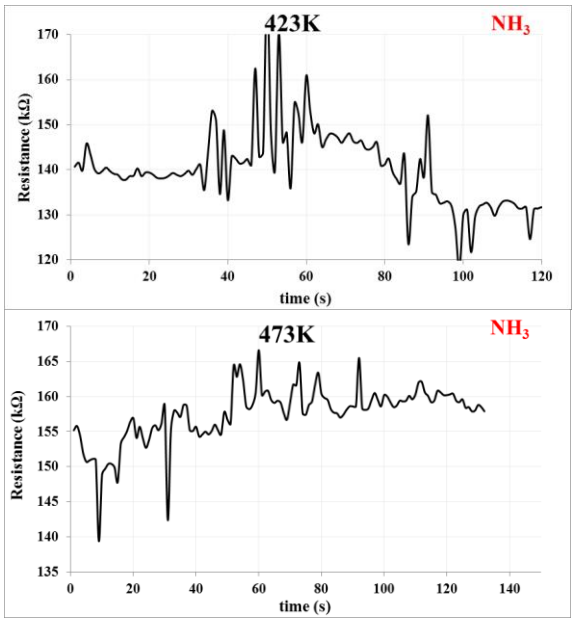

Fig. (9) The resistance versus time for (CeO_2:5%In_2O_3)/c-Si at 303, 373, 423 and 473K

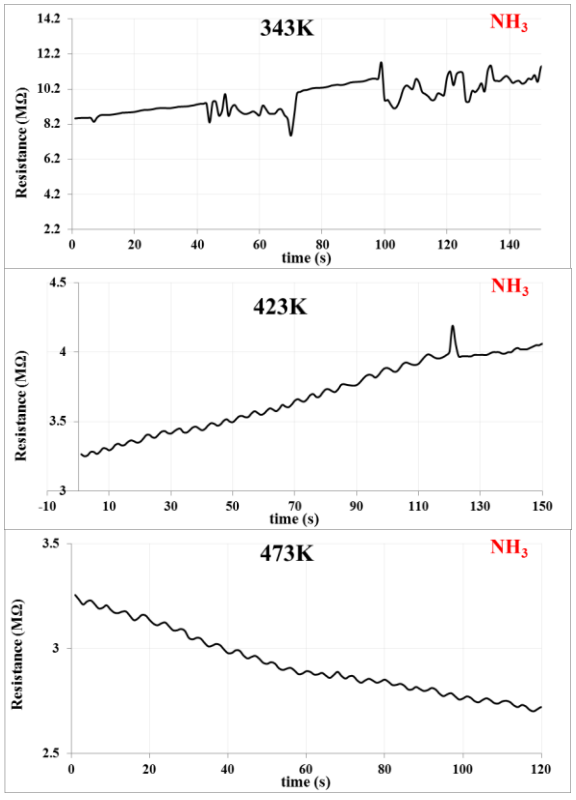

Fig. (10) The resistance versus time for (CeO_2:7%In_2O_3)/c-Si at 343, 423 and 473K

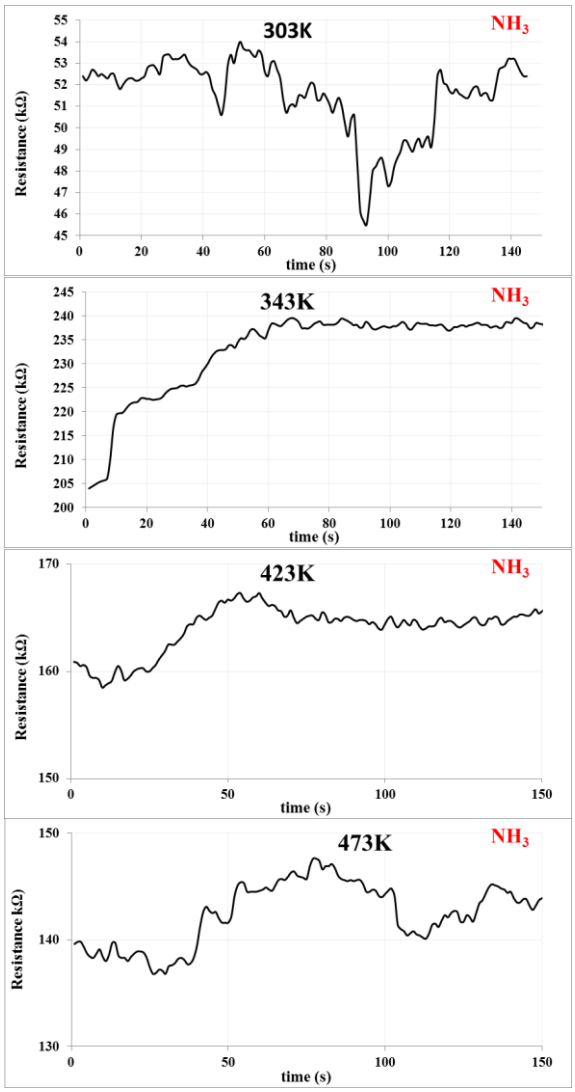

Fig. (11) The resistance versus time for (CeO_2:9%In_2O_3)/c-Si at 303, 343, 423 and 473K

Table (4) Values of sensitivity, response and recover times for pristine CeO_2 and (CeO_2:In_2O_3)/c-Si

Doping Ratio (%)	Temperature (K)	Sensitivity (%)	Response Time (s)	Recovery Time (s)
0	303	29.7	30.6	85.5
	373	41.0	26.1	85.5
	423	39.1	28.8	49.5
	473	54.4	27.0	44.1
3	303	-	-	-
	373	5.4	27.0	42.3
	423	1.6	25.2	46.8
	473	9.1	25.2	44.1
5	303	4.4	5.1	117.6
	373	6.7	8.1	122.5
	423	6.9	8.6	127.1
	473	1.3	1.9	140.8
7	303	-	-	-
	373	10.1	22.5	63.9
	423	4.1	27.0	44.1
	473	5.9	27.0	44.1
9	303	3.4	1.6	45.5
	373	7.2	14.5	208.7
	423	4.5	6.5	146.4
	473	5.3	6.6	125.8

4. Conclusions

The average diameter increases by increasing of doping ratio while the average roughness change in reverse manner. The sensitivity of (CeO_2:Eu_2O_3)/c-Si is higher than those of (CeO_2:In_2O_3)/c-Si. The optimum sensitivity is 54.4% and 19.7% obtained from undoped ceria and (CeO_2:3%Eu_2O_3)/c-Si at 473 and 303 K, respectively. The results declare that CeO_2 has the maximum response to NH_3 at optimal temperature of 473 K which indicates that CeO_2 doped with Eu_2O_3 and In_2O_3 is a good reducing gas sensing material. However, the findings of other researchers referred that optimal temperature of CeO_2 is 1073 K, and the response/recovery time are long [10]. The reduction of optimal temperature and improving response and return time represents a great challenge for the researchers.

References

[1] G.J. Cadena, J. Riu and F.X. Rius, "Gas sensors based on nanostructured materials", *Analyst.*, 132 (2007) 1083-1099.
[2] G. Korotcenkov, "Metal oxides for solid-state gas sensors", *Mater. Sci. Eng.*, 139 (2007) 1-23.
[3] G.D. Francia, B. Alfano and V.L. Ferrara, "Conductometric Gas Nanosensors", *J. Sens.*, 10 (2009) 13-??.
[4] J.L.F.D. Silva et al., "Hybrid functionals applied to rare-earth oxides: The example of ceria", *Phys. Rev. B*, 75 (2007) 045121.
[5] D. Tibiletti et al., "DFT and *in situ* EXAFS Investigation of Gold/Ceria−Zirconia Low-Temperature Water Gas Shift Catalysts: Identification of the Nature of the Active Form of Gold", *J. Phys. Chem. B*, 109 (2005) 22553-22559.
[6] T.T. Yan et al., "Facile synthesis, characterization, formation mechanism and photoluminescence property of Eu_2O_3 nanorods", *J. Alloys Comp.*, 487 (2009) 483-488.
[7] S. Kumar, R. Prakash and V.K. Singh, "Synthesis, Characterization, and Applications of Europium Oxide: A Review", *Rev. Adv. Sci. Eng.*, 4 (2015) 247-257.
[8] Q. Wan et al., "High-Performance Transparent Conducting Oxide Nanowires", *Nano Lett.*, 6 (2006) 2909-2915.
[9] F. Laatar, A. Harizi and H. Ezzaouia, "Optical and Optoelectronic Properties Enhancement of Porous Silicon Treated with Indium Oxide", *J. Phys. Chem. Solid.*, 12 (2020) 373-380.
[10] W. Zhang et al., "Interconnected CeO_2 Nanofibers for Enhanced CO Gas Sensing", *Hindawi J. Sens.*, 7 (2022) 3097440.
[11] W. Shi et al., "Photoelectric characteristics of rare earth element Eu-doped MoS_2 thin films", *Opt. Commun.*, 406 (2018) 50-54.
[12] M. Wang et al., "Crystal structure, morphology and luminescent properties of rare earth ion-doped $SrHPO_4$ nanomaterials", *J. Rare Earths*, 33 (2015) 355-360.
[13] K. Pooryusef and H. Kangarlou, "Indium Oxide as a material for biological applications; structural properties and biocompatibility", *Biol. Forum – An Int. J.*, 7 (2015) 799-801.
[14] S.R. Morrison, "Selectivity in semiconductor gas sensors", *Sens. Actuat. B: Chem.*, 12 (1987) 425-440.
[15] N. Yamazoe, G. Sakai and K. Shimanoe, "Oxide semiconductor gas sensors", *Catal. Surv. from Asia*, 7(1) (2003) 63-75.
[16] M. Verma and V. Gupta, "SnO_2-CuO Nanocomposite Thin Film Sensor For Fast Detection of H_2S Gas", *J. Exp. Nanosci.*, 8 (2013) 326-331.
[17] C. Wang et al., "Metal Oxide Gas Sensors: Sensitivity and Influencing Factors", *Sensors*, 10 (2010) 2088-2106.
[18] L. Liang et al., "Microstructural, Optical, and Electrical Properties of SnO Thin Films Prepared on Quartz Via a Two-Step Method", *ACS Appl. Mater. Interfaces*, 4 (2010) 1060-1065.
[19] A. Chowdhuri, V. Gupta and K. Sreenivas, "Response Speed of SnO_2-Based H_2S Gas Sensors with CuO Nanoparticles", *Appl. Phys. Lett.*, 84 (2004) 1180-1182.
[20] K. Sun et al., "Low-Operating-Temperature NO_2 Sensor Based on a CeO_2/ZnO Heterojunction", *mdpi Sensors*, 21(24) (2021) 8269-8281.
[21] B.A. Hasan, "SnO_2-doped In_2O_3 thin films as reducing gas sensors", *IOP Conf. Ser.: Mater. Sci. Eng.*, 928 (2020) 072011.

 ISSN (print) 1813-2065, (online) 2309-1673 PRINTED IN IRAQ

IRAQI JOURNAL OF APPLIED PHYSICS
Vol. 19, No. 3A, July-August 2023, pp. 19-24

Structural Properties of CuPc:(Au,Ag) NPs Thin Films Deposited by Spin Coating Technique

Ahmad Gh. Ahmad[1]
Adnan R. Ahmad[1]
Ameer F. Abdulameer[2]

[1] *Department of Physics, College of Education for Pure Sciences, Tikrit University, Tikrit, IRAQ*
[2] *Department of Physics, College of Science, University of Baghdad, Baghdad, IRAQ*

In this paper, copper phthalocyanine (CuPc) thin films doped with gold (Au) and silver (Ag) nanoparticles (NPs) were prepared using spin coating technique on glass substrates. The gold and silver nanoparticles were prepared by pulsed-laser ablation (PLA) technique. The transmission electron microscopy (TEM) indicated that these nanoparticles were primarily spherical and their sizes were determined to be in the range 7-43 nm for Au NPs, and 12-50 nm for Ag NPs. The structural characteristics were analyzed with x-ray diffraction (XRD), field-emission scanning electron microscopy (FE-SEM), and energy-dispersive x-ray spectroscopy (EDX). The XRD patterns confirmed the presence of a polymorphism structure predominated by a CuPc phase with a plane $(\bar{1}01)$ orientation preference at 2θ~7.1°. The FE-SEM used to investigate the structural formation of these films has shown that CuPc thin films have granular nature stacking. On the other hand, the elemental composition of films was confirmed by EDX analysis, which revealed compositional uniformity of the detected components and the (Au, Ag) NPs were loaded throughout the CuPc films.

Keywords: Structural properties; Thin film; Copper phthalocyanine; Nanoparticles
Received: 15 February 2023; **Revised:** 21 March 2023; **Accepted:** 28 March 2023

1. Introduction

Recently, organic thin films have played a key role in the discovery of novel materials for optoelectronics and their different applications [1]. One example is metallic phthalocyanine (MPc) thin films, which can be deposited on a solid substrates utilizing a variety of techniques (thermal evaporation, evaporation from solutions, chemical spray, and spin coating) [2]. Copper phthalocyanine (CuPc) is a p-type well-known organic semiconductor that is also considered to be among the most promising candidates for the applications of semiconducting materials. This is due to the fact that these materials possess important characteristics, such as favorable energy gaps, high thermal and chemical stabilities, high molecular symmetry [3,4], and thus, can be employed as a building block for a wide range of systems such as organic field-effect transistors (OFETs) [5], gas sensors [6], photovoltaic cells [7], and organic light emitting diodes (OLEDs) [8]. Most of these applications depend on the electrical characteristics and some of them demands knowledge of the molecular and crystalline structures. The dependency on crystalline structure becomes much more relevant if the material exists in several crystalline forms [9,10]. Many years ago, researchers have investigated the possibility of using metallic nanoparticles, such as gold, silver or copper, to improve the performance of optoelectronics devices in different applications [11]. Typically, thin films are doped with metallic nanoparticles to control the optical and electrical properties, such as the optical energy gap and electrical conductivity. Metallic nanoparticles often exhibit unique chemical and physical properties formed with specific characteristics related to size and shape. One more important feature of metal nanoparticles is their high surface area-to-volume ratio, which is important for sensing and photovoltaics applications [12]. This ratio and the quantum size effect cause nanomaterials to have unique characteristics compared to their bulk counterparts. As a result, a wide range of nanoscale devices employing metallic nanoparticles are rapidly developed [13]. The CuPc thin films are commonly prepared using thermal evaporation technique [14,15] due to its low solubility in organic solvents. There are few reports on the preparation of CuPc thin films by spin coating [16,17].

In this paper, we discuss the structural characteristics of CuPc thin films prepared by spin coating technique and doped with gold and silver nanoparticles.

2. Experimental Part

The organic material used in this study is CuPc (99%) powder supplied by Sigma Aldrich and used without further purification. CuPc powder of 125 mg was dissolved in 25 mL chloroform with ratio of 5:1 milligrams per milliliter, stirred by a magnetic stirrer continuously for 72 hours. Filters of 0.45 μm were used for the filtering and to remove any contaminant or undissolved material and get homogenous solution. The glass substrates were ultrasonically

cleaned for 10 minutes in deionized water, acetone, and alcohol.

The gold and silver sheets (99.99% pure) were used to prepare five alloys with different ratios. Alloys were manufactured using metal casting technology at temperature range of 962-1065°C. Alloys with a dimeter of 1 cm and thickness of 1 mm were obtained with different concentrations of Au (0, 0.25, 0.5, 0.75 and 1 wt.%).

In order to obtain Au NPs or Ag NPs suspended in chloroform, pulsed-laser ablation (PLA) technique was used to ablate the gold and silver nanoparticles from their alloys. Each of the five alloys was put in a glass cell containing chloroform, then, a solid-state Nd:YAG laser (1064nm fundamental wavelength, 8ns pulse duration, 1Hz repetition rate, and 80mJ energy) was used as an irradiation source for ablation of the gold and silver nanoparticles from their alloys. The laser pulses were focused on various regions of the alloy's surface. The layer of chloroform covering the alloy surface was 8mm thick and 2mL volume. TEM was used for determination of average size of the (Au,Ag)NPs suspended in chloroform.

In order to prepare a nanocomposite solution of CuPc embedded with (Au,Ag)NPs, 1 mL of different ratios of (Au,Ag)NPs solutions were added to 1mL of CuPc solution. Ultrasonic device was used to suspend and disperse the nanoparticles in solution before deposition process. Thin films were deposited using a VTC-100 spin coater on glass substrates. Before depositing the solution, the spin coater was set at 500 rpm for 10 seconds (acceleration up), 2500 rpm for 30 seconds (stable state), and 500 rpm for 10 seconds (acceleration down). A 50 µL of the solution of each sample was poured onto the substrate. Samples were dried to 80°C for 15 min in electric oven to evaporate the solvent and in order to improve the adherence of nanocomposite films to the glass substrate. The resulting films appeared to be of high quality with a uniform thickness that was suitable for studying the film's physical characteristics. Using a Shimadzu XRD 6000 x-ray diffractometer (1.5405Å Cu-Ka radiation source, scan angle 5-60°, scan speed 10.00 deg/min, and step size 0.0400 deg), the structures of these films were studied.

Bragg's law states that the route difference between two diffracted rays of the same phase equals integer numbers of x-ray wavelength, which can be expressed as [18]:

$$n\lambda = 2\,d\,sin\,\theta_B \qquad (1)$$

where θ_B is Bragg's angle, λ is the wavelength, d is the inter-planar distance, and n is the spectral order (n=1, 2, 3, …)

Scherrer's equation was used to determine the grain size (G.S) of the crystalline materials [19]:

$$G.S = \frac{0.9\lambda}{\beta cos\theta} \qquad (2)$$

where β refers to the full-Width at half maximum (FWHM) in radians

The morphology and dispersion of (Au,Ag)NPs in chloroform solvent were investigated using a JEOLJEM-1011 TEM at 120kV acceleration voltage. The images of the prepared thin films were recorded using a Zeiss Supra 35 FE-SEM at magnification of up to 1,000,000x. Also, the energy-dispersive x-ray spectroscopy (EDS) was utilized to examine the chemical composition of films.

Measurements of films thickness using an optical interferometer (fringes method using 632.8nm He-Ne laser) yielded a value of 100±5 nm according to the following equation [20]:

$$t = \frac{\lambda \Delta x}{2x} \qquad (3)$$

where x is the fringe width, Δx is fringe's shift and λ is the wavelength of laser light

3. Results and Discussion

The XRD patterns of pure CuPc and CuPc:(Au/Ag)NPs thin films deposited by spin coating technique are shown in Fig. (1). All films exhibit polymorphism structure, as shown by the XRD patterns, which exhibit variations in structure between polycrystalline and amorphous phases. Thin films exhibit a significant reflection at $(\bar{1}01)$ orientation at 2θ≈7.10°. This peak belongs to the CuPc phase with a monoclinic crystal structure, which is characteristic of the majority of MPc films [14].

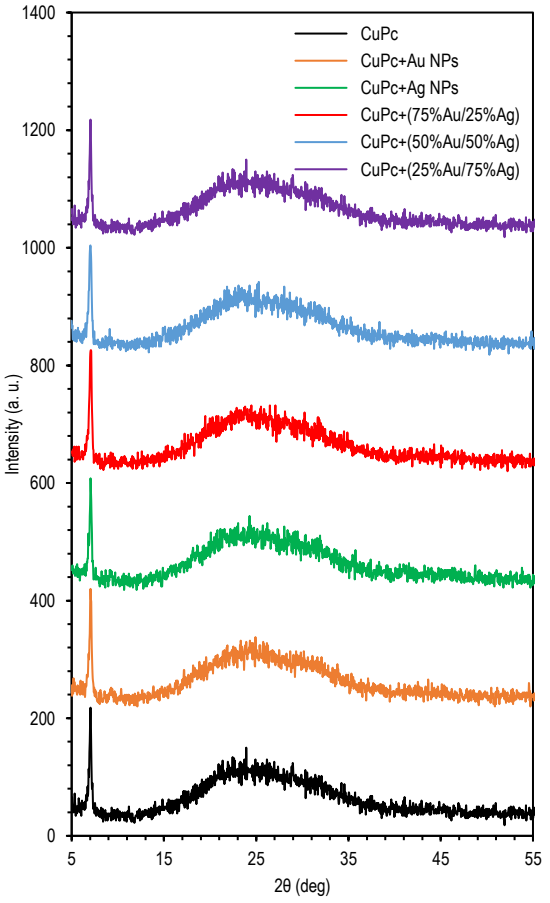

Fig. (1) XRD patterns of pure CuPc and CuPc:(Au/Ag)NPs thin films

 ISSN (print) 1813-2065, (online) 2309-1673

A wide hump at 2θ≈25º in Fig. (1) may have been caused by the glass substrate on which the CuPc film were deposited. It is noteworthy the NPs have no obvious effects on the crystal structure of CuPc, therefore, the CuPc:(Au/Ag)NPs films demonstrate the same polycrystalline structure as pure CuPc thin films since no substantial shift in peak location was found. Table (1) lists the the preferred orientations and crystalline size estimated from FWHM values for the relevant peaks in pure CuPc and CuPc:(Au/Ag)NPs films.

Table (1) Structural parameters of CuPc thin films at $(\bar{1}01)$ orientation prepared by spin coating technique

Sample	2θ (deg)	d (Å)	FWHM (deg)	D (nm)
CuPc	7.174	12.321	0.295	26.953
CuPc+AuNPs	7.049	12.539	0.157	50.547
CuPc+AgNPs	7.072	12.499	0.275	28.879
CuPc+ (75Au:25Ag)%NPs	7.039	12.557	0.157	50.547
CuPc+ (50Au:50Ag)%NPs	7.042	12.552	0.236	33.684
CuPc+ (25Au:75Ag)%NPs	7.069	12.504	0.196	40.428

The shape, size distribution, morphology, and particle size of the AuNPs and AgNPs suspended in chloroform were confirmed using TEM. High-resolution TEM images of NPs are shown in Fig. (2). Small black particles could be seen in the images because of the existence of NPs. We note that most particles are nearly spherical in shape and in the monodispersing state, uniform distribution with no agglomeration. The particle size varies from 7 to 43 nm for AuNPs and from 12 to 50 nm for AgNPs. The small histogram in Fig. (2) displays the size distribution of the NPs with the prevalent grain size being around 20nm for AuNPs and 24nm for AgNPs.

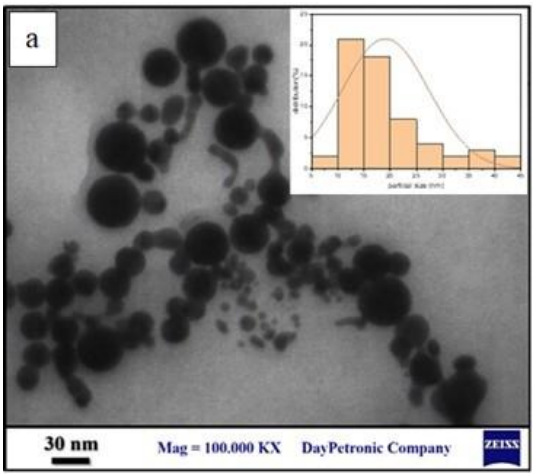

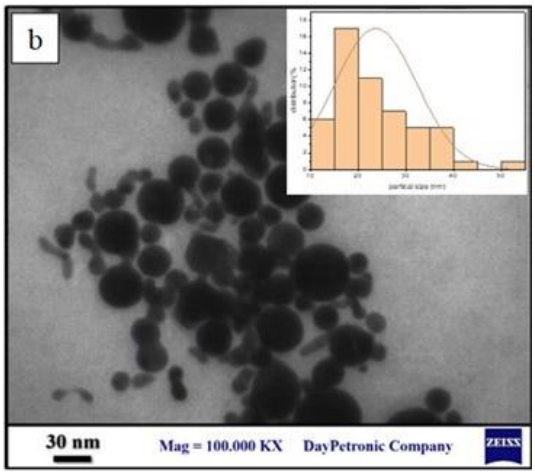

Fig. (2) TEM image of (a) Au NPs, and (b) Ag NPs

Figure (3) displays FE-SEM images with different magnifications of pure CuPc and CuPc:(Au/Ag)NPs thin films. The morphological feature of the thin films clearly showed clusters of spherical nanoparticles, which have a large surface area in relation to their volume, as seen in Fig. (3). It is also worth noting that the film deposited on substrates formed dense, uniform nanoparticles which have granular nature stacking and are oriented arbitrarily with ordinary distribution of grain concentration and are well adhered to the glass substrate.

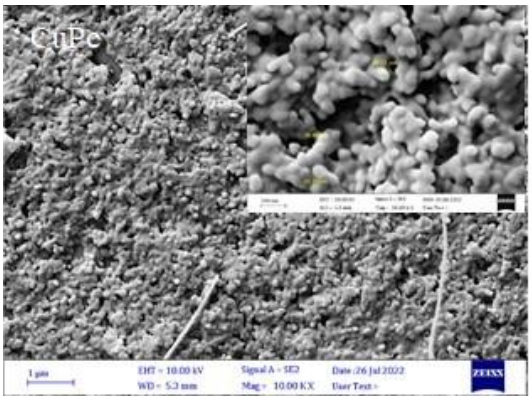

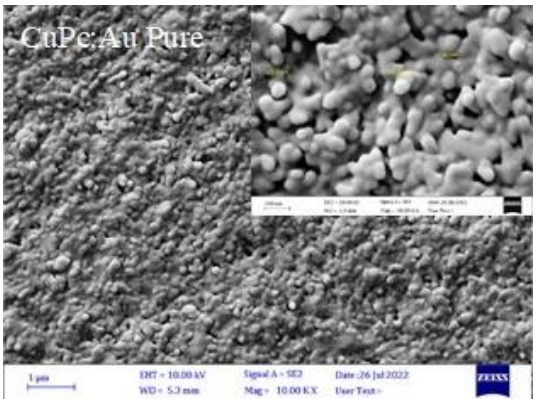

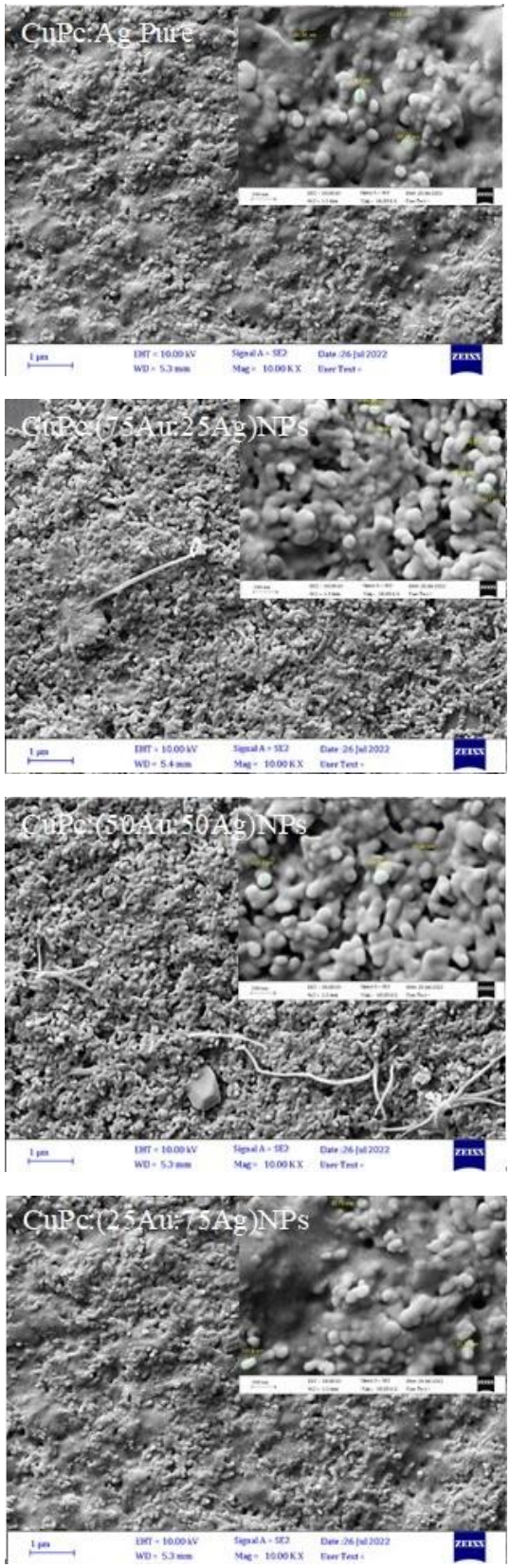

Fig. (3) FE-SEM images of pure CuPc, and CuPc:(Au/Ag)NPs thin films

In order to determine the elemental compositions of pure CuPc and CuPc:(Au/Ag)NPs thin films deposited on glass substrates, an EDX analysis was carried out, which also allows to know the presence of any other impurities. Figure (4) displays the EDX spectra of pure CuPc and CuPc doped with different concentrations of Au (0, 0.25, 0.5, 0.75, and 1 wt.%). These spectra showed good compositional uniformity of the observed elements such as (C, O and Cu) of CuPc due to the organic structure of the MPs materials used. In addition, they showed that the gold and silver nanoparticles were loaded throughout CuPc films. A strong peaks for the carbon have been observed of all samples in the spectra because of the chemical composition of the stoichiometry $C_{32}H_{16}N_8Cu$ compound, which indicates that carbon is an essential element in the structure of organic materials MPs. Hydrogen is not often observed in all spectra due to its low atomic weight. Also, nitrogen peak cannot be seen in the EDX spectra most likely because of the detection limitations of roughly 1 wt.% and may stay undetected because of overlapped peaks [21]. The element Si and excess amount of O are belonging to glass substrate.

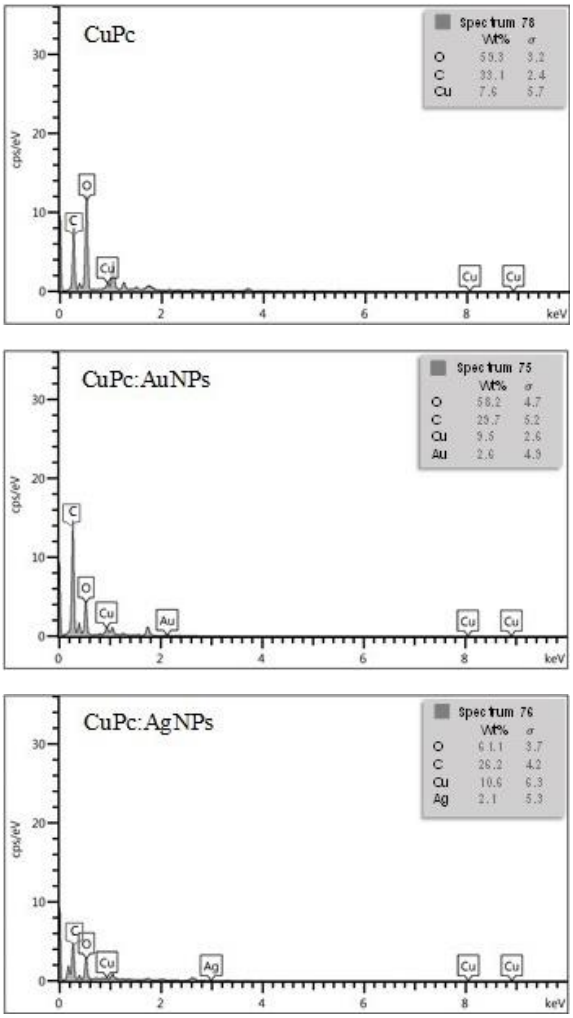

 ISSN (print) 1813-2065, (online) 2309-1673

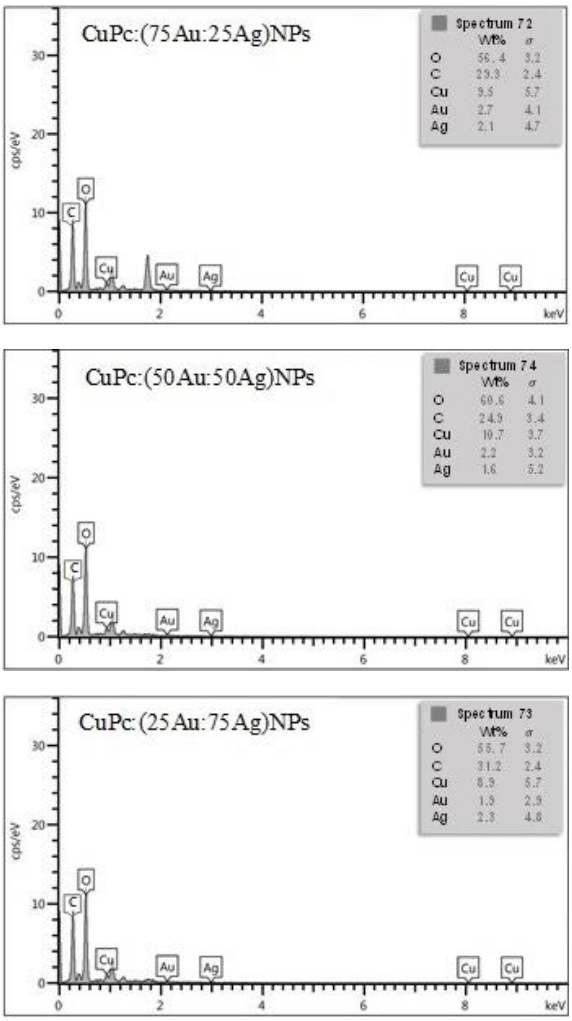

Fig. (4) EDS spectra of pure CuPc and CuPc:(Au/Ag)NPs thin films

4. Conclusions

In concluding remarks, the copper phthalocyanine (CuPc) thin films were deposited on glass substrates by using spin coating technique and successfully doped with gold and silver nanoparticles with good homogeneity. Results have confirmed the presence of a single, prominent diffraction peak at $(\bar{1}01)$ plane, which is typical for most MPc films. They also showed that thin films have granular nature stacking and well adhered to the substrate. Good uniform elemental composition of the prepared CuPc:(Au,Ag)NPs films was confirmed.

References

[1] B.R. Sridevi, P.A. Hoskeri and C.M. Joseph, "Effect of annealing on the optical, structural and electrochromic properties of vacuum evaporated manganese phthalocyanine thin films", *Thin Solid Films*, 723 (2021) 138584.

[2] M. Szybowicz et al., "The molecular structure ordering and orientation of the metallophthalocyanine CoPc, ZnPc, CuPc, and MgPc thin layers deposited on silicon substrate, as studied by micro-Raman spectroscopy", *J. Mater. Sci.*, 46(20) (2011) 6589-6595.

[3] H.A. Afify et al., "Effect of thermal annealing on the structural and optical properties of spin coated copper phthalocyanine thin films", *J. Mol. Struct.*, 1098 (2015) 161-166.

[4] A. Zawadzka et al., "Structural and nonlinear optical properties of as-grown and annealed metallophthalocyanine thin films", *Thin Solid Films*, 545 (2013) 429-437.

[5] L. Vijayan et al., "Low power organic field effect transistors with copper phthalocyanine as active layer", *J. Sci. Adv. Mater. Devices*, 3(3) (2018) 348-352.

[6] M.K. Rana, M. Sinha and S. Panda, "Gas sensing behavior of metal-phthalocyanines: Effects of electronic structure on sensitivity", *Chem. Phys.*, 513 (2018) 23-34.

[7] A.M. Ali et al., "Improving the efficiency of the organic solar cell (CuPc/C60) via PEDOT: PSS as a photoconductor layer doped by silver nanoparticles", *Results in Physics*, 16 (2020) 102819.

[8] Y.-Y. Ma et al., "Doped copper phthalocyanine via an aqueous solution process for high-performance organic light-emitting diodes", *Org. Electron.*, 68 (2019) 236-241.

[9] K. Onlaor et al., "Electrical bistable properties of copper phthalocyanine at different deposition rates", *Solid. State. Electron.*, 72 (2012) 60-66.

[10] O. Berger et al., "Studies on phase transformations of Cu-phthalocyanine thin films", *J. Mater. Sci. Mater. Electron.*, 11(4) (2000) 331-346.

[11] V. Kumar and H. Wang, "Plasmonic Au nanoparticles for enhanced broadband light absorption in inverted organic photovoltaic devices by plasma assisted physical vapour deposition", *Org. Electron.*, 14(2) (2013) 560-568.

[12] O.V. Molodtsova et al., "Noble metal nanoparticles in organic matrix", *Appl. Surf. Sci.*, 506 (2020) 144980.

[13] K.S. Hamdan et al., "Effects of silver nanoparticles towards the efficiency of organic solar cells", *Appl. Phys. A*, 115(1) (2014) 63-68.

[14] M.T. Hussein, K.A. Aadim and E.K. Hassan, "Structural and surface morphology analysis of copper phthalocyanine thin film prepared by pulsed laser deposition and thermal evaporation techniques", *Adv. Mater. Phys. Chem.*, 6(4) (2016) 85-97.

[15] X. Ai et al., "Phase modification of copper phthalocyanine semiconductor by converting powder to thin film", *Appl. Surf. Sci.*, 428 (2018) 788-792.

[16] H. Hassan, N.B. Ibrahim and Z. Ibarahim, "Effects of annealing temperature on the optical properties and device performance of Ag/n-Si/CuPc/Ag solar cell prepared via spin coating method", *Sains Malaysiana*, 39(4) (2010) 627-

631.
[17] B. Wang et al., "Comparative gas sensing in copper porphyrin and copper phthalocyanine spin-coating films", *Sens. Actuat. B Chem.*, 152(2) (2011) 191-195.
[18] A.F. Abdulameer et al., "Structural, surface morphology and optical properties of annealing treated Copper Phthalocyanine doped Fullerene (CuPc: C60) thin films", *J. Phys.: Conf. Ser.*, 1795(1) (2021) 12068.
[19] P. Keeratithiwakorn et al., "Structural properties of copper phthalocyanine films grown by electrophoretic deposition process", *Mater. Today Proc.*, 4(5) (2017) 6194-6199.
[20] J. Park et al., "A review of thickness measurements of thick transparent layers using optical interferometry", *Int. J. Precis. Eng. Manuf.*, 20(3) (2019) 463-477.
[21] T. Potlog et al., "Synthesis and characterization of CuPc-PEPC composite thin films and photovoltaic devices by drop casting method", *Mater. Plast.*, 57(4) (2021) 134-144.

 ISSN (print) 1813-2065, (online) 2309-1673

IRAQI JOURNAL OF APPLIED PHYSICS
Vol. 19, No. 3A, July-August 2023, pp. 25-30

Structural, Optical and Electrical Properties of TiO_2:MoS_2 Thin Films Prepared by Pulsed-Laser Deposition Technique

Zeina S. Mahdi
Ghuson H. Mohammed

Department of Physics, College of Science, University of Baghdad, Baghdad, IRAQ

Titanium dioxide (TiO_2) films with different contents of molybdenum dioxide (MoS_2) (2, 4, 6, 8 and 10 wt.%) have been deposited on glass at room temperature by pulsed-laser deposition method using an Nd:YAG laser with 1064 nm wavelength, 400mJ energy and 200 shots. The structural, electrical, morphological, and optical characteristics of the deposited films were characterized. The effects of MoS_2 content in the deposited films on their characteristics were investigated. The films were polycrystalline and structurally hexagonal and the formation of rutile phase of TiO_2 was confirmed. The transmittance of the films was found to increase as the MoS_2 content is increased. Also, 0.02 wt.% MoS_2 content was the optimum as the largest crystallite size and highest roughness were achieved. The optical band gap of the deposited films was found to decrease with increasing MoS_2 content while the refractive index, dielectric constant, and extinction coefficient were measured at 300 nm.

Keywords: TiO_2:MoS_2; PLD technique; Optical properties; Hall effect
Received: 06 April 2023; **Revised:** 01 May 2023; **Accepted:** 08 May 2023

1. Introduction

Transparent conducting oxides (TCOs) are semiconductors, including titanium dioxide (TiO_2), those absorb ultraviolet light, have low electrical conductivity, and are highly transparent in the visible region of electromagnetic spectrum [1]. TiO_2 is also belonging to the II-VI category of semiconductors. There are three different crystalline forms of TiO_2, namely rutile, anatase and brookite [2,3]. The anatase form of TiO_2 is the most common as a semiconductor due to its crystalline structure and higher band gap (3.2eV) compared to the rutile form (3eV). However, both anatase and rutile forms are suitable for use in sensing applications. White pigment, gas sensors, corrosion protection, and optical coatings examples of the industrial uses of the chemically inert TiO_2. It is also used in solar cell arrays [4], applications requiring high electrical resistance [6] and high dielectric constant [7], environmental cleanup [8,9], photocatalysis and self-cleaning surfaces [10,11], and antifungal treatment [12].

Molybdenum disulfide (MoS_2) is among the transition metal dichalcogenides (TMDs) family. It is made up of one molybdenum (Mo) atom and two sulfur (S) atoms [13]. The electrical and optical properties of layered structures of MoS_2 and other TMDs have been reported [14]. The distinct physical, chemical and electrical properties of this compound have attracted the attention of numerous researchers. It has a band gap of about 1.8 eV, which in thin structures, changes from an indirect gap to a direct gap; making it possible to downscale electronic devices [15,16]. Although MoS_2 has numerous applications across numerous industries, those involving applications like DNA and cancer studies are the most significant [17-20]. Optical sensors are another use of MoS_2, however, these are not as substantial as those are related to biological applications.

In this work, optically transparent TiO_2:MoS_2 thin films are grown on glass substrates by pulsed-laser deposition method. The structural, morphological, optical and electrical characteristics of these films are introduced.

2. Experimental Part

A molybdenum disulfide and titanium dioxide powders (99.99% purity) supplied by NanoShell Company were mixed at different quantities (2, 4, 6, 8, and 10 wt.%). The precursor powder was combined and crushed into 1.5 cm diameter and 0.2 cm thick pellets with a SPECAC hydraulic press at 6 tons pressure after blending in an agate mortar. Finally, the pellets were sintered for at 750 K for one hour in the air.

Using the produced pellets, thin films from $(TiO_2)_{1-x}(MoS_2)_x$ were deposited at room temperature onto glass substrates, which were cleaned with distilled water for 15 minutes using ultrasonic technique. The PLD method was used to deposit these thin films using an Nd:YAG laser with 1064nm wavelength and 400mJ energy. During the process, 200 laser pulses at a repetition frequency of 6Hz were applied to the targeted surface at a 45° angle. The

deposition process was performed at a chamber pressure of 0.1 mbar. The target and substrate were separated by 10 cm.

The XRD patterns of the deposited films were recorded by a Panalytical X'Pert Pro X-ray diffractometer (Cu-K, 0.154 nm) with scan range of 10-80°. Atomic force spectroscopy (AFM) was used for the examination of the surface morphology of the film. A metertech UV-vis-NIR spectrophotometer was used to record transmission and absorption spectra of the deposited films in the spectral range of 190-1100nm.

3. 3. Results and Discussion

Figure (1) shows the XRD patterns of the prepared $(TiO_2)_{1-x}(MoS_2)_x$ thin films with different concentrations of MoS_2 (x=0.02, 0.04, 0.06, 0.08, and 0.10 wt.%). According to the ASTM cards, the produced films are polycrystalline and tetragonal in structure for the rutile phase of TiO_2, while the MoS_2 is hexagonal. The characteristic peak at 2θ of 27.3° corresponds to the reflection from the (110) crystal plane of TiO_2 for the concentrations of 0.02 and 0.04 wt.%, while the peaks at 2θ values of 27.1° and 28.1° for 0.06 wt.% concentration correspond to the reflections from (110) and (004) crystal planes, respectively. The peaks at 2θ values of 27.4°, 28.4°, 32.9°, 33.6°, 39.4°, and 49.2° for concentrations of 0.08 and 0.10 wt.% correspond to the reflections from the planes (110), (004), (100), (101), (103) and (105), respectively, with new peak belonging to MoS_2. The crystallite size (C_s) of the films was calculated using Debye-Scherrer's equation as follows [21]:

$$C_s = \frac{0.9\,\lambda}{\beta \cos\theta} \qquad (1)$$

The strain (ε) can be determined using the following relation [22]:

$$\varepsilon = \frac{\beta_{hkl}}{4\,tan\theta} \qquad (2)$$

The dislocation density (δ) was determined as the length of the dislocation lines to the crystallite size as follows [23]:

$$\delta = \frac{1}{C_s^2} \qquad (3)$$

Table (1) presents the results obtained from the diffraction patterns of the prepared TiO_2:MoS_2 thin films. The data in Table (1) demonstrate that despite the increase in the microstrain and dislocation values following the increase in the MoS_2 content, the average crystallite size was reduced possibly due to the ability of MoS_2 phase to stop TiO_2 from growing new grains. Additionally, it is asserted that MoS_2 is substituted for TiO_2 in the TiO_2 lattice due to the smaller atomic radii of MoS_2 particles compared to those of TiO_2.

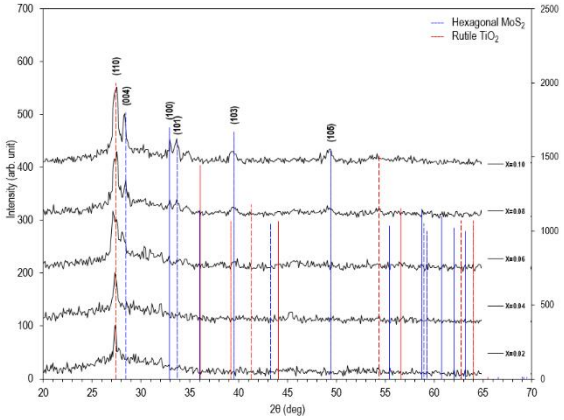

Fig. (1) XRD patterns of $(TiO_2)_{1-x}(MoS_2)_x$ thin films prepared at room temperature with different MoS_2 concentrations

The AFM results showed that the doping procedure with MoS_2 had a substantial impact on the surface characteristics of the produced TiO_2 films. The 3D AFM images of TiO_2:MoS_2 thin films shown in Fig. (2) and Table (2) showed the surface morphology of thin films grown on glass substrates at room temperature, as well as the grain size, average and root mean square (r.m.s.) roughness. It is easy to see the delicate morphology and roughness of the TiO_2:MoS_2 films. It is shown that the surface grains are much more uniform as the roughness decreases based on the $R_{r.m.s.}$ values.

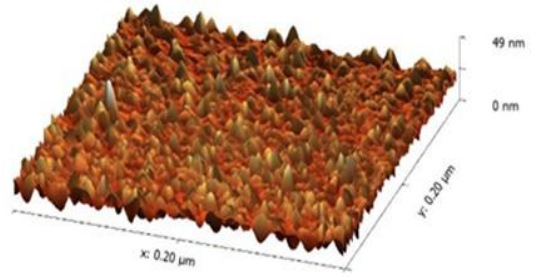

X = 0.02

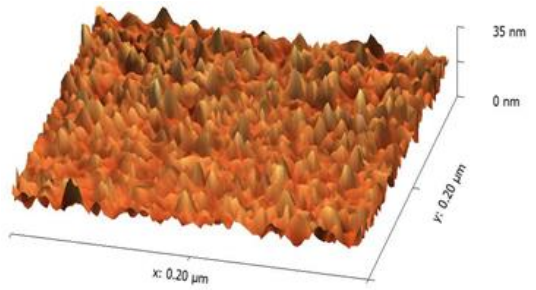

X = 0.04

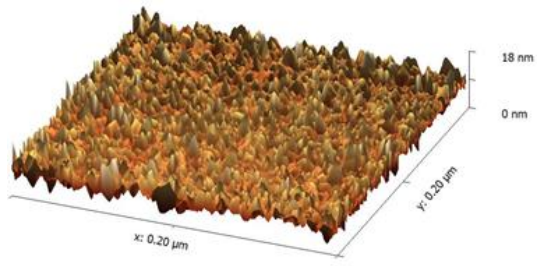

X = 0.06

 ISSN (print) 1813-2065, (online) 2309-1673

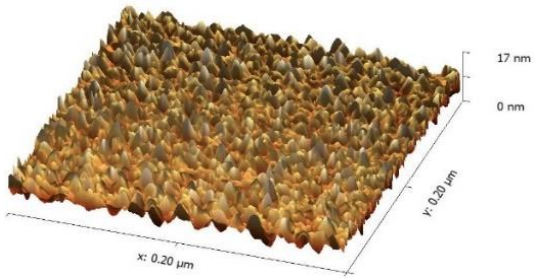

X = 0.08

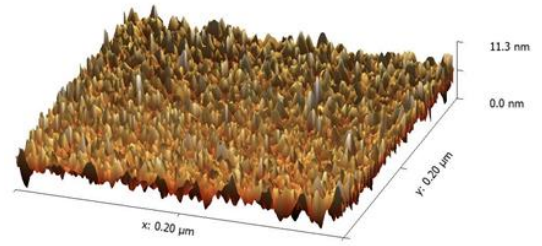

X = 0.10

Fig. (2) AFM-acquired surface features of $(TiO_2)_{1-x}(MoS_2)_x$ thin films prepared at room temperature with different MoS_2 concentrations

These results demonstrate that the values of the average grain size of the surface structures of the generated TiO_2 films decreases as the content of MoS_2 dopants is increased. Average and r.m.s. roughness values also changes as MoS_2 is added, with a maximum value of a MoS_2 ratio of 0.02%. The largest crystalline size and maximum roughness were achieved in the 0.02% MoS_2 ratio, hence, the films can be used to fabricate several devices, such as optoelectronic devices.

Table (2) values of average grain size, average roughness, and r.m.s. roughness of the $(TiO_2)_{1-x}(MoS_2)_x$ thin films prepared at room temperature with different MoS_2 concentrations

Sample	Avg. Grain Size (nm)	Avg. Roughness (nm)	R.M.S Roughness (nm)
0.02	40.48	9.45	4.02
0.04	32.50	7.91	3.44
0.06	31.17	7.23	1.88
0.08	20.49	3.38	1.72
0.10	8.86	1.52	1.38

The transmission and absorption spectra, refractive index, dielectric constant, extinction coefficient, and optical energy gap of the prepared TiO_2:MoS_2 thin films were measured and recorded in the spectral range of 300-1100 nm. Figure (3) showed the transmission spectra of TiO_2:MoS_2 thin films. The data in table (3) showed an increase in the transmittance with increasing MoS_2 content for all samples, while the absorbance decreases as the amount of MoS_2 increases. This is due to the formation of localized states in the band gap, which increases the sample's opacity to the incident light. This could be caused by an increase in the heavy atoms, which would increase the absorption. The decrease in transmission, on the other hand, might be caused by the appearance of levels close to the energy band gap, which causes the peak to shift to lower energies as earlier reported by [24].

The absorption coefficient can be calculated as shown in Fig. (4) using the following relation [25,26]:

$$\alpha = 2.303A/t \quad (4)$$

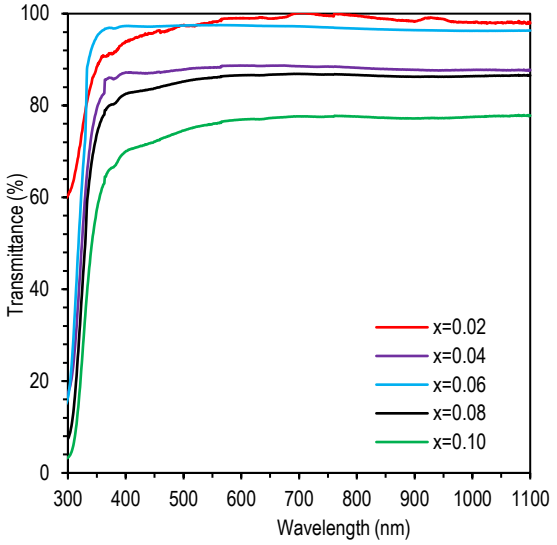

Fig. (3) Transmission spectra of prepared films with different MoS_2 concentrations

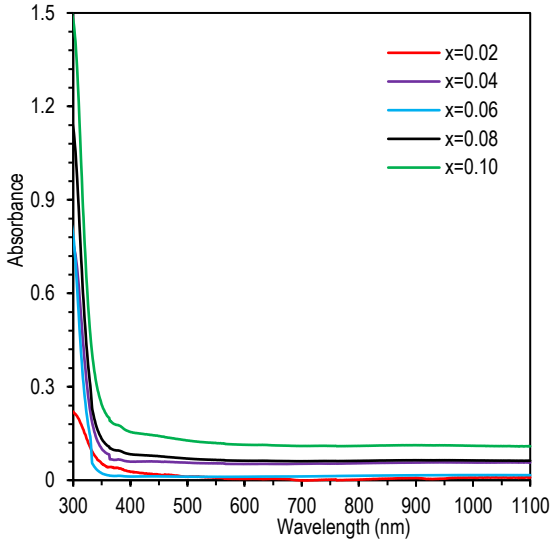

Fig. (4) Absorption spectra of prepared films with different MoS_2 concentrations

The following relation was used to calculate the optical energy gap (E_g) value of the prepared thin films [27]:

$$\alpha h\nu = B(h\nu - E_g)^r \quad (5)$$

where $h\nu$ is the incident photon energy, r is an exponent that describes the material's optical transitions, and B is a constant that inversely correlates with amorphous nature of the material

This phenomenon is due to the occurrence of band-to-band absorption that usually happens following the migration of an electron from the valence band to the conduction band, giving rise to a new pair of charge carriers (one electron and one

hole). TiO_2:MoS_2 films have excellent absorption and low transmission properties in the UV range (as seen in Fig. 5). In addition, table (3) showed that the band gap decreases with increasing MoS_2 content. For instance, when the MoS_2 content is increased from 0.02 to 0.10, the optical band gap dropped from approximately 3.92 to 3.80 eV. Being that it closely resembles what is available in the existing literature, this conclusion is tenable. However, the opacity of the material increased at higher MoS_2 content (x) due to the lowering of E_g (much more absorbance). This phenomenon can be explained by the observed increase in the density of localized states in the conduction or valence band that is ready to accept electrons and form optical energy gap tails that are attempting to fill the energy gap [28]. A smaller band gap may also be due to many-body interaction phenomena that occur between free carriers and charge carriers or ionized impurities [29,30].

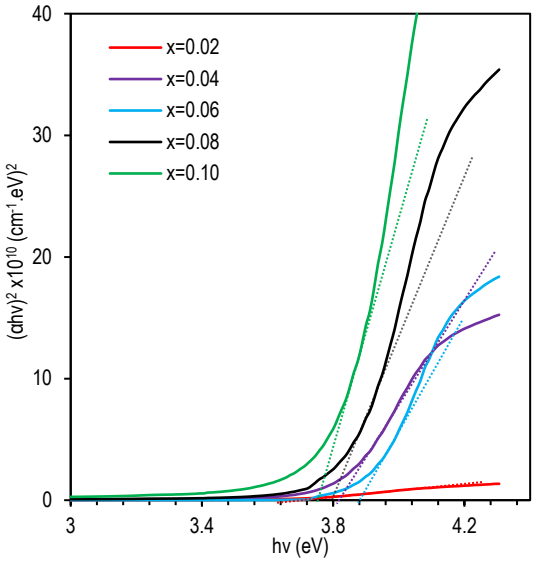

Fig. (5) Variation of $(\alpha hv)^2$ as a function of photon energy (hv) for $(TiO_2)_{1-x}(MoS_2)_x$ films at different MoS_2 concentrations

The extinction coefficient (k) can be estimated using the equation $k=\alpha\lambda/4\pi$, and it is obvious that its value rises as doping levels rise, as shown in table (3).

The variation of refractive index of TiO_2:MoS_2 films with wavelength in the range of 300-1100 nm is depicted in Fig. (7) and table (3). It is clear that as doping levels increase, the refractive index falls.

The complex optical refractive index of the prepared films can be described using the following relation [31]:

$$n^*=n-ik \quad (7)$$

The refractive index of the thin film can be roughly determined as follows [32]:

$$n=\frac{1+R}{1-R}+\sqrt{\frac{4R}{(1-R)2}-k^2} \quad (8)$$

The real (ε_r) and imaginary (ε_i) parts of the dielectric constant are measured using the following equations [33]:

$$\varepsilon_r = n^2-k^2 \quad (9)$$

$$\varepsilon_i = 2nk \quad (10)$$

The variations of these parts as functions of wavelength are shown in table (3). It can be seen from the table that as concentration increases, the imaginary part of the dielectric constant increases, and the real part decreases. This is because the extinction coefficient increases and the refractive index lowers as the incident wavelength increases.

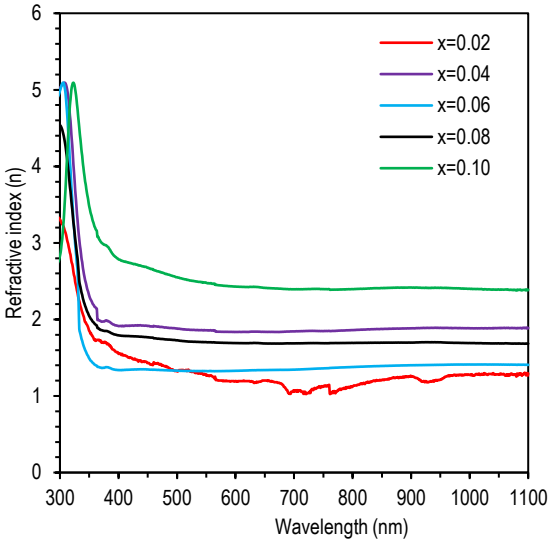

Fig. (7) Variation of refractive index as a function of wavelength for $(TiO_2)_{1-x}(MoS_2)_x$ films at different concentrations of MoS_2

Table (3) Transmittance, refractive index, absorption coefficient, extinction coefficient, and dielectric constant of the $(TiO_2)_{1-x}(MoS_2)_x$ thin films prepared in this work with different contents of MoS_2 at room temperature at 300nm

Sample	T_{max} (%)	α (cm^{-1})	k	n	ε_r	ε_i	E_g (eV)
0.02	60.36	25241	0.060	5.028	25.24	0.399	3.76
0.04	17.48	87215	0.208	4.988	24.83	2.095	3.81
0.06	16.42	90343	0.216	4.538	20.50	2.153	3.89
0.08	7.41	130144	0.311	3.306	10.92	2.300	3.80
0.10	3.34	169944	0.406	2.833	7.860	2.822	3.75

Equations (11) and (12) were used to predict the type and concentration of charge carriers (n_H), as well as the Hall mobility (μ_H) using Hall measurements. The values of the obtained parameters are illustrated in table (4)

$$R_H = -1/n.e \quad (11)$$

$$\mu_H = \sigma|R_H| \quad (12)$$

The table clearly shows a negative Hall coefficient (n-type) for all the samples, showing decreases in Hall voltage as current increases. The mobility is directly inversely proportional to the carrier concentration, and these characteristics are proportional to the MoS_2 concentrations, as can be seen from the table. The substitution doping of MoS_2 produces an extra free carrier during the process, raising the doping level, which leads to more dopant atoms occupying Ti atoms' lattice sites and producing more charge carriers. As the molecular weight of MoS_2 increases, it is anticipated that the density of the carriers will rise as well. In contrast to the Hall

 ISSN (print) 1813-2065, (online) 2309-1673

mobility, it is observed that as MoS_2 concentration increases, μ_H rapidly decreases. The mobility decreases due to the inverse connection between μ_H and n_H; this is a typical behavior exhibited by many polycrystalline films which are caused by the presence of possible barriers in the grain boundaries.

Table (4) Hall Effect observations on $(TiO_2)_{1-x}(MoS_2)_x$ films with different MoS_2 concentrations at room temperature

TiO_2:MoS_2	σ $(\Omega.cm)^{-1}$	ρ $(\Omega.cm)$	R_H $(cm^3.C^{-1})$	n_H x10^{17} (cm^{-3})	μ $(cm^2.V^{-1}.S^{-1})$	Type
1.921:0.079	17.2	0.0580	-38.5	1.62	663	n
1.84:0.16	12.9	0.0773	-30.5	2.05	395	n
1.77:0.23	13.4	0.0748	-66.2	4.43	285	n
1.70:0.30	12.9	0.0776	-93.7	6.66	121	n
1.63:0.37	11.8	0.0846	-58.8	10.6	69.5	n

4. Conclusion

In concluding remarks, nanocomposites were successfully prepared from TiO_2 films doped with MoS_2 by PLD technique. Their structural, morphological, optical and electrical characteristics were determined. These nanocomposite films were hexagonal. The content of 0.02% MoS2 was the optimal to produce the maximum crystalline size and highest roughness. The band gap energy of TiO_2 was varied with varying the content of MoS_2 in the nanocomposite. All samples have negative Hall coefficients (n-type). Therefore, it is concluded that TiO_2 doped with different concentrations of MoS_2 can serve as appropriate materials for solar cell applications.

References

[1] R.C. Weast and S.M. Selby, **"Handbook of Chemistry and Physics"**, 3rd ed., CRC Pub. (1966-1976).
[2] M. Walczak et al., "Structural and morphological characterization of TiO_2 nanostructured films grown by nanosecond pulsed laser deposition", *Appl. Surf. Sci.*, 255(10) (2009) 5267-5270.
[3] N. Okubo et al., "Fabrication of nanoparticles of anatase TiO_2 by oxygen-supplied pulsed-laser deposition", *Appl. Surf. Sci.*, 197 (2002) 679-683.
[4] B.R. Sankapal, M.C. Lux-Steiner and A. Ennaoui, "Synthesis and characterization of anatase-TiO_2 thin films", *Appl. Surf. Sci.*, 239(2) (2005) 165-170.
[5] B. O'Regan and M. Gratzel, "A low-cost, high-efficiency solar cell based on dye-sensitized colloidal TiO_2 films", *Nature*, 353 (1991) 737-740.
[6] S. Ikezawa et al., "Applications of TiO_2 films for environmental purification deposited by controlled electron beam-excited plasma", *Thin Solid Films*, 386(2) (2001) 173-176.
[7] H. Cheng et al., "Hydrothermal preparation of uniform nanosize rutile and anatase particles", *Chem. Mater.*, 7(4) (1995) 663-671.
[8] M. Gopal, W.J. Moberly Chan and L.C. De Jonghe, "Room temperature synthesis of crystalline metal oxides", *J. Mater. Sci.*, 32 (1997) 6001-6008.
[9] E.M. de Paula Silva, "A tecnologia, suas estratégias, suas trajetórias", *Ciência e Cultura*, 60(SPE1) (2008) 13-21.
[10] R.A.H. Hassan and F.T. Ibrahim, "Preparation and Characterization of Ni-doped TiO_2 Nanostructures for Surface Cleaning Applications", *Iraqi J. Appl. Phys.*, 17(1) (2021) 3-8.
[11] R.A.H. Hassan and F.T. Ibrahim, "Preparation and Characterization of Ni-doped TiO_2 Nanostructures for Surface Cleaning Applications", Iraqi J. Appl. Phys., 17(1) (2021) 3-8.
[12] O.A. Hammadi, F.J. Kadhim and E.A. Al-Oubidy, "Photocatalytic Activity of Nitrogen-Doped Titanium Dioxide Nanostructures Synthesized by DC Reactive Magnetron Sputtering Technique", Nonl. Opt. Quantum Opt., 51(1-2) (2019) 67-78.
[13] Z. He and W. Que, "Molybdenum disulfide nanomaterials: Structures, properties, synthesis and recent progress on hydrogen evolution reaction", *Appl. Mater. Today*, 3 (2016) 23-56.
[14] Q.H. Wang et al., "Electronics and optoelectronics of two-dimensional transition metal dichalcogenides", *Nature Nanotech.*, 7(11) (2012) 699-712.
[15] K. Novoselov, "Beyond the wonder material", *Physics World*, 22(08) (2009) 27.
[16] A. El Moutaouakil et al., "Room temperature logic inverter on epitaxial graphene-on-silicon device", *Japanese J. Appl. Phys.*, 50(7R) (2011) 070113.
[17] X. Weng and S. Neethirajan, "Immunosensor based on antibody-functionalized MoS_2 for rapid detection of avian coronavirus on cotton thread", *IEEE Sens. J.*, 18(11) (2018) 4358-4363.
[18] S. Catalán-Gómez et al., "Breast cancer biomarker detection through the photoluminescence of epitaxial monolayer MoS_2 flakes", *Sci. Rep.*, 10(1) (2020) 16039.
[19] Y. Liu et al., "MoS_2 quantum dots featured fluorescent biosensor for multiple detection of cancer", *RSC Adv.*, 7(86) (2017) 54638-54643.
[20] R.M. Kong et al., "A novel aptamer-functionalized MoS_2 nanosheet fluorescent biosensor for sensitive detection of prostate specific antigen", *Anal. Bioanal. Chem.*, 407 (2015) 369-377.
[21] B.D. Cullity, **"Elements of X-ray Diffraction"**, Addison-Wesley Pub. (1956).
[22] G.A. Al-Dahash, Q.M. Salman and M.F. Haddawi, "Study the Effect of Copper (Cu) Doping on the Structure Properties of Zinc Oxide (ZnO) Prepared by Using Pulsed Laser Deposition (PLD)", *J. Kerbala Univ.*, 13(2) (2017) 87-95.
[23] G.K. Williamson and R.E. Smallman, "III. Dislocation densities in some annealed and cold-worked metals from measurements on the X-ray Debye-Scherrer spectrum", *Phil. Mag.*, 1(1) (1956) 34-46.

[24] G.H. Mohammed, "The Effect of Au Nanoparticles on the Structural and Optical Properties of (NiO:WO_3) Thin Films Prepared by PLD Technique", *Iraqi J. Sci.*, 63(6) (2022) 2502-2513.
[25] H. Kim et al., "Transparent conducting aluminum-doped zinc oxide thin films for organic light-emitting devices", *Appl. Phys. Lett.*, 76(3) (2000) 259-261.
[26] S.S. Chiad et al., "Fabrication and study the structure, optical and dispersion parameters of PMMA with $InCl_3$ additive", *J. Glob. Pharma. Technol.*, 11(4) (2019) 369-375.
[27] M.G. Hutchins et al., "Structural and optical characterization of thermally evaporated tungsten trioxide (WO_3) thin films", *Mater. Chem. Phys.*, 98(2-3) (2006) 401-405.
[28] F.J. Kadhim, O.A. Hammadi and N.H. Mutesher, "Photocatalytic activity of TiO_2/SiO_2 nanocomposites synthesized by reactive magnetron sputtering technique", *J. Nanophot.*, 16(2) (2022) 026005.
[29] S.J. Mousavi, "First–Principle Calculation of the Electronic and Optical Properties of Nanolayered ZnO Polymorphs by PBE and mBJ Density Functionals", *J. Optoelectron. Nanostruct.*, 2(4) (2017) 1-18.
[30] R.H. Turki and M.A. Hameed, "Spectral and Electrical Characteristics of Nanostructured NiO/TiO_2 Heterojunction Fabricated by DC Reactive Magnetron Sputtering", *Iraqi J. Appl. Phys.*, 16(3) (2020) 39-42.
[31] S. Sönmezoğlu et al., "The effects of film thickness on the optical properties of TiO_2–SnO_2 compound thin films", *Physica Scripta*, 84(6) (2011) 065602.
[32] A. Gültekin, "Effect of Au nanoparticles doping on the properties of TiO_2 thin films", *Mater. Sci.*, 20(1) (2014) 10-14.
[33] S.R. Elliott, **"Physics of Amorphous Materials"**, Longman Group (Essex, 1983).

Table (1) Diffraction peaks, inter-planar distance, and full-width at half maximum (FWHM) of $(TiO_2)_{1-x}(MoS_2)_x$ thin films prepared at room temperature with different MoS_2 concentrations

Sample	2θ (deg.)	FWHM (deg.)	d_{hkl} (Å)	d_{hkl} Std. (Å)	C.S. (nm)	hkl	Phase	$\delta \times 10^{15}$ (line/m^2)	ε
X=0.02	27.3427	0.2914	3.2591	3.2483	28.1	(110)	RutileTiO_2	1.27	0.00124
X=0.04	27.3427	0.4953	3.2591	3.2483	16.5	(110)	RutileTiO_2	3.67	0.00210
X=0.06	27.1387	0.7575	3.2832	3.2483	10.8	(110)	RutileTiO_2	8.58	0.00321
	28.1294	0.4079	3.1697	3.1325	20.1	(004)	Hex. MoS_2	2.48	0.00173
X=0.08	27.4592	0.6410	3.2456	3.2483	12.8	(110)	RutileTiO_2	6.14	0.00272
	28.4499	0.3205	3.1347	3.1325	25.6	(004)	Hex. MoS_2	1.53	0.00136
	32.9371	0.3205	2.7172	2.7193	25.9	(100)	Hex. MoS_2	1.50	0.00134
	33.6072	0.5245	2.6646	2.6575	15.8	(101)	Hex. MoS_2	3.99	0.00219
	39.4347	0.8741	2.2832	2.2789	9.7	(103)	Hex. MoS_2	10.72	0.00359
	49.2541	0.8158	1.8485	1.8428	10.7	(105)	Hex. MoS_2	8.71	0.00324
X=0.1	27.5175	0.6118	3.2388	3.2483	13.4	(110)	RutileTiO_2	5.59	0.00259
	28.3042	0.2914	3.1506	3.1325	28.1	(004)	Hex. MoS_2	1.26	0.00123
	32.9371	0.3205	2.7172	2.7193	25.9	(100)	Hex. MoS_2	1.50	0.00134
	33.6655	0.4954	2.6601	2.6575	16.8	(101)	Hex. MoS_2	3.56	0.00207
	39.3473	0.7867	2.2880	2.2789	10.7	(103)	Hex. MoS_2	8.69	0.00323
	49.3124	0.6993	1.8465	1.8428	12.5	(105)	Hex. MoS_2	6.39	0.00277

 ISSN (print) 1813-2065, (online) 2309-1673

IRAQI JOURNAL OF APPLIED PHYSICS
Vol. 19, No. 3A, July-August 2023, pp. 31-36

Chaotic Semiconductor Laser with Extra Optical Delay Feedback

Raghad I. Ibrahim
Wasmaa A. Jabbar

Department of Physics, College of Education, Mustansiriyah University, Baghdad, IRAQ

In this study, a new method of double delayed feedback chaotic system has been suggested. The optisystem program uses semiconductor lasers for generating chaos. To determine the effect of chaos created by semiconductor lasers, many parameters are taken into account and simulated. Experimental data have shown that using a Mach-Zehnder modulator (MZM), semiconductor lasers (SL) with double feed-back exhibit spikes over generations. Chaotic laser output is fed back to MZM, based on the chaotic optoelectronic and optical oscillator system to create the original system.

Keywords: Chaos generation; Optoelectronics; Optical feedback; Mach-Zehnder Modulator
Received: 08 April 2023; **Revised:** 01 May 2023; **Accepted:** 08 May 2023

1. Introduction

A term chaos represents a paradigmatic name which has been utilized for describing deterministic dynamic systems that have a complex behavior, which is unpredictable and has extreme sensitivity to the initial conditions. The sensitive dependence upon the initial conditions indicates the fact that in the case where two chaotic temporal sequences begin from very close however, a little different initial condition, then the behavior of those two sequences is similar at first, none-the-less, begin exponentially diverging in the time and never exhibit identical behaviors again [1-3]. The irregular spiking sequences in the chemical, electronic and biological systems were observed often to result from the dynamics of the multiple time scales. Chaotic spiking regime may be comprehended according to the chaotic attractor's excitability, in which small chaotic background is spontaneously triggering the excitable spikes in erratic, however, deterministic sequence [4]. In a case where a semiconductor laser (SL) has been subjected to one perturbation or more like the optical injection (OI), optical feedback (OFB), optoelectronic feedback (OEFB) and optical modulations, it may show rich non-linear dynamics that include chaos [5]. A Mach-Zehnder interferometer (MZI) represents non-linearity source, whereas SL providing optical power plays the role of a linear current-to-optical converter of frequency. The interferometer's nonlinearity that is coupled with the feedback loop delay combine for producing a steady state, periodic, and chaotic behavior range [6,7]. Nonlinear reduction of the gain for semiconductor laser that is utilized in the systems of the optical communication is quite strong and its direct consequences on dynamics of those lasers results in suppressing the chaotic output. One of the most important roles in the modeling of the dynamics of the semiconductor lasers is the fact that dynamic semi-conductor laser response is highly dependent upon non-linear gain [8].

In recent years, the rapid development of related technologies at home and abroad, at present there are four international produce optical chaos and three modulation signal. Design an optical chaos secret system key is generated chaos method, and the selection of the synchronous mode based on the optical communication simulation software optisystem [9]. OptiSystem can be defined as a software package for optical communication devices that enables users to simulate, design, and test optical links at the transmission layer of advanced optical networks [10]. A radio over fiber (RoF) communication system has been designed in a licensed Optisystem software version 17 where the signal of the radiofrequency is modulated on the optical signal through the use of the laser and MZM [11]. Propagation of chaos hiding multiformat message has been researched for the model of the long distance communications. Synchronization between receiver and transmitter is accomplished for obtaining acceptable eye-diagrams and quality factors based upon the optisystem [12]. An SL diode is driven to chaotic area with the use of the scheme of the direct modulation and RoF signal is added by the chaos message masking approach [13]. Following introducing extra optical feedback loop, the time-delay signature characteristics regarding chaotic signal output from the optoelectronic oscillator (OEO) have been numerically examined [14].

The optisystem program is used in this study to create chaos in semiconductor laser with the double delayed feedback. High bandwidth chaos is generated by semiconductor lasers in simulations. To identify a route from periodic to quasi-periodic and then to chaos behavior, many semiconductor laser parameters including modulation peak current, bias current, and frequency have been optimized. Chaotic pulses of acceptable amplitude are produced so that to use them for long distance communication and to hide message modulated with advance formats.

2. System's Model and Theory

A chaotic signal generation diagram depending on OEO after the addition of extra optic feedback is

shown in Fig. (1). MZM, SL, photodetector (PD), and amplifier make up the device. Using a laser diode, a chaotic dynamics laser was created and delivered to a MZM with a frequency (F) half-wave voltage of VF. The MZM could be specified as a tool used to measure relative phase shifting between two collimated beams of light coming from a specific source, either by altering length of one arm or by inserting a sample into the path of one of the beams. MZM has 2 ports for the input and the output, two couplers are used for constructing a fundamental MZM; one is placed at the input and functions as a splitter, and the other is placed at the output and functions as a combiner. One of the two parts of MZM's output passes through delay line 1 and is transformed into an electrical signal by a photo-detector (PD). The FA amplifies electrical signals further, and an amplifier functions as a band-pass filter with a low cut-off frequency of Fl and a high cut-off frequency of f_H. Once optoelectronic feedback was established in loop1 with a delay time equal to T_1, the electrical signal which was amplified V(t), which was reliant upon PD conversion efficiency and FA magnification, is delivered to MZM. The other part is injected into the delay line 2–based optical feedback loop, and the feedback delay time is T_2. In order to maximize coupling efficiency, the strength regarding the optical feedback K is controlled using a variable amplifier in conjunction with a MZM.

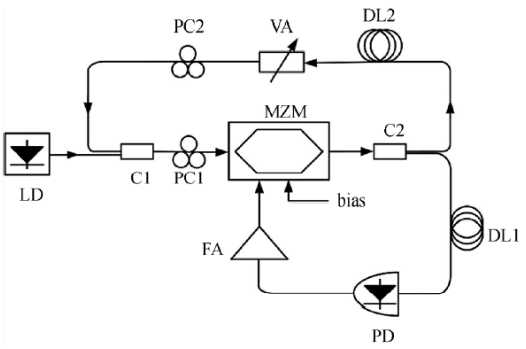

Fig. (1) Diagram of chaos signal generation that is based upon OEO after the introduction of extra optical feedback. FC: fiber coupler; LD: laser diode; MZM: Mach- Zehnder modulator; PC: polarization controller; PD: photo-detector; DL: fiber delay line; VA: variable attenuator; FA: frequency amplifier

According to Ikeda rate equations [15] and taking extra optic feedback under consideration, for the convenient comparison to results that have been obtained by [16], dynamic chaotic system equations that have been mentioned earlier may be explained in [16]

$$\frac{dx(t)}{dt} = -\frac{1}{t_H}\left\{x(t) + \frac{1}{t_L}y(t) - P_{in}(t - T_1) \times Q \times \cos^2[x(t - T_1) + \phi]\right\} \quad (1)$$

$$P_{in}(t) = P_0 + K \times P_{in}(t - T_2) \times \cos^2[x(t - T_2) + \phi] \quad (2)$$

$$\frac{dy(t)}{dt} = x(t) \quad (3)$$

Here,

$x(t) = \pi V(t)/(2V\pi F)$,

$t_H = 1/(2\pi f_H)$,

$t_L = 1/(2\pi f_L)$, and

$Q = \pi gAG/(2V\pi F)$

A represents the total optoelectronic feedback loop attenuation, g and G represent PD conversion efficiency and FA gain, respectively). P_o represents power of the laser output, and $P_{in}(t)$ represents the coupled MZM input power. P_oQ denotes non-linear function strength, playing a significant role in chaotic behaviors with a high level of the complexity.

2.1 Implementation of Optisystem Simulation

OptiSystem software was used for simulating the circuit and design. The simulated circuit diagram for the suggested method is shown in Fig. (2), in which the built-in components were used according to the right requirements.

Research was done on the chaotic behavior of the OEFB when MZM bias voltage is present. Figure (2) depicts the experimental setup for analyzing the chaotic behavior regarding MZMs using optical and optoelectronic delayed feedback. The input couple divides the light into the two interferometer arms. The coupler divides the light into two equal beams, one of which, the SL (1550nm) beam, was coupled into MZM and after that into the PD in order to convert the optical signal into electrical one. PD is after that coupled to amplifier and feedback arm. It is amplified through optical amplifier, and after that, it enters the MZM once more to produce chaotic lasers through non-linear modulation. The coefficient of the gain regarding the original electro-optical oscillator (OEO) is altered dynamically, and a further time delay is added to system, resulting in a more complex chaotic laser signal, when system output is fed back to MZM through delayed optical path.

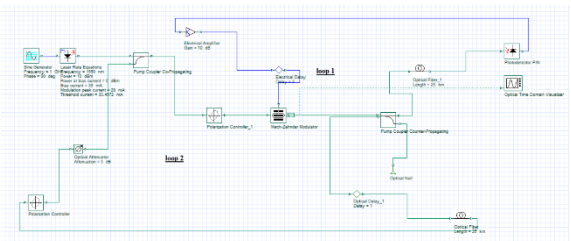

Fig. (2) Diagram of OEO chaotic system with the double feedback

Aforementioned properties make it easier to create a chaotic secure communication system that offers enhanced security. Also, the optical paths of two arms are not equal in length due to the addition of a light path feedback delay, which causes the phase shifting, which is corresponding to delay to be the input signal's wavelength function. The parameter interval which couldn't cause chaos experiences chaos as well, path into the chaos is increased, and the system becomes more workable.

 ISSN (print) 1813-2065, (online) 2309-1673

2.1.1 Changing of the Bias Current (i.e. the Route from the Periodic to the Quasi-Periodic and Chaos)

Table (1) lists the semiconductor laser parameters that can cause chaos. Chaos in a laser is the signal's variation in frequency and amplitude. Gradually increasing the bias current from 35 to 41 mA, the quasi-periodic behavior begins to appear. The semiconductor laser bias current changing causes the variation of nonlinear dynamics of the system. The time series undergoes a transition from a line (at 40mA bias current) to semi sinusoidal oscillations. These semi-sinusoidal oscillations increase in amplitude gradually until they reach to another types of periodicity and finally to chaotic spiking oscillations . Thus, This scenario is called the period-doubling route to chaos .Three cases of current's values are chose to demonstrate the behavior of the system as shown in Fig. (3).

Table (1) Parameters of the SL with various values of the bias current

Parameters	Values	Unit
Bias current	35-41	mA
Power	10	dBm
Wavelength	1550	nm
Modulation peak current	40	mA
Power (at bias current)	0	dBm
Threshold power	0.0154	mW
Threshold current	33.46	mA
Frequency	2	GHz

Figure (3a) represents periodic behavior at the start when the bias current is 40 mA. While the bias current is 39 mA as shown in Fig. (3b), chaotic pulses exhibit quasi-periodic behavior. Each bunch has a span that roughly equals 1ns and then a new set of the chaotic pulses begins one ns later. The frequency of Bunches increased as the bias current increased, and as they overlapped, they created a chaotic route as shown in Fig. (3c). This mean Fig. (3) shows the path from periodic to quasi-periodic and after that chaos from bias current 41 mA to 35 mA.

The scenario that results in chaos is summarized by the bifurcation diagram, as shown in Fig. (4). The bifurcation diagram illustrates how the intensity relates to the laser output (i.e., peak-to-peak) when a control parameter is changed (bias current of laser source). The bifurcation diagram was produced within the confines of a constant increase in the control parameter (bias current) of 0.25 mA.

The region between 35-41 mA was described in the bifurcation diagram. The dynamic changed to quasi-chaotic behavior first appears at 39.75-36.75 mA in the first region, which exhibits periodic behavior from 41-40 mA. As the bias current is gradually reduced, chaotic behavior starts to show between 37 and 35 mA. This indicates that the dynamic system of SL changed from periodic to chaotic and quasi-chaotic behavior as a result of the variation in bias current.

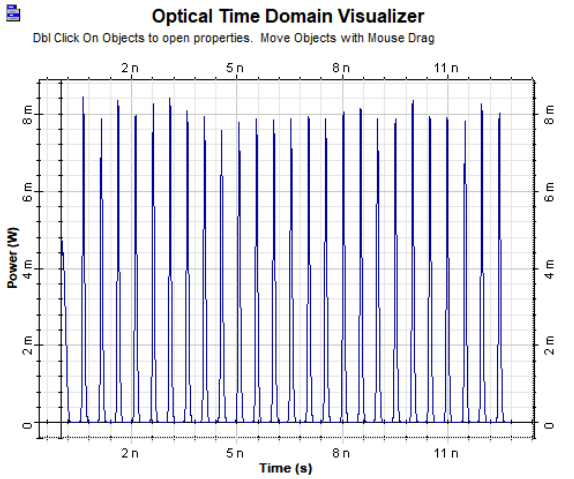

(a) Bias current is 40mA

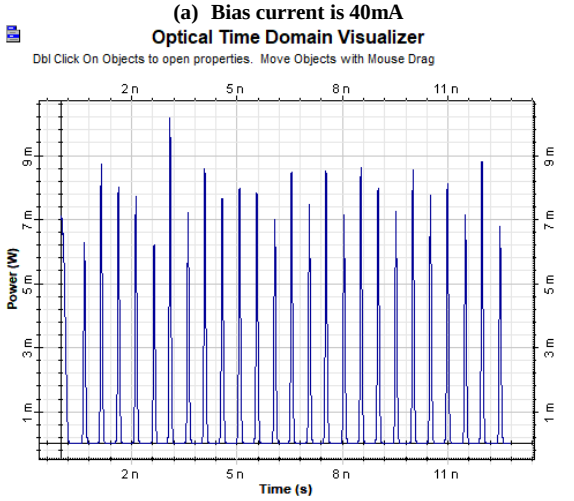

(b) Bias current is 39mA

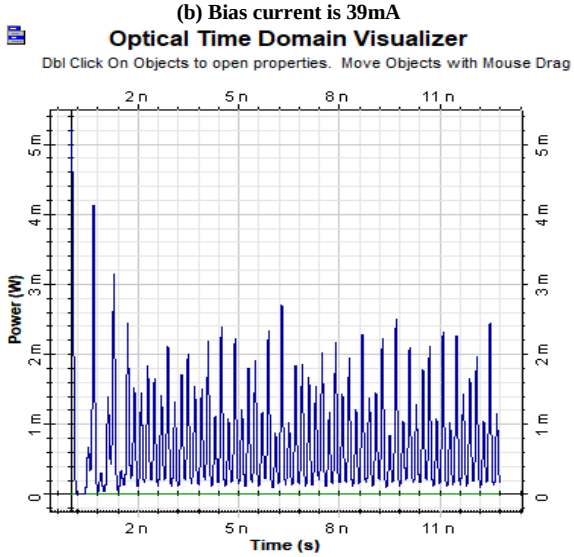

(c) Bias current is 36mA

Fig. (3) The output of SL at different values of bias current

2.1.2 Changing the Modulation Peak Current (i.e., the High Amplitude Pulses)

The parameters for generating chaos using semiconductor lasers with different modulation peak currents are shown in table (2). Modulation peak current is increased from 40 to 60 mA while maintaining the same bias current. Low modulation peak current results in extremely small pulse

amplitudes that not just stray from the chaotic behaviors but are useless as well for any useful length of the fiber. Figure (5) represents the best case of the system's behavior which shows a noticeable change in pulse amplitude with an increase in the value regarding modulation peak current, where various pulses of low-amplitude are followed by pulses of high-amplitude.

Table (2) Parameters of SL with different values of the modulation peak current

Parameters	Values	Units
Bias current	50	mA
Power	10	dBm
Wavelength	1550	nm
Modulation peak current	40-60	mA
Power (at bias current)	0	dBm
Threshold power	0.123	mW
Threshold current	33.46	mA
Frequency	5	GHz

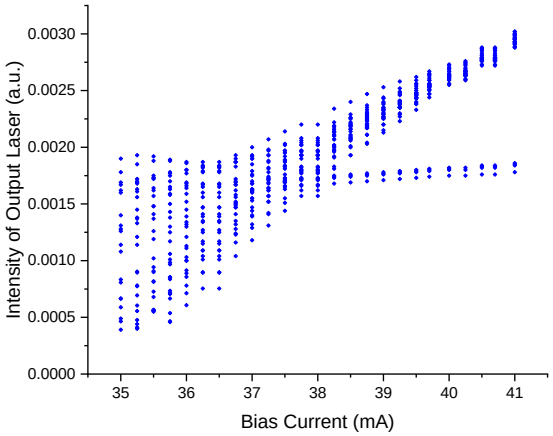

Fig. (4) Bifurcation diagram for bias current variation

The series appears to be periodic as shown in Fig. (5a). Additional increasing in the Modulation peak current lead to quasi- periodic as shown in Fig. (5b). Figure (5c) shows the chaotic spiking oscillation beginning of the behavior of non-regular periodicity (i.e., appearing of different amplitudes). Pairs of small-amplitude oscillations alternate with pairs of large amplitude oscillations. The result is an example of a mixed mode oscillation which is oscillation that consist of a mixture of different kinds of oscillation, usually small and large amplitude relaxation spikes, with the intermediate amplitudes left unrealized.

The bifurcation diagram was utilized to examine chaotic routes and output evolutions in nonlinear systems due to the changes in the control parameter. A bifurcation diagram for varied modulation peak currents is shown in Fig. (6).

Figure (6) exhibits such modulation peak current values resulted in the system to be changed from the periodic at 40-41 mA, and after that into quasi-chaotic behavior at 42-47 mA and finally into chaotic at 48-60 mA.

Findings indicate that modulation peak current may be a parameter that regulates system's overall dynamics and that varying amplitudes are employed in order to govern chaotic system's transition from the periodic to the quasi-periodic, and then into chaotic behavior.

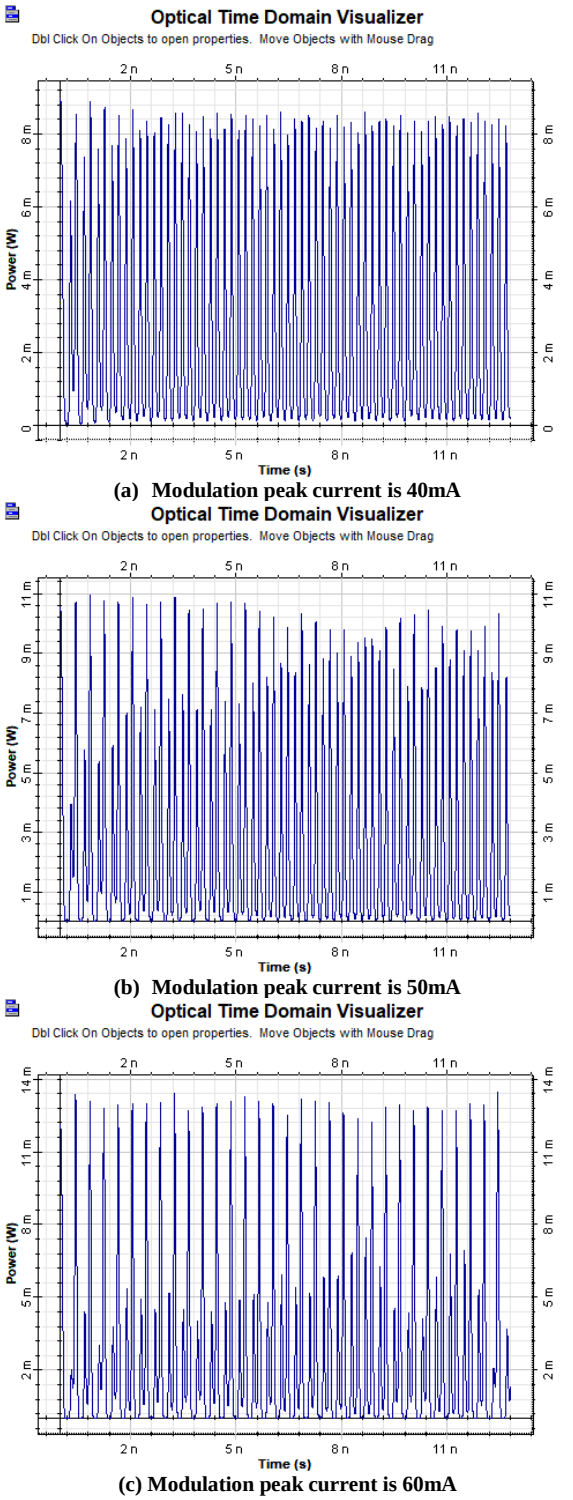

(a) Modulation peak current is 40mA

(b) Modulation peak current is 50mA

(c) Modulation peak current is 60mA

Fig. (5) Output of the SL at different values of the modulation peak current

 ISSN (print) 1813-2065, (online) 2309-1673

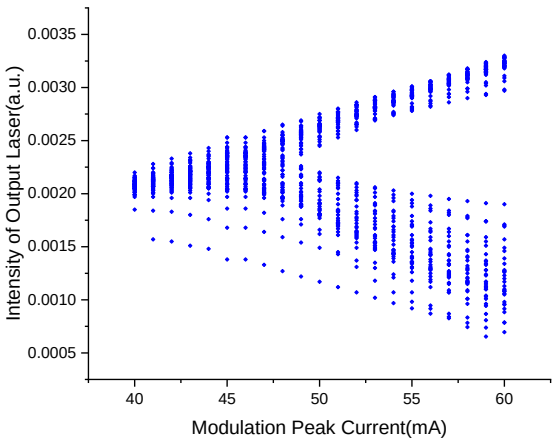

Fig. (6) Bifurcation diagram with different values of the modulation peak current

2.1.3 Changing the Current Source Frequency (i.e., Random Amplitude Pulses)

The chaotic nature regarding the pulses must be achieved with an adequate pumping power or current. Pulses of the same amplitude are seen in the case when the current source's frequency is low and the electric field strength is not particularly high. Because of an increase in field strength, increasing the frequency causes variations in pulse amplitude. Table (3) displays the frequency generator's properties when used for external modulation at various frequencies between 1 and 5 GHz.

Table (3) Parameters of the current source with different frequency values

Parameters	Values	Units
Phase	90	Deg
Amplitude	1	a.u.
Frequency	1- 5	GHz
Bias	0	a.u.

Figure (7) represents the most common variation in the semiconductor laser outputs with respect to the changes of frequency. At the beginning, the first figure (7a) is indicated to a stable equilibrium, therefore the dynamics of SL is in the form of periodic motion, any more increasing in frequency at 3GHz (in Fig. 7b), will demonstrates the quasi-periodic behavior begins to appear. Gradually increasing the frequency (5 GHz) as shown in Fig. (7c), the chaotic behavior begins to appear.

Figure (8) illustrates how a function generator was used to modulate the source's frequency. Results imply that the frequency modulation could be a control parameter with regard to system's collective dynamics. Many frequencies have been used in order to govern the chaotic system, from periodic state at 1-1.25 GHz to quasi chaotic state at 1.5-1.75 GHz to chaotic state at 2-5 GHz. Therefore, in the case when frequency is added to chaotic systems, quite intriguing results are discovered.

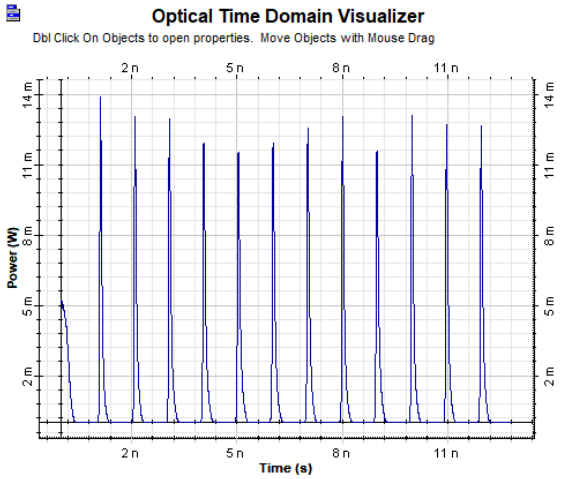

(a) Frequency of a current source is 1GHz

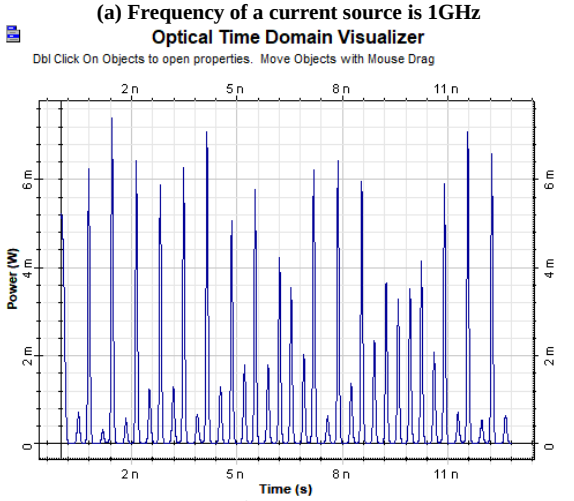

(b) Frequency of a current source is 3GHz

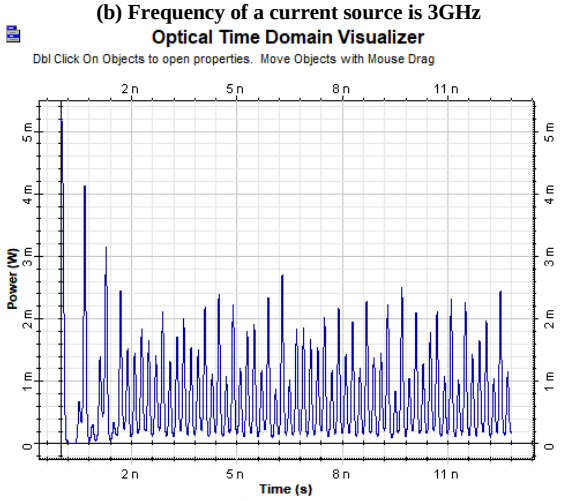

(c) Frequency of a current source is 5GHz

Fig. (7) Output of the SL at different values of frequency of a current source

Finally the appropriate control in bias current, modulation peak current and frequency of SL can be generate chaotic laser which is utilized for communication purposes (i.e. by modulating the chaotic waveform with the signal to be send, in order to protect the signal from the spy), and this variation in the control parameters could give us an impression or an idea about the method of elimination of the chaotic behavior when it is considered as an

undesired phenomenon in several engineering applications because it restricts the operating range of many electronic and mechanical devices, etc.

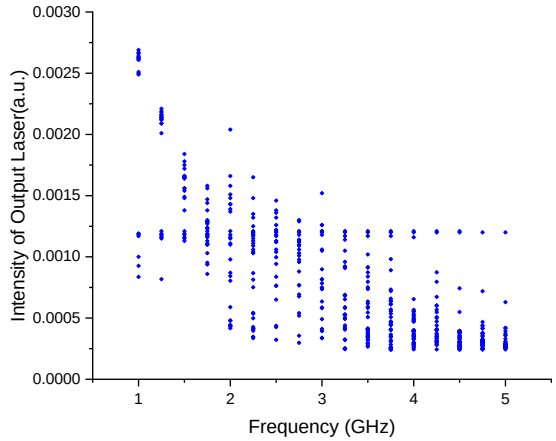

Fig. (8) Bifurcation diagram with different modulations of the frequency

3. Conclusion

The improvement of double delayed feedback oscillator's security circuit is successfully built in optisystem program for the secure communications, which resulted in greatly improving the original optoelectronic delayed feedback oscillator's security, and is simpler to implement compared to the majority of the other suggested optoelectronic delayed feedback systems. The bias current, modulation peak current & frequency of SL act good control parameters ingenerating chaotic semiconductor laser. As a best result, the value of bias current varied between 37 and 35 mA, the modulation peak current at 48-60 mA and frequency at 2-5 GHz. The system might attain increased chaotic complexity, which partially hides the massage's signals and increases the system's practicability. These properties are helpful for promoting the level of the security and further maturity of the optical chaos secure communications.

References

[1] P. Holmes, "Chaos" (Hao Bai-Lin), *SIAM Rev.*, 28(1) (1986) 106-109.
[2] R.C. Hilborn, **"Chaos and Nonlinear Dynamics: An Introduction for Scientists and Engineers"**, Oxford University Press (NY, 2000) 100-115.
[3] A. Uchida, **"Optical Communication with Chaotic Lasers: Applications of Nonlinear Dynamics and Synchronization"**, John Wiley & Sons (Weinheim, 2012) 19-57.
[4] K. Al-Naimee et al., "Excitability of periodic and chaotic attractors in semiconductor lasers with optoelectronic feedback", *The Euro. Phys. J. D*, 58(2) (2010) 187-189.
[5] A.E. Korsuize and A.E. Korsuize, **"Coupled Systems of Differential Equations and Chaos"**, Springer-Verlag (Netherlands) (2008) 25-27.
[6] G.F. Jiao et al., "Nonlinear phase estimation enhanced by an actively correlated Mach-Zehnder interferometer", *Phys. Rev. A*, 102(3) (2020) 033520.
[7] N. McBride, "Chaos theory as a model for interpreting information systems in organizations", *Inform. Sys. J.*, 15(3) (2005) 233-254.
[8] R.S. Tucker, "High speed modulation properties of semiconductor laser", *IEEE Trans. Electron Dev.*, 3(12) (1985) 1180-1192.
[9] Z.Z. Zuo, "A Research on Optical Chaotic Secure Communication System Based on Optisystem", MSc thesis, Huazhong University of Science and Technology (China) (2011) 20-40.
[10] OptiSystem software for the design of optical communication system, https://optiwave.com.
[11] A. Ali et al., "Design and analysis of secure RoF based communication in 5G fronthaul", 2020 Int. Conf. on Cyber Warfare Secur. (ICCWS), IEEE (2020) 1-6.
[12] F. Qamar et al., "Secure duobinary signal transmission in optical communication networks for high performance & reliability", *IEEE Access*, 5 (2017) 17795-17802.
[13] D.A. Mazhar et al., "Design issues of digital and analog chaotic RoF link using chaos message masking", *IEEE Access*, 7 (2019) 174042-174050.
[14] X. Liu et al., "Time-delay signature characteristics of the chaotic output from an optoelectronic oscillator by introducing an optical feedback", *Front. Optoelectron.*, 13(4) (2020) 402-408.
[15] K. Ikeda and K. Matsumoto, "High-dimensional chaotic behavior in systems with time-delayed feedback", *Physica D: Nonl. Phenom.*, 29(1-2) (1987) 223-235.
[16] H. Hu, S. Shi and F. Xie, "Electro-optic intensity chaotic system with an extra optical feedback", *Opt. Commun.*, 402 (2017) 140-146.

 ISSN (print) 1813-2065, (online) 2309-1673

IRAQI JOURNAL OF APPLIED PHYSICS
Vol. 19, No. 3A, July-August 2023, pp. 37-42

Preparation and Characterization of Copper Oxide Nanoparticles by Precipitation Method for Photonics and Optoelectronics

Zaman S. Jabar
Majid H. Hassouni

Department of Physics, College of Education, Mustansiriyah University, Baghdad, IRAQ

In this study, copper oxide (CuO) nanoparticles have been synthesized by the precipitation method. The structural and spectroscopic characteristics of these nanoparticles were characterized. These nanoparticles showed energy band gap of 5.1 eV. Also, they were employed to fabricate photodetectors on silicon substrates (Ag/CuO/PSi/(n,p)Si/Ag) with two different type of conductivity (n- and p-type) and the parameters of these structures such as spectral responsivity and specific detectivity were investigated in the wavelength range of 400–900nm.

Keywords: Copper oxide; Precipitation method; Optical properties; Photodetectors
Received: 28 March 2023; **Revised:** 11 May 2023; **Accepted:** 18 May 2023

1. Introduction

Due to its exceptional optical, electrical, physical, and magnetic characteristics, copper oxide (CuO) is one of the most p-type semiconductors that is receiving a lot of interest [1]. Numerous applications, including catalysis, make substantial use of CuO, which has a low band gap of 1.2 eV [2] converted from solar energy [3] gas detector [4] likewise field emission [5]. The fabrication of CuO nanostructures, which have demonstrated exceptional performance when compared to their bulk equivalent, can, nevertheless, improve these unique features [6]. CuO is produced into a variety of nanostructures, including nanowires, nanorods, nanoneedles, nanoflower, and nanoparticles. Several techniques, including thermal oxidation, have been suggested in recent years to prepare CuO nanoparticles of varied sizes and forms such as sonochemical [7,8], combustion [9], chemical vapor deposition (CVD) [10], reactive sputtering [11,12], and swift precipitation [13,14]. Precipitation is a simple process that takes a lot of attention due to its low energy and temperature requirements, cost-effective for mass production, and high yield.

The current work concerns to prepare copper oxide (CuO) nanoparticles by precipitation method and characterize their structural and spectroscopic characteristics. These nanoparticles are employed in the fabrication and characterization of heterojunction photodetectors for photonics and optoelectronics applications.

2. Experimental Work

Copper nitrate ($Cu(NO_3)_2.3H_2O$) was the major chemical material used as a precursor to prepare the copper oxide nanoparticles via precipitation method. The precursor was first dissolved to a concentration of 1.87 g/mol in 100 ml of distilled water. Then, 9 cc of a 1M NaOH solution was added gradually while being vigorously stirred until the pH reached 14. Precipitations with black color were found.

The structural characteristics of the prepared nanoparticles were introduced by the x-ray diffraction (XRD) and atomic force microscopy (AFM), while their spectroscopic characteristics were introduced by Fourier-transform infrared (FTIR) and UV-visible spectroscopy. As well, the parameters of the photodetectors fabricated from these nanoparticles on silicon substrates were determined and compared as two different types of conductivity of these substrates (n- and p-type) were used.

The copper oxide films were deposited on glass substrates and silicon wafers by casting method. The substrates were cleaned using distilled water and ethanol by ultrasonic for 15 min. Thereby, porous silicon surfaces were prepared using hydrofluoric acid (HF) with a concentration of 40% M. The etching process was performed throughout subjecting the acid to current (15-20mA). The thickness of obtained films was 1 µm. The experimental setup of this work is shown in Fig. (1).

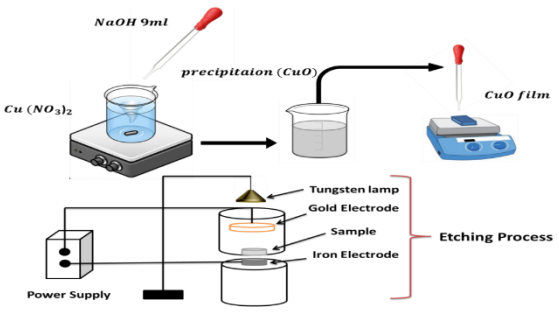

Fig. (1) Experimental setup of precipitation method to prepare CuO nanoparticles

3. Result and Discussion

Figure (2) displays the absorption spectrum of the CuO NPs in the spectral range 200-1000 nm. It is clear that the absorbance start to decrease at wavelength of 212nm to reach its minimum at 264nm then increases to a peak centered on 346nm. Then, it decreases again within the visible region and beyond. This reveals that the samples transmit the visible light and infrared radiation without reasonable absorption or scattering effects.

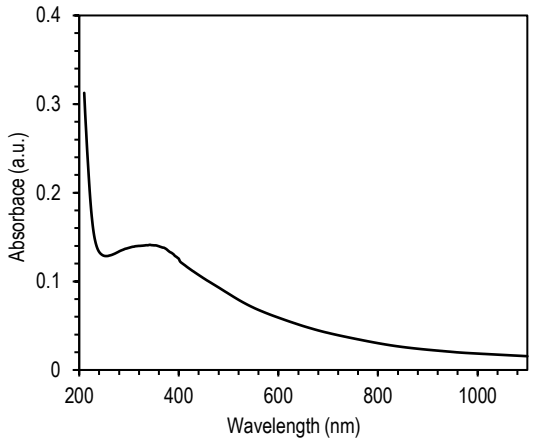

Fig. (2) Absorption spectrum of the CuO NPs prepared in this work

The formula shown below [15] may be used to calculate the optical band gap of CuO NPs prepared in this work from their UV-Vis spectra:

$$(\alpha h\nu)^{1/d} = A(h\nu - E_g) \quad (1)$$

where α is the absorption coefficient, E_g is the optical band gap, $h\nu$ is the incident photon energy

Figure (3) shows the determination of energy band gap of 5.1 eV, which is larger than the reported value [16] as well as of the bulk CuO (2.1eV). The size of the prepared nanoparticles is responsible for the larger band gap as the quantum confinement effect takes place. Accordingly, the band gap energy starts to rise as particle size decreases and the size of nanocrystals is less than the Bohr radius of the excited electron-hole pair [12]. This result agrees with previous study [17].

Based on the result of UV-visible spectrophotometry shown in Fig. (4), the optical constants, mainly absorption (extinction) index, refractive index, and complex dielectric constant were presented. The following relationships [18] were used to study the relationship between the extinction coefficient (k) and the refractive index (n) as functions of photon energy:

$$k = \frac{\alpha\lambda}{4\pi} \quad (2a)$$

$$n = \left[\frac{4R}{(R-1)^2} - k^2\right]^{1/2} - \frac{R+1}{R-1} \quad (2b)$$

whereas the complex dielectric constant (ε) was identified as follows:

$$\varepsilon = \varepsilon_1 - i\varepsilon_2 \quad (3)$$

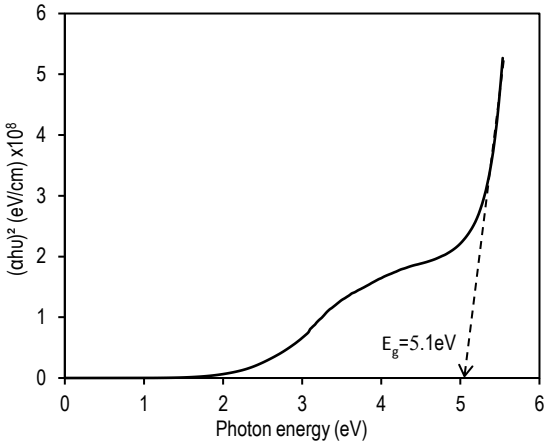

Fig. (3) Determination of optical energy band gap the CuO NPs prepared in this work

The real part (ε_1) and the imaginary part (ε_2) of the dielectric constant can be obtained using the following formulas [18]:

$$\varepsilon_1 = n^2 - k^2 \quad (4a)$$

$$\varepsilon_2 = 2nk \quad (4b)$$

From the data of refractive indices, there are two ways to calculate the high-frequency dielectric constant. The free carriers and lattice vibration modes of the dispersion are discussed in the first technique. The second approach relies on the scattering caused by bound carriers in an empty lattice. The high-frequency dielectric constant of the lattice was calculated using both techniques.

Figure (5) depicts the XRD pattern of the CuO NPs prepared in this work. The position peaks, which correspond to the (111), (110), (220), and (002), could hardly be seen at the 2θ values of 17.57°, 29.39°, 31.73°, and 35.57°, respectively. The following equations were used to determine the average crystallite size (D), dislocation density (δ), and micro-strain (ε) for the prepared samples [19]:

$$D = \frac{0.9\lambda}{\beta cos\theta} \quad (5a)$$

$$\delta = \frac{1}{D^2} \quad (5b)$$

$$\varepsilon = \frac{\beta}{4tan\theta} \quad (5c)$$

The peaks are located and compared to the published JCPDS data. The prepared nanoparticles have crystallite size ranging between 33.997 and 58.897 nm. The XRD pattern reveals the formation of monoclinic CuO with an average crystallite size of 51.21nm. However, this pattern shows that $Cu(OH)_2$ nanostructures are immediately developed by position peaks at 10.46° and 26.48° [20] when adding copper nitrate solution to the NaOH solution.

 ISSN (print) 1813-2065, (online) 2309-1673

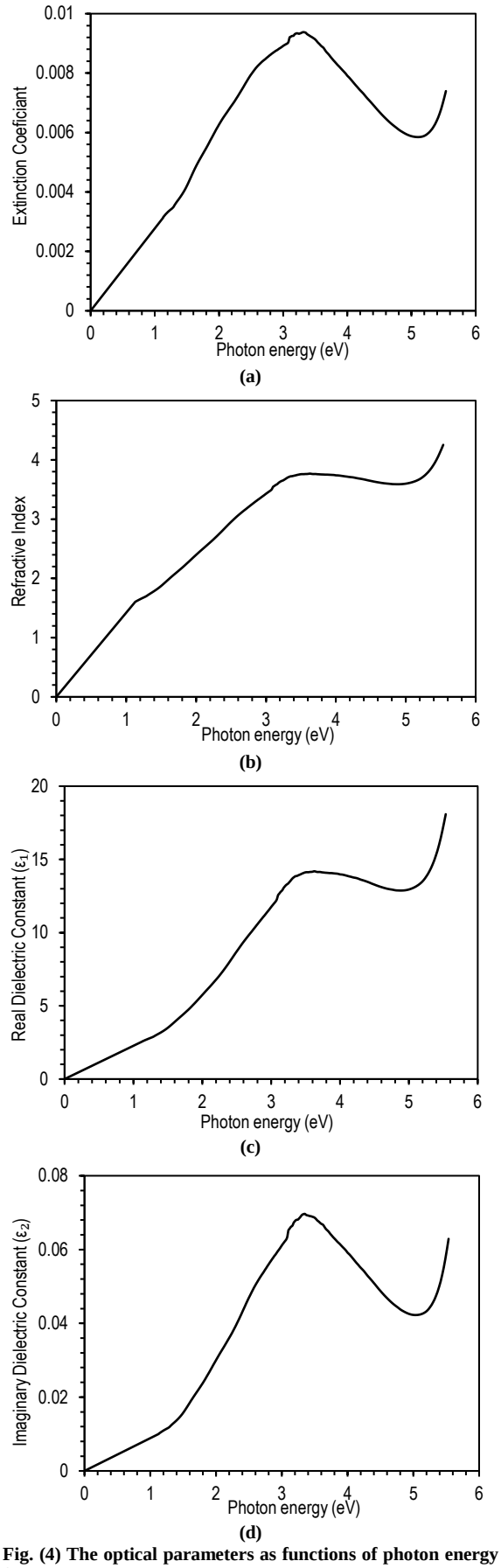

Fig. (4) The optical parameters as functions of photon energy for CuO NPs prepared in this work

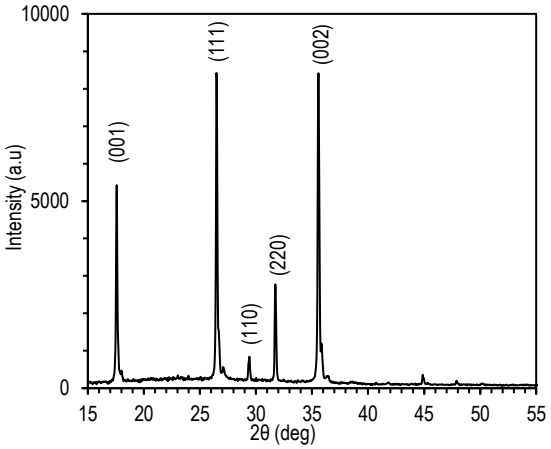

Fig. (5) XRD pattern of the CuO NPs prepared in this work

Figure (6) shows the FTIR spectrum of the CuO NPs prepared in this work. The peak at 741 cm^{-1}, ascribed to the Cu-O wagging, indicates that the material contains a metal-oxide group. The presence of the hydroxide group in the sample is confirmed by the vibration peak at 3493.5 cm^{-1}. This could be attributed to the water which is a chemical byproduct that is bound to the CuO nanoparticle surface and that can be evaporated with more heating. CuO is formed from copper nitrate at 1655.5 cm^{-1} (M-O rocking out of plane).

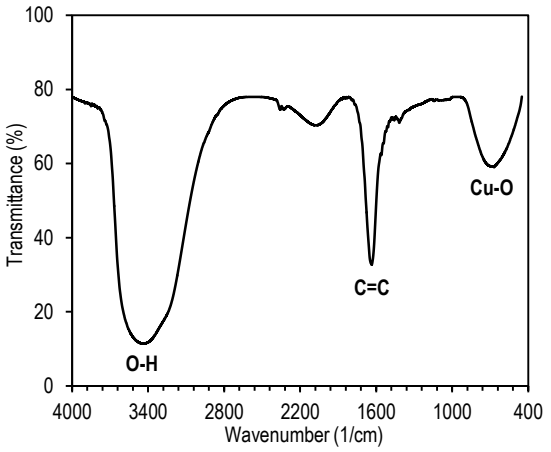

Fig. (6) FTIR spectrum of the CuO NPs prepared in this work

Figure (7) displays the three-dimensional AFM surface images of CuO film samples. Many crucial issues, such as fraction, contact deformation, tightness, etc., may be effectively addressed by the assessment of surface roughness characteristics [21,22]. The CuO film demonstrates the development of aggregated nanosized grains spanning the whole substrate surface. The average size of the regularly formed agglomerated grains is 7.22 nm. Such morphology is the product of synthesis at ambient temperature. These films slowly develop into nanograins as a result of room-temperature production. Additionally, the produced grains have a regular shape and a root-mean-square (r.m.s.) of 1.86 nm, which indicates minimal roughness.

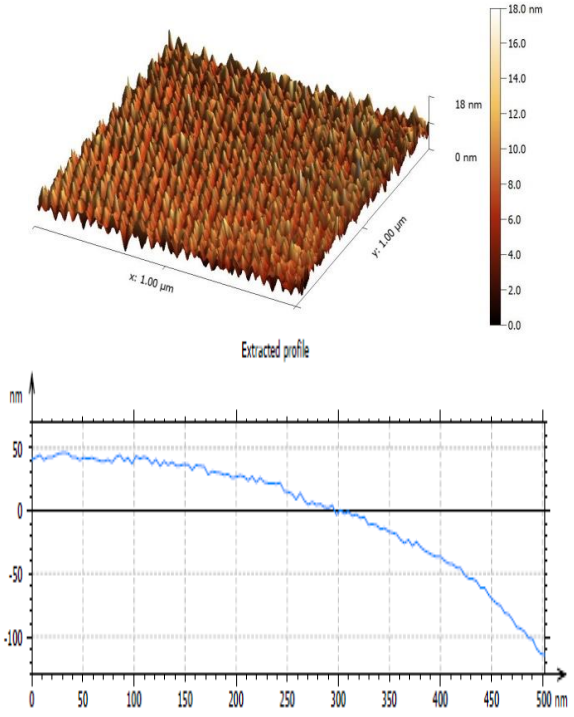

Fig. (7) AFM result of the CuO NPs prepared in this work

One peak can be seen at 496nm in the photoluminescence (PL) spectrum (Fig. 8) of CuO nanoparticles. Defect states coming from the emission mediated between oxygen (O) vacancies and copper (Cu) interstitials are responsible for the blue emission peak at 496nm [23,24]. Due to the existence of valence defects in the synthesized nanoparticles, an indirect interband transition peak at 496nm has been identified [25-27].

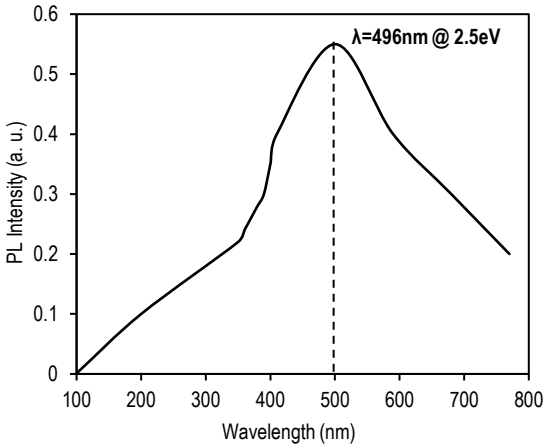

Fig. (8) PL spectrum of the CuO NPs prepared in this work

For a photodetector, particular responsivity and detectivity are crucial factors. In the wavelength range of 400-900nm with a 5V bias, the spectral responsivity of the fabricated structures is studied and computed using the following equation:

$$R_\lambda = \frac{I_{Ph}}{P_{in}} \quad (A/W) \qquad (6)$$

Two heterojunctions make up Si/Ag; the first is between the CuO layer and porous silicon (CuO/PSi), and the second is between the porous silicon layer and crystalline (substrate) silicon (PSi/Si). Consequently, there are two depletion zones formed in the CuO/PSi/(n,p)-Si.

Figure (9) demonstrates the spectral responsivity and specific detectivity of the CuO/PSi/(n,p)-Si as functions of wavelength after being etched for 15 min at a current density of 20 mA/cm^2. The spectral responsivity curve of CuO/PSi/(n,p)-Si has two response peaks, the first peak being due to the absorption edge of CuO nanoparticles at 640 nm and the second area being related to the absorption edge of silicon at 850 nm.

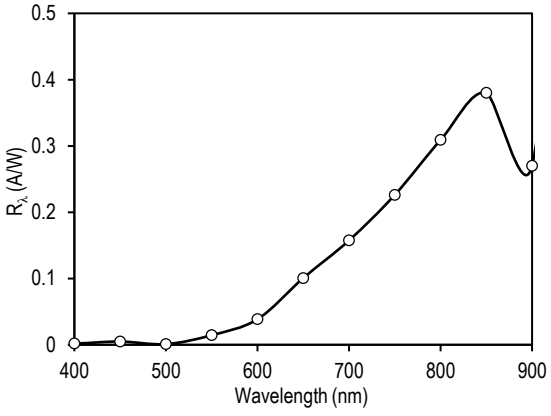

(a)

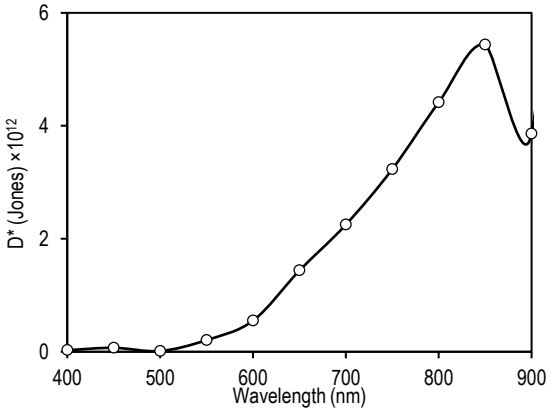

(b)

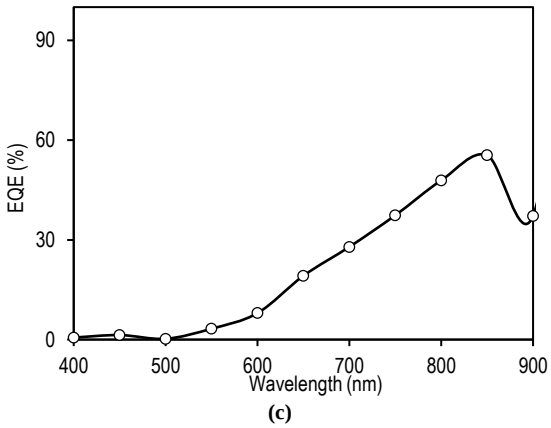

(c)

 ISSN (print) 1813-2065, (online) 2309-1673

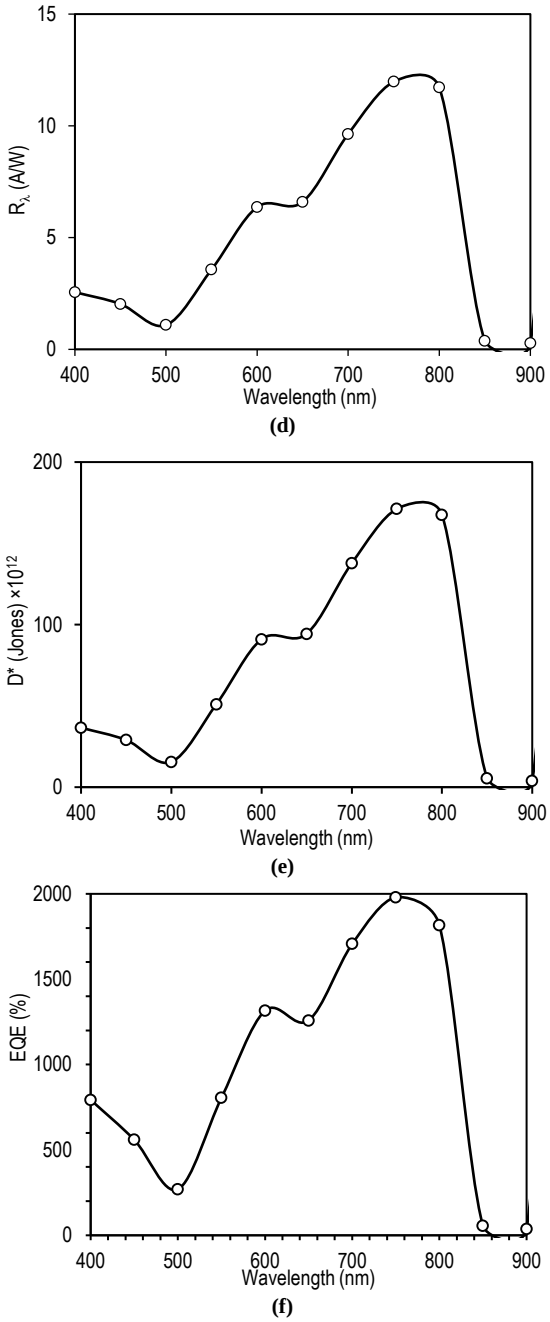

Fig. (9) The spectral responsivity (R_λ), specific detectivity (D^*) and external quantum efficiency (EQE) of the CuO/PSi/n-Si structure (a-c), and of the CuO/PSi/p-Si structure (d-f)

It is worth noting that the CuO samples prepared by the chemical precipitation method contain very small nanoparticles, which make them promising material in the photonic and optoelectronics applications due to their effects on the values of energy gap and the generated currents [28]. The results conclusively explain the band gap alteration due to different confinement sizes which lead to the phenomenon above.

4. Conclusions

Chemical precipitation method was successfully used to prepare CuO nanoparticles. Their structural and spectroscopic characteristics introduced and discussed. The structural characterizations revealed the development of monoclinic CuO with an average particle size of 51.21 nm. An optical energy band gap of 5.1 eV was determined. The photoluminescence spectrum showed five major peaks at 334.2, 466.8, 630, 765.8, and 830 nm. Moreover, the main parameters of photodetectors fabricated from the Ag/CuO/PSi/(n,p)Si/Ag structures were determined and compared.

References

[1] M.A. Hameed, S.H. Faisal, R.H. Turki, "Characterization of Multilayer Highly-Pure Metal Oxide Structures Prepared by DC Reactive Magnetron Sputtering Technique", *Iraqi J. Appl. Phys.*, 16(4) (2020) 25-30

[2] C. Jianliang et al., "Synthesis of porous hematite nanorods loaded with Cuo nanocrystals as catalysts for CO oxidation", *J. Nat. Gas. Chem.*, 20 (2011) 669- 676.

[3] K. Jess et al., "Advances in copper-chalcopyrite thin films for solar energy conversion", *Solar Ener. Mater. Solar*, C94 (2009) 12-16.

[4] Z. Yang et al., "Gas-sensing properties of hollow and hierarchical copper oxide microspheres", *Sensor*, 128 (2007) 293 298.

[5] R.H. Bohr et al., "Field emission studies of amorphous carbon deposited on copper nanowires grown by cathodic arc plasma deposition", *New Carbon Mater.*, 24 (2009) 97-101.

[6] Asraa M. Hameed and Mohammed A. Hameed, "Highly-Pure Nanostructured Metal Oxide Multilayer Structure Prepared by DC Reactive Magnetron Sputtering Technique", *Iraqi J. Appl. Phys.*, 18(4) (2022) 9-14.

[7] K. Manmeet et al., "Growth and branching of CuO nanowires by thermal oxidation of copper", *J. Cryst. Growth*, 289 (2011) 670-675.

[8] W. Narongdet et al., "Synthesis and Characterization of Copper Oxide Nanoparticles", *Energy Procedia*, 29 (2011) 404-409.

[9] M.H. Yamukyan, K.V. Manukyan and S.L. Kharatyan, "Copper oxide reduction by combined reducers under the combustion mode", *Chem.*, 137 (2008) 636 642.

[10] O.A. Hamadi, "The Fundamentals of Plasma-Assisted CVD Technique Employed in Thin Films Production", *Iraqi J. Appl. Phys. Lett.*, 1(2) (2008) 3-8.

[11] Asraa M. Hameed and Mohammed A. Hameed, "Spectroscopic characteristics of highly pure metal oxide nanostructures prepared by DC reactive magnetron sputtering technique", *Emergent Materials*, 6 (2022) 627-633.

[12] O.A. Hammadi et al., "Employment of Magnetron to Enhance Langmuir Probe Characteristics of Argon Glow Discharge

Plasma in Sputtering System", *Iraqi J. Appl. Phys.*, 12(4) (2016) 19-28.
[13] J. Zhu et al., "Highly dispersed CuO nanoparticles prepared by a novel quick-precipitation method", *Mater. Lett.*, 58 (2004) 3324-3327.
[14] W. Rujun et al., "Preparation and characterization of CuO nanoparticles with different morphology through a simple quick-precipitation method in DMAC water mixed solvent", *J. Alloy Comp.*, 504 (2010) 45-49.
[15] R.K. Fakher Alfahed et al., "Synthesis, morphological and optical characterizations of the poly (O-toluidine)-LiCl networks thin film" *Opt. Laser Technol.*, 133 (2021) 106524.
[16] K.J. Arun et al., "Surfactant Free Hydrothermal Synthesis of Copper Oxide Nanoparticles", *Am. J. Mater. Sci.*, 5(3A) (2015) 36-38.
[17] H. Siddiqui, M. Qureshi and F.Z. Haque, "Valuation of copper oxide (CuO) nanoflakes for its suitability as an absorbing material in solar cells fabrication", *Optik Int. J. Light Electron Opt.*, 127(5) (2016) 3713-3717.
[18] B. Kadem et al., "Morphological, structural, optical, and photovoltaic cell of copolymer P3HT:ICBA and P3HT:PCBM", Optik, 204 (2020) 164153.
[19] R.K. Fakher Alfahed et al., "Structural, morphological, and Z-scan technique for a temperature-controllable chemical reaction synthesis of zinc sulfide nanoparticles", *Appl. Phys. B*, 125 (2019) 1-11.
[20] C. Lu et al., "Simple Template-Free Solution Route for the Controlled Synthesis of $Cu(OH)_2$ and CuO Nanostructures", *J. Phys. Chem. B*, 108(46) (2004) 17825-17831.
[21] E. Gadelmawla et al., "Roughness parameters", *J. Mater. Process. Technol.*, 123 (2002) 133-145.
[22] N. Misdan et al., "Study on the thin film composite poly (piperazine-amide) nanofiltration membrane: impacts of physicochemical properties of substrate on interfacial polymerization formation", *Desalination*, 344 (2014) 198-205.
[23] R. Rawat et al., "Synthesis of CuO hollow nanoparticles using laser ablation: effect of fluence and solvents", *Appl. Phys. A*, 126 (2020) 226.
[24] A. El-Trass et al., "CuO nanoparticles: Synthesis, characterization, optical properties and interaction with amino acids", *Appl. Surf. Sci.*, 258(7) (2012) 2997.
[25] H. Siddiqui, M. Qureshi and F.Z. Haque, "Surfactant assisted wet chemical synthesis of copper oxide (CuO) nanostructures and their spectroscopic analysis", *Optik Int. J. Light Electron Opt.*, 127(5) (2016) 2740-2747.
[26] C. Tamuly et al., "Reduction of aromatic nitro compounds catalyzed by biogenic CuO nanoparticles", *RSC Adv.*, 4(95) (2014) 53229-53236.
[27] P. Chand et al., "Effect of NaOH molar concentration on morphology, optical and ferroelectric properties of hydrothermally grown CuO nanoplate", *Mater. Sci. Semicond. Process.*, 38 (2015) 72-80.
[28] A. Virdian et al., "The effect of surface morphology in copper oxide nanostructure to photo detector characteristics", *J. Phys.: Conf. Ser.*, 877 (2017) 012024.

 ISSN (print) 1813-2065, (online) 2309-1673

IRAQI JOURNAL OF APPLIED PHYSICS
Vol. 19, No. 3A, July-August 2023, pp. 43-48

Synthesis and Characterization of Ceramic System Beta Tri-calcium Phosphate Used in Teeth and Bones Substitutions

Jafer F. Odah[1]
Fadhil K. Farhan[1]
Mazin M. Mawat[2]

[1] *College of Science, Al-Karkh University for Sciences, Baghdad, IRAQ*
[2] *College of Medicine, Wasit University, Kut, Wasit, IRAQ*

Beta tri-calcium phosphate is due to its superior degradation in vivo, osteoconductivity, and osteoinductivity qualities, has become a promising material for bone regeneration applications. In addition, it is compatible with body tissues and has the ability to integrate bone, being very similar to the bone of an organism in addition to being a material with a very low thermal expansion coefficient, which makes it a desirable material for a wide range of applications in the field of biomedicine. In this work, beta tri-calcium phosphate was synthesizing by the reaction of calcium hydroxide and phosphoric acid at room temperature using a precipitation chemical method. Sodium hydroxide was use as a catalyst to fixing the pH at a range of (10-11). Scanning electron microscope and energy dispersion were used to investigate the characteristics particularities of these scaffolds. Final scaffold was immersed in simulated body fluid to help tissue correlation. Finally, Vickers microhardness, mechanical impact strength, Young's modulus and compressive strength were calculated for the prepared composites. The outcomes turn up a good linkage correlate between the prepared samples with human's teeth and bones substitutions.

Keywords: Bio-ceramics, hydroxyapatite, bones substitutions, beta tri-calcium phosphate
Received: 4 January 2023; **Revised:** 18 February 2023; **Accepted:** 25 February 2023

1. Introduction

Due to their bioactive qualities, calcium phosphate (CaP) ceramics are extensively researched for orthopedic and dental applications. A chemical link is typically formed to this tissue bone-bonding when bioactive molecules contact with the nearby bone. Beta tri-calcium phosphate [$Ca_3(PO_4)_2$] (TCP) is one of most important bio-ceramic systems due to their identification in structure and properties with hydroxyapatite [$Ca_{10}(PO_4)_6(OH)_2$] (HA), which is the major mineral built-up of bones and teeth, it has been established that nano-sized hydroxyapatite increases the bioactivity of biomaterials. The bioactivity of composed of (HA) and (TCP) have been broadly exemplified. The resulting mechanical characteristics, biodegradability, and stability are all confined by an established equilibrium between HA and TCP, despite the fact that the two phosphates appear to have differing biological resorption capacities [1, 2]. Co-precipitation or acid–base titration can be used to produce both HA and TCP bio-ceramics from aqueous solutions containing calcium nitrate and di-ammonium hydrogen phosphate. They've been made via a wet-chemical process by various researchers [3, 4, 5, 6, 7] and using both Ca $(NO_3)_2.4H_2O$ and $(NaHPO_4)$ as precursors in all of this research. Tas et al. [8], Akao et al. [9] and Jarcho et al. [10]. In the current study, tri-calcium phosphate was synthesized using a precipitation chemical method due the simplicity of this method also the final sample obtainable from this method had a high homogeneity.

A tri-calcium phosphate compound, or calcium phosphate group, which can be obtained by altering and manipulating the molar ratios of the calcium-phosphorus complex to match them with bone tissue. The hardness and hardness of the compound comes because of the correct and effective association between phosphorous and calcium in the presence of cofactors while keeping the pH value above 10. At room temperature, two types of calcium phosphate were form, which are stable and compatible with the body fluid. At high temperatures at 1200 ^oC, this is done through the reaction of the compound in a thermal furnace in the presence of oxygen. In this case, we get the hydroxyapatite compound when these new compounds interact with the body fluid [11].

Due to its macro porosity, beta tri-calcium phosphate has significant osteoconuctive ability, resulting in strong and healthy bone formation. It fuses straight to the bone, enhancing the healing process at the extraction site. The effect of a tri-calcium phosphate on bone density around newly implanted dental implants has been extensively studied in several articles. When tri-calcium phosphate was introduced to certain areas of the body, bone density assessments increased.

In previous years, over decades, types of bone restoration and replacement were use, including ceramic, including organic, and self-replacement [13-16]. Which showed tissue compatibility with the organism. Among the most important ceramic materials that are biocompatible with the body are the group of calcium phosphate and hydroxyapatite,

which are unique in properties for the engineering of body tissues [17-19].

Both HA and tri-calcium phosphate materials have been studied, and encouraging results have been obtained for fields of biotechnology (bone substitute or regenerate bone tissue) and material sciences.

The bone morphogenetic proteins (BMP) are huge group of proteins involves of more than twenty BMPs, but a few of them such BMP7 have important role in osteogenesis and bone formation, and these proteins were obtaining from non-mineralized cells to osteoprogenitor cells, therefore they have become one of likely treatment option [20].

Bioceramic materials such as calcium phosphate and other compounds such as alumina, zirconia, silica and calcium carbonate in addition to calcium titanium can be used as a coating material for metal alloys, which enhances their strength and resistance to corrosion, as well as to increase the bond of these minerals to integrate with the tissues of the body [21]. The use of synthetic bone protein and adding it to ceramic materials will increase bone perfection and the speed of fusion in addition to the release of calcium and phosphorous, which are included in the composition of bone and are the main elements in it [22]. The use of nanotechnology in medical applications [23,24], especially in orthopedics, has led to a great development in providing promising materials with unique properties and interest in this field encouraged researchers to create prosthetic materials and new techniques in replacement and grafting. HA composite and its usage in medical application as bones and teeth substitutions after proceedings of a several investigations and tests.

2. Experimental Part

A precipitation chemical method was used to synthesized beta tri-calcium phosphate as following: A 10 gm of CaO is mixed with 300ml distilled water at 27°C to get a white $Ca(OH)_2$ suspension. A 0.3 M of H_3PO_4 was subsequently add to the last suspension under continuous stirring to get a final suspension at pH ranged 10-11 with assistance of adding sodium hydroxide. The mixture was stirred for one hr. at fixed temperature. Precipitates were separate from the glassware immediately by filtration and dried at 60°C for one day. Finally, the sample was sintering at 400°C for 4 hours to resulting the final Ca-P powder.

Characteristics tests were acquired such (XRD) at three temperatures (400, 800 and 1000°C). At 1000°C, the tri-calcium phosphate will have formed and this final production will have compressed as bulk with dimensions 1x1 cm^2 using hydraulic compressor. Scanning electron microscopy (SEM), energy-dispersive x-ray (EDX) spectroscopy and x-ray diffraction (XRD) were used to investigate the characteristics of these scaffolds. A tri-calcium phosphate scaffold was mash in 250 ml of (SBF) for 30 days at 37°C without stirring and dark place after adding 5% of BMP to the scaffold to help tissue correlation. After that a HA forming in the TCP scaffold's surface as obvious white layer, the homogeneity of HA/tri-calcium phosphate composite was checked by (XRD) after calcination at 600°C for 2 hours. Finally, Vickers micro hardness, mechanical impact strength, Yong's modulus and compressing strength for this composite were calculated.

3. Results and Discussion

The EDX analysis for the final scaffold product is shown in Fig. (1). From EDX data, the Ca-P ratio of the bone hydroxyapatite (BHA) under investigation varies by as much as 3:1. As can be shown from the HA weight and atomic composition (Fig. 1). (Ca, P, and O_2) are the primary components of (HAp) and there is a small amount of Na and Mg in the EDX of (BHA) is consistent with published studies [25].

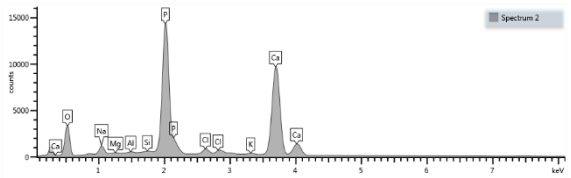

Element	Wt.%	Wt.% Sigma
O	41.67	0.28
Na	2.65	0.07
Mg	0.15	0.04
Al	0.24	0.03
Si	0.23	0.03
P	23.77	0.15
Cl	1.47	0.04
K	0.38	0.03
Ca	29.45	0.17
Total:	**100.00**	

Fig. (1) EDX analysis for final scaffold product in SBF

The x-ray diffraction (XRD) analysis was carried out for the prepared samples. The (2θ) range was from 10° to 80°. Data used for structural investigation were collect in the 2θ range of 10-100° with a 0.026° step and counting time of 500 s/step. The XRD pattern of obtained beta-TCP using wet chemistry synthesized is shown in Fig. (2). The most-intense XRD peaks were at 40.7° and 47.4° of the CaO product phase coincided with those of HA and beta-TCP respectively. Also figure (2) shows intense peaks at 25.8°, 31.7- 3°, 39.8°, 47-48°, 49.5° and 53.2°, attesting that the synthetized Ca-P has a crystalline HA. The peaks at 30-35° indicated the presence of a crystallinity of nano-sized hydroxyapatite [26]. XRD examination of the Ca-P synthetized at low pH appearing the main specific peaks of HA at 2θ such 25.8°, 31.7°, 32.2°, 32.8°, 34.1°, 46.9° and 49.4°, and main peaks for tri-calcium phosphate are 25.8°, 26.5°, 29.6°, 32.8° and 34.3° [27]. The morphology of tri-calcium phosphate and HA particles synthetized at 400, 800 and 1000°C, particles at pH ranging in 10-

 ISSN (print) 1813-2065, (online) 2309-1673

11 and final scaffold were observed using (SEM) and shown in Fig. (3).

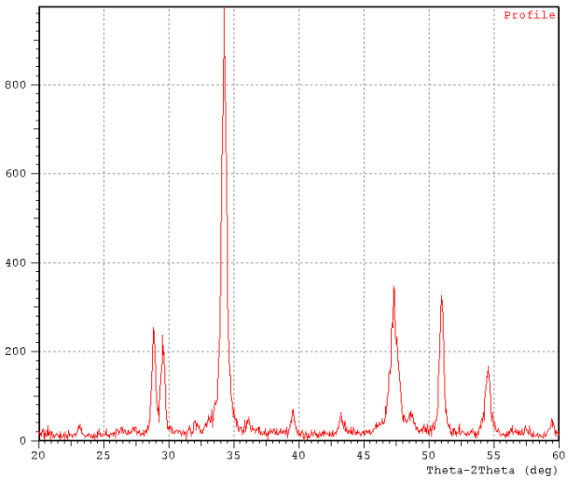

(a)

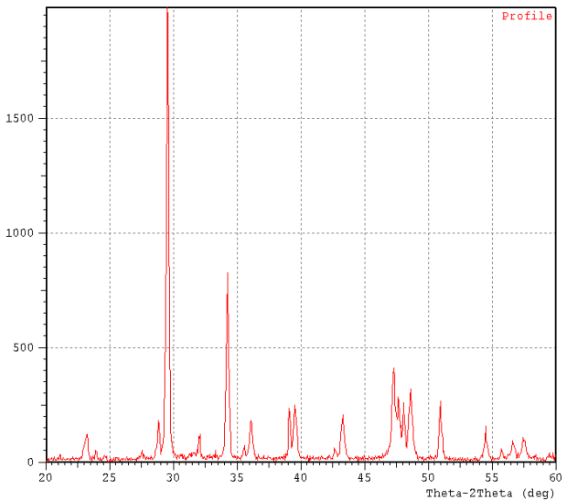

(b)

Fig. (2) (a) XRD of beta-TCP at 600°C and (b) XRD of TCP/HA composite after calcination at 1000°C for two hours

Scanning electron microscopy images indicated that the granular size of the powder is within the nanoscale range with little clumping of the prepared powder. The morphology is resembled between the samples synthetized at different temperatures as shown in Fig. (3). However, at 1000°C, the particle size will decrease. A Ca-P condensed as spheroidal shape and micro-pores, being the sample treated at 1000°C the most condensed.

The bioactivity examines of the tri-calcium phosphate scaffold showed that morphological changes. Figure (4) shows the result of dipping into a body fluid-simulated solution after 30 days; the all sample had an elementary change on the scaffolds surface and tend to white colored due HA forming as shown in Fig. (4a).

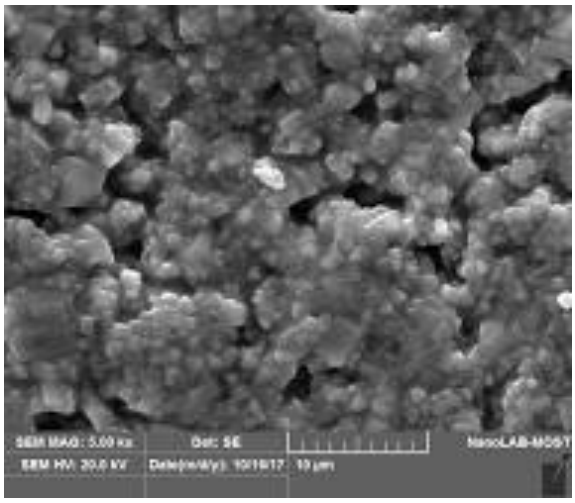

(a)

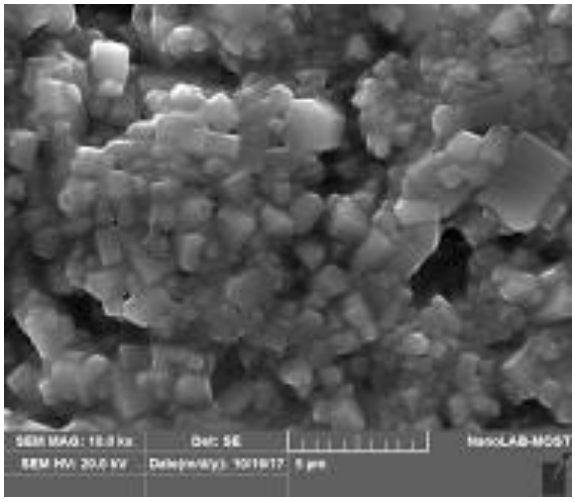

(b)

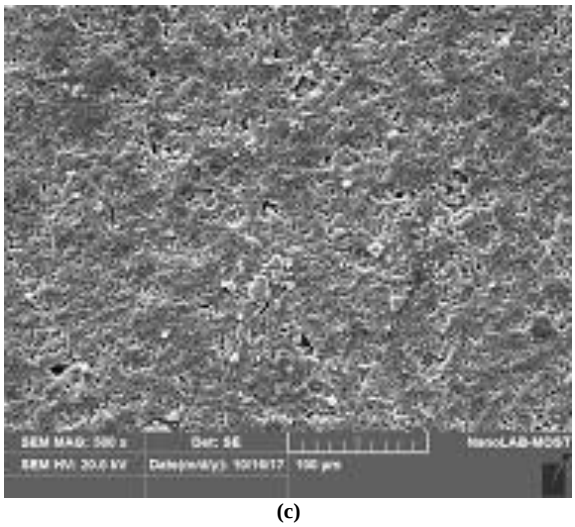

(c)

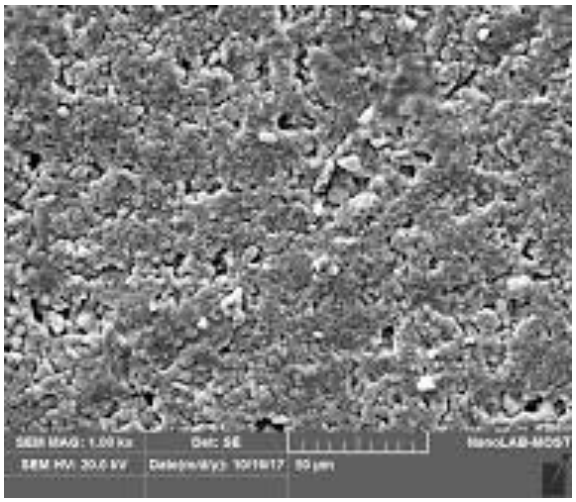

(d)

Fig. (3) SEM for final scaffold product

The use of the sintering temperature at 1000°C made the compound have high performance (biomechanical) properties. As a result, mechanical properties were obtained close to the bone of the organism. The shape represents the hip joint made of calcium phosphate (Fig. 4b). Because of the great strength of the ionic bonds in tri-calcium phosphate, it is generally fragile. The crystallinity, size, borders, and grain porosity of HA and tri-calcium phosphate can be used to identify their mechanical properties. With smaller grains, the number of grain boundaries decreases, resulting in an improvement in mechanical strength. It is useful to coat beta tri-calcium phosphate scaffolds with HA to boost the mechanical strength of porous ceramic materials.

In fact, beta tri-calcium phosphate-based scaffolds coated with bioabsorbable HA provide a novel way to obtain good compressive strength while preserving high levels of biocompatibility, biodegradability, and osteoconductibility. The interpenetrating structure that resulted is presumably what gave the scaffold its strength.

A comparison of mechanical properties between the finished scaffold product and various ceramic materials and some hard tissues of the human body is shown in table (1).

Table (1) the final scaffold product's mechanical properties are compared to those of several human tissues

Material	Compressive Strength (MPa)	Flexural Strength (MPa)	Modulus of Elasticity (GPa)	Ref.
Final scaffold product	190	210	1.6	
hydroxyphosphate.	400	112	40-120	[28]
Zirconia	1800	600	195-210	[29]
Alumina	1000-2500	200-380	350-400	[30]
Bone	100-200	90-120	3-30	[31]
Teeth	300	51.7	15-20	[32]
Tooth enamel	250-550	10.3	10-90	[33]

(a)

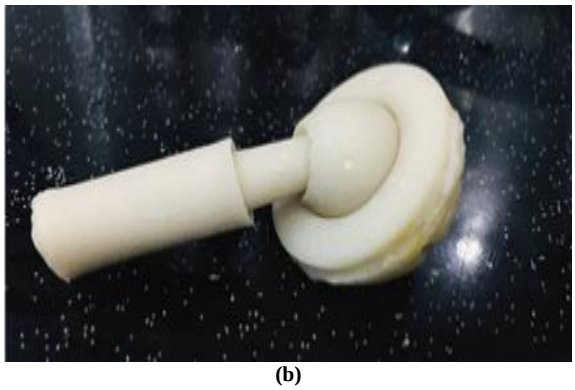

(b)

Fig. (4) (a) before (left) and after (right) immersed in SBF, and (b) hip join

Comparing the resultant scaffold with the materials mentioned in table (1), ceramic system of tri-calcium phosphate synthesis in this work with mentioned ratios is within the mechanical properties ranging of cortical bone for the compressive strength and the other properties could be closer whether the ratios be more suitable and accurate the calcination temperature.

4. Conclusion

The manufacturing properties of the compound tri-calcium phosphate bio ceramic associated with hydroxyapatite and tri-calcium phosphate particles were acquire with nano-dimensional size distribution, for with high hand the agglomeration in more stable structures that they conformed. A clear XRD test of the prepared powder showed a multi-phase crystallization of a tri-calcium phosphate compound in addition to a pattern of calcium phosphate with hydroxyapatite. The structural and mechanical properties of the synthesized tri-calcium phosphate are suitable for their use as biomaterials, which make this product a good material for bones and teeth regeneration reliance on the mechanical properties.

Acknowledgement

We would like to thank the Department of Medical Physics, College of Science at Al-Karkh University for Sciences for their generous of using lab work for this research paper and ministry of higher education and scientific research.

 ISSN (print) 1813-2065, (online) 2309-1673

References

[1] A.C. Tas et al., "An Investigation of the Chemical Synthesis and High-Temperature Sintering Behaviour of Calcium Hydroxyapatite (HA) and Tricalcium Phosphate (TCP) Bioceramics", *J. Mater. Sci.: Mater. Med.*, 8 (1997) 91-96.

[2] R. Adamski and D. Siuta, "Mechanical, Structural, and Biological Properties of Chitosan/Hydroxyapatite/Silica Composites for Bone Tissue Engineering", *Molecules*, 26(7) (2021) 1976.

[3] J.M. Bouler et al., "Biphasic calcium phosphate ceramics for bone reconstruction: A review of biological response", *Acta Biomater.*, 53 (2017) 1-12.

[4] B. Bragdon et al., "Bone morphogenetic proteins: A critical review", *Cell. Signal.*, 32 (2011) 609-620.

[5] W. Cao and L.L. Hench, "Bioactive materials", *Ceram. Int.*, 22(6) (1996) 493-507.

[6] M. Ebrahimi and M. Botelho, "Biphasic calcium phosphates (BCP) of hydroxyapatite (HA) and tricalcium phosphate (TCP) as bone substitutes", Importance of physicochemical characterizations in biomaterials studies, *Data in Brief*, 10 (2017) 93-97.

[7] H. Ibrahim, "Nanotechnology and Its Applications to Medicine: an overview", *Int. J. Med.*, 113(1) (2020) hcaa060.008.

[8] T.T. Hegi et al., "Cell-mediated BMP-2 liberation promotes bone formation in a mechanically unstable implant environment", *Bone*, 46 (2010) 1322-1327.

[9] I. Denry and L.T. Kuhn, "Design and characterization of calcium phosphate ceramic scaffolds for bone tissue engineering", *Dent. Mater.*, 32 (2016) 43-53.

[10] J. Black and G. Hastings, **"Handbook of Biomaterial Properties"**, Springer (2013).

[11] K. Uematsu et al., ''Transparent HA Prepared by HIP of Filter Cake", *J. Am. Ceram. Soc.*, 72 (1989) 1476–1478.

[12] K. Yamashita et al., ''Trivalent-Cation-Substituted Calcium Oxyhydroxyapatite", *J. Am. Ceram. Soc.*, 69 (1986) 590–594.

[13] W. Koechner, **"Solid-State Laser Engineering"**, 6th ed., Springer, USA (2006).

[14] M. Akao et al., "Dense Polycrystalline b-Tricalcium Phosphate for Prosthetic Applications", *J. Mater. Sci.*, 17 (1982) 243-246.

[15] M. Asada et al., "HA Crystal Growth on Ca-HA Ceramics", *J. Mater. Sci.*, 23 (1988) 3202–3205.

[16] M. Jarcho et al., "HA Synthesis and Characterization in Dense Polycrystalline Form", *J. Mater. Sci.*, 11 (1976) 2027-2035.

[17] M. Jarcho et al., "Synthesis and Fabrication of b-TCP (Whitlockite) Ceramics for Potential Prosthetic Applications", *J. Mater. Sci.*, 14 (1979) 142-150.

[18] M. Iskaros et al., "Does B-Tricalcium Phosphate Work as a Bone Regenerative Material", *J. Dent. Oral Biol.*, 2(18) (2017) Article 1106.

[19] C. Marques et al., "Biocompatibility and antimicrobial activity of biphasic calcium phosphate powders doped with metal ions for regenerative medicine", *Ceram. Int.*, 43 (2017) 15719-15728.

[20] M. Rufino Senra and M. de Fátima Vieira Marques, "Synthetic Polymeric Materials for Bone Replacement", *J. Compos. Sci.*, 4 (2020) 191, doi:10.3390/jcs4040191.

[21] M. Mabrouk et al., "Nanomaterials for Biomedical Applications: Production, Characterisations, Recent Trends and Difficulties", *Molecules*, 26 (2021) 1077.

[22] P.E. Wang and T.K. Chaki, "Sintering Behavior and Mechanical Properties of HA and Dicalcium Phosphate", *J. Mater. Sci: Mater. Med.*, 4 (1993) 150–158.

[23] G. Poinern et al., "Synthesis and characterization of nanohydroxyapatite using an ultrasound assisted method", *Ultrason. Sonochem.*, 16 (2009) 469-474.

[24] M. Prakasam et al., "Fabrication, properties and applications of dense hydroxyapatite: a review", *J. Func. Biomater.*, 6(4) (2015) 1099-1140.

[25] Q. Ali et al., "Role of Modern Technologies in Tissue Engineering", *Archives Neurosci.*, 7(1) (2020) e90394.

[26] R.Z. LeGeros and J.P. LeGeros, **"An Introduction to Bioceramics"**, L.L. Hench, J. Wilson (Eds.), World Scientific (Singapore, 1993) 139.

[27] K. Shim et al., "Surface Immobilization of biphasic calcium phosphate nanoparticles on 3D printed poly (caprolactone) scaffolds enhances osteogenesis and bone tissue regeneration", *J. Ind. Eng. Chem.*, 55 (2017) 101-109.

[28] M.V. Silva et al., "Ceramic armors for ballistic applications: a review", *Cerâmica*, 60(355) (2014) 323-331.

[29] V.V. Silva, R.Z. Domingues and F.S. Lameiras, "Microstructural and mechanical study of zirconia-hydroxyapatite (ZH) composite ceramics for biomedical applications", *Comp. Sci. Technol.*, 61(2) (2001) 301-310.

[30] F. Tamimi, Z. Sheikh and J. Barralet, "Dicalcium phosphate cements: Brushite and monetite", *Acta Biomater.*, 8 (2012) 474-487.

[31] Z. Wang et al., "Applications of Calcium Phosphate Nanoparticles in Porous Hard Tissue Engineering Scaffolds", *Nano*, 7(4) (2012) 1230004.

[32] T. Winkler et al., "A review of biomaterials in bone defect healing, remaining shortcomings and future opportunities for bone tissue

engineering", *Bone Jt. Res.*, 7(3) (2018) 232–243.
[33] Y. Hu et al., "Enhanced reparative dentinogenesis of biphasic calcium phosphate ceramics containing calcium-deficient hydroxyapatite (CDHA) and strontium-incorporated CDHA in direct pulp capping", Mater. Today Commun., 33 (2022) 104231.
[34] C. Gervais, C. Bonhomme and D. Laurencin, "Recent directions in the solid-state NMR study of synthetic and natural calcium phosphates", Sol. Stat. Nucl. Mag. Reson., 107 (2020) 101663.
[35] N. Ramesh et al., "Calcium-based ceramic biomaterials", ed. Cuie Wen, in Biomaterials, Structural Biomaterials, Woodhead Publishing (2021) 333-394.
[36] S. Johnson Jeyakumar et al., "Preparation and analysis of pure and surface modified nanohydroxyapatite derived from eggshells and its in-vitro studies for bone graft applications", Cer. Int., 49(11B) (2023) 18708-18727.
[37] M. Edén, "Structure and formation of amorphous calcium phosphate and its role as surface layer of nanocrystalline apatite: Implications for bone mineralization", Materialia, 17 (2021) 101107.
[38] A. Nisar et al., "Study of physico-mechanical and electrical properties of cerium doped hydroxyapatite for biomedical applications", Mater. Chem. Phys., 299 (2023) 127511.
[39] C.M. Mardziah et al., "Effect of zinc ions on the structural characteristics of hydroxyapatite bioceramics", Cer. Int., 46(9) (2020) 13945-13952.

 ISSN (print) 1813-2065, (online) 2309-1673 PRINTED IN IRAQ

IRAQI JOURNAL OF APPLIED PHYSICS
Vol. 19, No. 3A, July-August 2023, pp. 49-54

Structural Characteristics of TiO_2/TiN Nanocomposites Synthesized by DC Reactive Magnetron Sputtering Technique

Mays K. Ali
Firas J. Kadhim

Department of Physics, College of Science, University of Baghdad, Baghdad, IRAQ

In this work, nanocomposites from titanium dioxide (TiO_2) and titanium nitride (TiN) thin films were prepared by dc reactive magnetron sputtering technique. A highly-pure titanium sheet was used as a sputtering target and gas mixtures of ($Ar:O_2$) and ($Ar:O_2:N_2$) with missing ratios of (50:50) and (40:40:20) were used to prepare TiO_2 and TiO_2:TiN samples, respectively. The structural and morphological characteristics of these samples were investigated. They showed that the TiO_2 samples contain both anatase and rutile phases with no other materials as impurities, while an additional phase of TiN structure was found in the TiO_2/TiN samples. Reasonable changes in the chemical structure and surface morphology were shown due to the formation of the nanocomposite material when compared to the TiO_2 samples.

Keywords: Titanium dioxide; Titanium nitride; Nanocomposites; Reactive sputtering
Received: 10 February 2023; **Revised:** 23 March 2023; **Accepted:** 30 March 2023

1. Introduction

Nature often creates structures that incorporate hierarchical features, from the tiny cell all the way to large forests. One can observe a rule of growth that is applied repeatedly to construct the next stage of the structure. Many man-made materials too involve structural elements within their structure. Such structural hierarchies can play a large role in determining the bulk properties of the materials [1]. When structures inspired by nature are fabricated in the nanoscale dimensions, the physical properties of the starting materials can be modified considerably to provide great opportunities to enhance their performance for many different technological applications [2].

Among all semiconductor photocatalysts, titanium dioxide (TiO_2) is receiving high concern as a promising material due to its evidence properties, including chemical stability, highly photocatalytic activity, ability to deposit as thin film, and environmentally friendly [3-5]. From the three distinct polymorphs of TiO_2, rutile and anatase phases are the most stable forms [6]. While rutile TiO_2 has a direct bandgap and anatase TiO_2 has an indirect bandgap, the latter has a wider bandgap (3.2 eV) [7,8]. There are several methods and techniques used for the deposition of titanium oxide thin films such as spray pyrolysis [9], chemical vapor deposition [10], thermal vacuum evaporation [11], radio-frequency sputtering [12], and reactive dc magnetron sputtering [13]. Despite the high cost of sputtering technique under high vacuum, it remains amongst the important and widely used techniques in many fields due to the purity and homogeneity of the nanostructures produced by this technique [14,15].

The characteristics of nanocrystalline TiO_2 thin films can be improved by different routes including preparation technique, engineering of nanostructure shape and size, or composing with other materials [16,17]. Pure TiO_2 thin films have a wide bandgap, which restricts their photosensitivity to the UV radiation, which represents a drawback in photocatalytic applications [18]. In order to enhance the photocatalytic activity, many methods have been used to expand the light response to the visible ranges. The most popular method to do so is the preparation of doped TiO_2 material as nanoparticles. There have been several methods for doping the TiO_2 with metals, non-metals (such as nitrogen), and semiconductors [19].

Since the p states of nitrogen (N) atom mix with O^2_p states help in narrowing the bandgap of TiO_2, substitutional doping of N is the most successful. Although doping with sulfur (S) exhibits a comparable bandgap narrowing, due to its large ionic radius, it would be challenging to incorporate it into the TiO_2 crystal, as shown by the significantly higher formation energy needed for the substitution of S than for the substitution of N atoms [20].

Al-Oubidy and Kadhim [21] have studied the structural characteristics of TiO_2 nanostructures prepared by dc reactive magnetron sputtering without any heat treatment. These nanostrcutures exhibited anatase phase only with average particle size of 5-7 nm. Shanmuga et al. have reported the synthesis and characterization of pure TiO_2 as well as N-, B-, and Ag-doped TiO_2 using the sol-gel method and the ability of these oxides to photodegrade methylene blue (MB) under sunlight or UV- radiation. Photocatalytic efficiency was significantly increased by N-doping, resulting in 98% MB decomposition

under UV- irradiation for 180 min, while Ag- and B-doped TiO_2 lowered the degradation rates. Photocatalysis with N-doped TiO_2 was proved to be a promising alternative for photocatalysis employing solar energy [22].

As an outcome of this work, new nanocomposites from titanium dioxide (TiO_2) and titanium nitride (TiN) thin films were prepared by dc reactive magnetron sputtering technique for photocatalysis applications. The structural and morphological characteirstics of these nanocomposites are studied and compared to those of individual TiO_2 nanostrcutures.

2. Experimental Part

A dc reactive magnetron sputtering system was used to prepare TiO_2 thin films and TiO_2:TiN thin film nanocomposite on glass substrates. A highly-pure titanium sheet of 4cm diameter was mounted on the cathode inside deposition chamber of the sputtering system. The magnetron configuration consists of two permanent ring magnets positioned on the cathode's backside. The inner magnet is 31 mm in diameter with a 17 mm diameter central hole, while the outer magnet is 80 mm in diameter and 40 mm diameter central hole. The inter-electrode distance was fixed at 4 cm, the working pressure was 0.085 mbar and the deposition time of 3 hours was considered to prepare the optimum samples. The anode might be heated up to 350°C using a controlled heating system. Argon was used as a sputtering gas, as well as nitrogen and oxygen as reactive gases. The TiO_2 samples were prepared using gas mixture (Ar:O_2) with mixing ratio of 50:50, while the TiO_2:TiN samples were prepared using gas mixture ($Ar/O_2/N_2$) with five different mixing ratios in order to control the contents of TiO_2 and TiN in the final sample. It was found that the optimum mixing ($Ar/O_2/N_2$) ratio was (40/40/20), which produces the highest content of TiN in the prepared nanocomposite.

The structural and surface morphology of the prepared samples were examined by x-ray diffraction (Shimadzu XRD 6000), scanning electron microscopy (JSM-7600F by JEOL), and Fourier-transform infrared (FTIR) spectroscopy.

3. Results and Discussions

Figure (1) illustrates the x-ray diffraction (XRD) patterns recorded for the as-deposited TiO_2 and TiO_2:TiN thin film prepared on glass slides. The two samples appeared as polycrystalline nature. The TiO_2 samples appeared of mixed Anatase and Rutile phases according to the standard cards No. 96-900-9087, and 96-900-7532, respectively, which indicated the oxidation of the sputtered substances. The preferred orientation peak appeared for the dominant anates phase located at diffraction angles of 2θ=25.39°, corresponding to the (101) crystal planes. Addition of N_2 cause to appeared new phase of TiN with peaks located at 2θ = 36.8340°, 42.7363°, 62.0139°, and 74.2040° corresponding to the crystal planes of (111), (200), (220), and (311), according to the standard cards No. 96-900-8749. As shown in table (1), the inert-planer distances (d_{hkl}) were calculated according to Bragg's law [23], while the crystallite size determine according to Scherrer's formula [24]. In general the crystallite size reduced after N-doping. The result agree with previous studies [25,26].

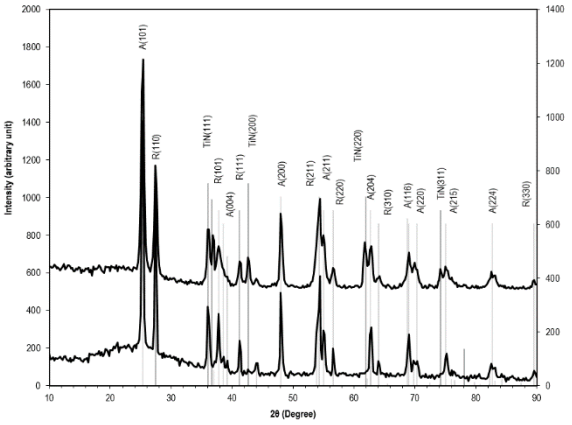

Fig. (1) XRD patterns for TiO_2 thin film (a) and TiO_2:TiN composite thin film (b) prepared by reactive DC sputtering

Figure (2) shows the FE-SEM images for the surface of TiO_2 and TiN/ TiO_2 thin films. There is a difference in the particle size between samples. The TiO_2 thin film appeared as nanoparticles with irregular shapes, sizes aggregate to each other and average particle size of 47.44nm (Fig. 2a). The TiO_2/TiN sample appeared as nearly uniform spherical and average particle size of 30.23nm in Fig. (2b). The average particle diameter significantly decreased due to the difference in growth. Such changes may enhance the applicable in photo catalytic applications.

Figure (3) and table (2) show the analysis of energy-dispersive x-ray spectroscopy (EDS) for TiO_2 and TiO_2:TiN thin films, which based on that each element has a unique atomic spectra after x-ray excitation. The measured shows many peaks corresponding to emission lines for titanium (Ti) and oxygen (O). The peaks intensities varies according to their existence in the samples. Additional peak corresponding to N_2 appeared in TiO_2:TiN samples indicate form new nanocomposite. The EDS map shown next to the patterns indicate the homogeneity distribution of the deposited elements.

 ISSN (print) 1813-2065, (online) 2309-1673

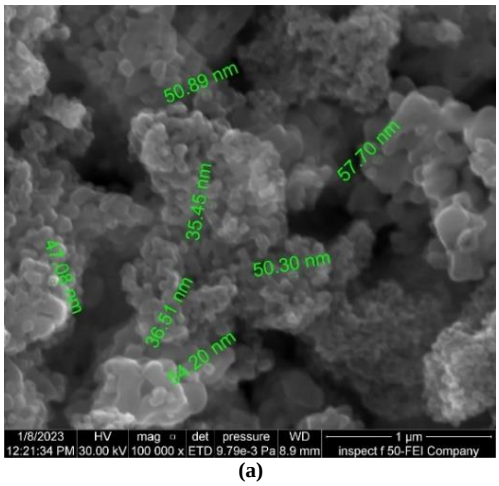

(a)

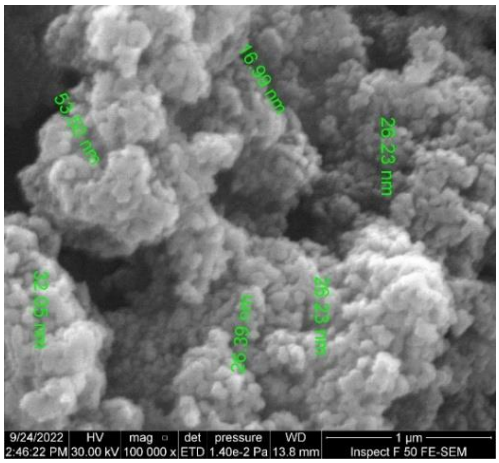

(b)

Fig. (2) SEM images for TiO_2 thin film (a) and TiO_2:TiN composite thin film (b) prepared by reactive DC sputtering

Table (2) Elements and their weights in EDS spectra for TiO_2 and TiO_2:TiN nanocomposites prepared in this work

	Element	Atomic %	Weight %
TiO_2	C	8.0	3.2
	O	46.6	24.7
	Ti	45.4	72.1
TiO_2:TiN	C	16.1	7.9
	N	9.7	5.6
	O	45.0	29.4
	Ti	29.2	57.1

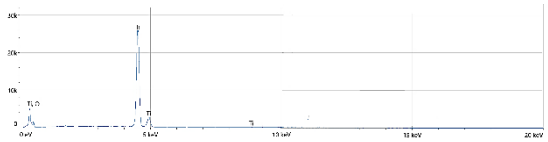

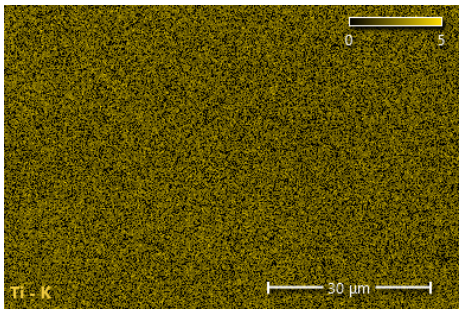

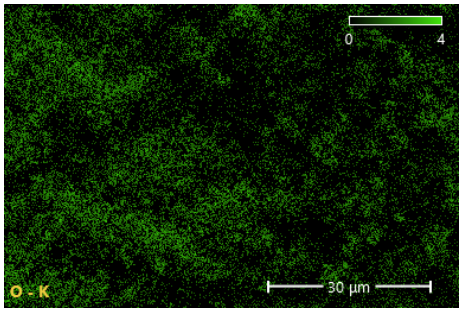

(a)

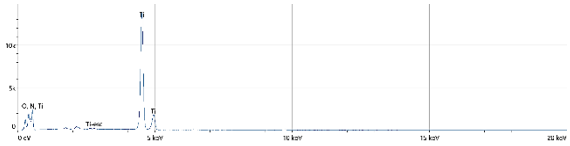

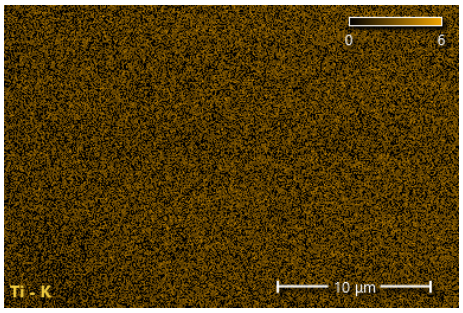

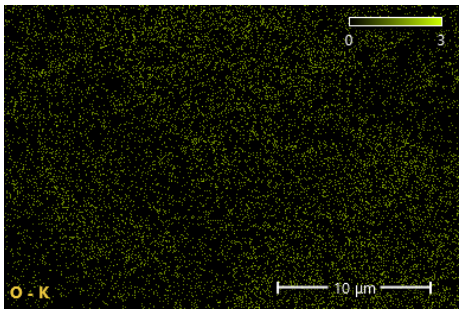

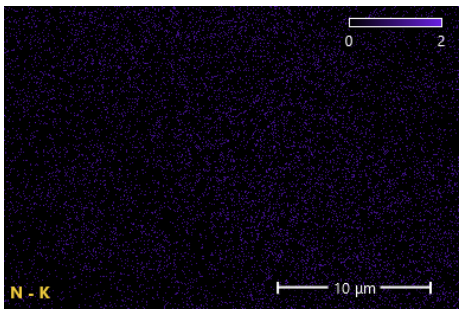

(b)

Fig. (3) EDS analysis and EDS map for TiO_2 thin film (a) and TiO_2:TiN composite thin film (b) prepared by reactive DC sputtering

The FTIR patterns for TiO_2 and TiO_2:TiN nanocomposite samples were shown in Fig. (5) and table (3). For the TiO_2, the band at around 3420 cm^{-1} in is attributed to hydroxel group. The C-H stretch appeared at 2987.24 corresponding to adsorbed carbonel group on the sample surface. A band at around 655.22 cm^{-1} which is represent of TiO_2

matrixes [27]. While a weak band at 423.23 Ti-O corresponding to rutile structure [28]. Additional band appeared at 1587.00 cm^{-1} corresponding to intermediate phase of Ti-OH causing defect sites in the TiO_2 matrix. Addition N_2 cause appearance of new bands, and some bands are shifted. The band at 1421.68 cm^{-1} corresponding to N-H band. The bands at 1134.27, 1041.96 and 1008.39 cm^{-1} attributed to Ti-N band for TiN phase. The band at 920.28 cm^{-1} may attribute to NO for intermediate nitride phases. The shoulder band at 540.56 cm^{-1} corresponding to Ti-O-Ti vibration [29,30].

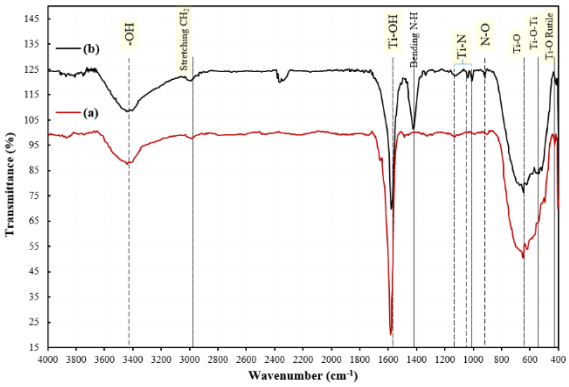

Fig. (4) FTIR analysis for TiO_2 thin film (a) and TiO_2:TiN composite thin film (b) prepared by reactive DC sputtering

Table (3) FTIR bands for TiO_2 and TiO_2:TiN composite thin film prepared by reactive DC sputtering

Band Type	TiO_2	20% N_2
O-H	3420.14	3435.66
C-H stretch	2987.24	2993.01
Ti-OH	1587.00	1576.92
N-H bending	-	1421.68
Ti-N	-	1134.27
	-	1041.96
	-	1008.39
N-O	-	920.28
Ti-O	655.22	643.36
Ti-O-Ti	-	540.56
Ti-O rutile	423.23	416.78

4. Conclusions

Titanium dioxide (TiO_2) and Titanium dioxide: Titanium nitride (TiO_2:TiN) nanocomposite thin film were successfully deposited by a dc reactive magnetron sputtering technique from a titanium target. The structural, morphological, and optical properties of the TiO_2 and TiO_2:TiN samples indicate the successful prepared new nanocomposite and the diagnosis techniques show the distinct variations in thin film properties after adding N_2. The results of the TiO2:TiN thin film prepared by reactive-DC sputtering were quite reasonable compared to the literature using other techniques, and the nanocomposite effect can enhance the photocatalytic activity.

References

[1] M. Fang et al., "Hierarchical nanostructures: design for sustainable water splitting", *Adv. Energy Mater.*, 7 (2017) 1700559.

[2] S. Reghunath, D. Pinheiro and S. Devi KR, "A review of hierarchical nanostructures of TiO_2: Advances and applications", *Appl. Sur. Sci. Adv.*, 3 (2021) 100063.

[3] C.H.A. Tsang et al., "Titanium oxide based photocatalytic materials development and their role of in the air pollutants degradation: Overview and forecast", *Environ. Int.*, 125 (2019) 200–228.

[4] F.J. Al-Maliki, O.A. Hammadi and E.A. Al-Oubidy, "Optimization of Rutile/Anatase Ratio in Titanium Dioxide Nanostructures prepared by DC Magnetron Sputtering Technique", *Iraqi J. Sci.*, Special Issue (2019) 91-98.

[5] R.M. Abdullah, "A Study the Effect of TiO_2 Nanoparticles Combination with Antibiotics and Plant extracts Against Some Gram Negative Bacteria", *Baghdad Sci. J.*, 13(3) (2016) 425-434.

[6] F.J. Al-Maliki, M.A. Al-Rubaiy, "Synthesis and study the concentration effect on the photocatalytic activity of titania nanoparticles as anti-bactria using reactive magnetron sputtering technique", *Opt. Quantum Electron.*, 54 (2022) 377.

[7] M.A. Ameen, A.J. Kadhum and A.A. Baker, "Annealing Effect on the phase Transformation in Sol-Gel Derived Titania Nanostructures", *Baghdad Sci. J.*, 8(2) (2011) 503-508.

[8] D. Reyes-Coronado et al., "Phase-pure TiO_2 nanoparticles: anatase, brookite and rutile", *Nanotechnology*, 19 (2008) 145605.

[9] M. Shahiduzzaman et al., "Spray Pyrolyzed TiO_2 Embedded Multi-Layer Front Contact Design for High-Efficiency Perovskite Solar Cells", *Nano-Micro Lett.*, 13 (2021) 36.

[10] O.A. Hamadi, "The Fundamentals of Plasma-Assisted CVD Technique Employed in Thin Films Production", *Iraqi J. Appl. Phys. Lett.*, 1(2) (2008) 3-8.

[11] Q. Zheng, X. Zhang and X. Zhou, "Experimental research on titanium dioxide nanofluid in vacuum flash evaporation", *Int. J. Energy Res.*, 44 (2020) 6035-6048.

[12] S.C. Ray et al., "Temperature-Dependent Electronic Structure of TiO_2 Thin Film Deposited by the Radio Frequency Reactive Magnetron Sputtering Technique: X-ray Absorption Near-Edge Structure and X-ray Photoelectron Spectroscopy", *J. Phys. Chem. C*, 126 (2022) 8947-8952.

[13] L. Mekala et al., "Effect of Oxygen Flow Rate on Surface Morphology and Optical Properties of Reactive DC Magnetron Sputtered TiO_2 Thin Films", *Appl. Mech. Mater.*, 903 (2021) 51-56.

[14] "Deposition Technologies" in Hand. Depos. Technol. Film. Coat., Elsevier (2010) 1-31.

[15] B. Huber et al., "Nanocrystalline anatase TiO_2

 ISSN (print) 1813-2065, (online) 2309-1673 PRINTED IN IRAQ

thin films: preparation and crystallite size-dependent properties", *Thin Solid Films*, 472 (2005) 114-124.

[16] W. Naffouti et al., "Structural, morphological and optical properties of TiO_2:Mn thin films prepared by spray pyrolysis technique", *J. Mater. Sci. Mater. Electron.*, 27 (2016) 4622-4630.

[17] S.J. Armaković, M.M. Savanović and S. Armaković, "Titanium Dioxide as the Most Used Photocatalyst for Water Purification: An Overview", *Catalysts*, 13 (2022) 26.

[18] A.Q. Abd Allah, H.S. Hussain and K.S. Mohan, "The effect of Gamma radiation on The Dielectric Properties of SiO_2/Ep:TiO_2/Ep Nanocomposite", *Iraqi J. Sci.*, 58(2B) (2022) 843-847.

[19] C. Thambiliyagodage, "Activity enhanced TiO_2 nanomaterials for photodegradation of dyes - A review", *Environ. Nanotechnol. Monit. Manag.*, 16 (2021) 100592.

[20] B. Liu, L. Wen and X. Zhao, "The structure and photocatalytic studies of N-doped TiO_2 films prepared by radio frequency reactive magnetron sputtering", *Sol. Energy Mater. Sol. Cells.*, 92 (2008) 1-10.

[21] E.A. Al-Oubidy and F.J. Kadhim, "Photocatalytic activity of anatase titanium dioxide nanostructures prepared by reactive magnetron sputtering technique", *Opt. Quantum Electron.*, 51 (2019) 23.

[22] S.I. Sharhan and I.M. Ibrahim, "Fabrication and Characterization of Hybrid MEH-PPV/TiO_2 for Photodetector", *Iraqi J. Sci.*, 60(4) (2019) 754-761.

[23] B. Shanmuga Priya et al., "Synthesis, characterization and photocatalytic activity of pure and Zn-doped In_2O_3 nanostructures", *J. Mater. Sci. Mater. Electron.*, 28 (2017) 12784-12794.

[24] W.H. Bragg and W.L. Bragg, "X-Rays and Crystal Structure", G. Bell and Sons, Ltd. (London, 1918).

[25] F. Li et al., "Sensors and Actuators B : Chemical Coaxial electrospinning heterojunction SnO_2/Au-doped In_2O_3 core-shell nanofibers for acetone gas sensor", *Sens. Actuat. B: Chem.*, 252 (2017) 822-830.

[26] F.J. Kadhim, O.A. Hammadi and N.H. Mutesher, "Photocatalytic activity of TiO_2/SiO_2 nanocomposites synthesized by reactive magnetron sputtering technique", *J. Nanophotonics*, 16 (2022) 026005–1–10.

[27] O.A. Hammadi, F.J. Al-Maliki and E.A. Al-Oubidy, "Photocatalytic activity of nitrogen-doped titanium dioxide nanostructures synthesized by DC reactive magnetron sputtering technique", *Nonl. Opt. Quantum Opt.*, 51 (2019) 67-78.

[28] C. Afonso et al., "Optical, structural, morphological and chemical properties of doped TiO_2 nanoparticles with $FeCl_3$", *J. Phys. Conf. Ser.*, 2407 (2022) 012001.

[29] P. Kumar et al., "Noble Metal Free, Visible Light Driven Photocatalysis Using TiO_2 Nanotube Arrays Sensitized by P-Doped C_3N_4 Quantum Dots", *Adv. Opt. Mater.*, 8 (2020) 1901275.

[30] R. Singh, M. Gupta and S.K. Mukherjee, "Effect of Ag layer thickness on optical and electrical properties of ion-beam-sputtered TiO_2/Ag/TiO_2 multilayer thin film", *J. Mater. Sci. Mater. Electron.*, 33 (2022) 6942-6953.

Table (1) XRD peaks parameters for TiO_2 and TiO_2:TiN composite thin film prepared by reactive DC sputtering

N_2 %	2θ (Deg)	FWHM (Deg)	d_{hkl} (Å)	C.S. (nm)	hkl	Phase	Card No.
0%	25.3983	0.4355	3.5040	18.7	(101)	Anatase	96-900-9087
	27.4171	0.4354	3.2504	18.8	(110)	Rutile	96-900-7532
	36.0069	0.4750	2.4923	17.6	(101)	Rutile	
	37.0361	0.4355	2.4254	19.2	(103)	Anatase	96-900-9087
	37.8278	0.3562	2.3764	23.6	(004)	Anatase	
	41.1925	0.4751	2.1897	17.9	(111)	Rutile	96-900-7532
	48.0010	0.4750	1.8938	18.3	(200)	Anatase	96-900-9087
	54.4137	0.6729	1.6848	13.3	(105)	Anatase	
	55.0866	0.4354	1.6658	20.6	(211)	Anatase	
	56.6304	0.4750	1.6240	19.0	(220)	Rutile	96-900-7532
	62.8055	0.5145	1.4784	18.1	(204)	Anatase	96-900-9087
	64.0327	0.4750	1.4530	19.7	(310)	Rutile	96-900-7532
	69.0203	0.5938	1.3596	16.2	(116)	Anatase	96-900-9087
	70.3266	0.7521	1.3375	12.9	(220)	Anatase	
	75.1954	0.5937	1.2626	16.9	(215)	Anatase	
	82.6373	0.9896	1.1667	10.7	(224)	Anatase	
20%	25.3983	0.5541	3.5040	14.7	(101)	Anatase	
	27.4171	0.5146	3.2504	15.9	(110)	Rutile	96-900-7532
	36.0861	0.5146	2.4870	16.2	(101)	Rutile	
	36.8340	0.5320	2.4382	15.7	(111)	TiN	96-900-8749
	37.8278	0.7126	2.3764	11.8	(004)	Anatase	96-900-9087
	41.2716	0.5937	2.1857	14.3	(111)	Rutile	96-900-7532
	42.7363	0.7521	2.1141	11.3	(200)	TiN	96-900-8749
	48.0010	0.5542	1.8938	15.7	(200)	Anatase	96-900-9087
	54.3741	0.7125	1.6859	12.5	(105)	Anatase	
	55.0866	0.5542	1.6658	16.2	(211)	Anatase	
	56.6700	0.5938	1.6230	15.2	(220)	Rutile	96-900-7532
	62.0139	0.7125	1.4953	13.0	(220)	TiN	96-900-8749
	62.8055	0.5937	1.4784	15.7	(204)	Anatase	96-900-9087
	64.1118	0.6729	1.4514	13.9	(310)	Rutile	96-900-7532
	69.0203	0.5542	1.3596	17.4	(116)	Anatase	96-900-9087
	69.9703	0.7521	1.3435	12.9	(220)	Anatase	
	74.2040	0.5435	1.2769	18.3	(311)	TiN	96-900-8749
	75.0371	0.8313	1.2648	12.1	(215)	Anatase	96-900-9087
	82.6769	0.9500	1.1662	11.1	(224)	Anatase	

 ISSN (print) 1813-2065, (online) 2309-1673

IRAQI JOURNAL OF APPLIED PHYSICS
Vol. 19, No. 3A, July-August 2023, pp. 55-58

Zahraa H. Zaidan[1]
Oday A. Hammadi[2]
Kasim H. Mahmood[1]

[1] *Department of Physics, College of Education for Pure Sciences, Tikrit University, Tikrit, IRAQ*
[2] *Department of Physics, College of Education, Al-Iraqia University, Baghdad, IRAQ*

Effect of Structural Phase on Photocatalytic Activity of Titanium Dioxide Nanoparticles

In this work, the effect of structure on the photocatalytic activity of titanium dioxide nanoparticles for the degradation of methylene blue dye in aqueous solution was introduced. The titanium dioxide nanoparticles were prepared by two different methods (solvothermal and dc reactive sputtering) with three different structures (anatase only, anatase:rutile with 2:1 and 1:1). According to the obtained results, the TiO_2 nanoparticles prepared by solvothermal method showed better photocatalytic activity than the other samples prepared by dc reactive sputtering. The solvothermal method can be described as a green method to prepare nanoparticles as photocatalyst for environmental and biomedical applications.

Keywords: Photocatalytic activity; Titanium dioxide; Nanoparticles; Structural phase
Received: 04 April 2023; **Revised:** 05 May 2023; **Accepted:** 12 May 2023

1. Introduction

Photocatalysts are classified into two categories: homogeneous and heterogeneous photocatalyst, Homogeneous photocatalysts are dispersed in the same phase as the reactants in the presence of light. The heterogeneous photocatalysts are in a different phase than the reactants, separated from them by a phase boundary under light [1]. Most common heterogeneous photocatalysts are transition metal oxides and semiconductors, which have unique characteristics. Unlike the metals which have a continuum of electronic states, semiconductors possess a void energy region where no energy levels are available to promote recombination of electrons and holes produced by photoactivation in the solid [2].

Crystallinity is an important factor to be considered in the optimization of the photodegradation efficiency. It has been shown that amorphous TiO_2 has negligible photodegradation efficiency compared with TiO_2 of high crystallinity. The low efficiency of amorphous TiO_2 is caused by the high recombination rate of electrons and holes due to the large amount of defects [3,4].

The primary criteria for an efficient semiconductor photocatalyst is that the redox potential of the charge couple, *i.e.*, e^-/h^+, lies within the band gap domain of the photocatalyst. The energy level at the bottom of conduction band determines the reducing ability of photoelectrons, while the energy level at the top of valence band determines the oxidizing ability of photogenerated holes [5]. The internal energy scale is given on the left for comparison to normal hydrogen electrode (NHE). The positions are derived from the flat band potentials in a contact solution of aqueous electrolyte at pH equal to 1. The pH of the electrolyte solution influences the band edge positions of the various semiconductors compared to the redox potentials for the adsorbate [6].

TiO_2 is close to be an ideal photocatalyst and the benchmark for photocatalysis performance. TiO_2 is cheap, photostable in solution and nontoxic. Its holes are strongly oxidizing and redox selective. For these reasons, several novel heterogeneous photocatalytic reactions have been reported at the interface of illuminated TiO_2 photocatalyst, and TiO_2-based photocatalysis has been researched exhaustively for environmental cleanup applications. The single drawback is that it does not absorb visible light [7]. To overcome this problem, several methods including dye sensitization, doping, coupling and capping of TiO_2 are proposed.

In this work, the photocatalytic activity of three samples of TiO_2 nanoparticles different in their structures was introduced and compared. These nanoparticles were prepared by two different methods; solvothermal and dc reactive sputtering. The photocatalytic activity was studied as a function of photodegradation methylene blue dye in aqueous solution.

2. Experimental Part

Two methods were used in this work to prepare titanium dioxide (TiO_2) nanoparticles. In the first method, solvothermal method, the TiO_2 nanoparticles were synthesized from the titanium isopropoxide and banana peels. The synthesized nanopowder was polycrystalline and containing both anatase and rutile phases (1:1) of TiO_2, with minimum nanoparticle size of 25.41, and good structural purity. For more details on this work, see reference [8]. In the second method, dc reactive magnetron sputtering, a highly-pure titanium sheet was sputtered in presence of $Ar:O_2$ gas mixture inside a vacuum chamber at gas pressure of 0.5mbar and discharge current of 40mA to deposit TiO_2 thin films on glass substrates. The deposited

films were containing both rutile and anatase phases of TiO_2. In order to deposit TiO_2 films with only anatase phase, a heat sink was placed under the substrate to avoid the thermal transition of anatase into rutile phase. For more details on this technique, see references [9-14]. The nanopowder was extracted from the tin film samples by the conjunctional freezing-assisted ultrasonic extraction method [15].

The photocatalytic activity of the prepared TiO_2 nanoparticles was determined by monitoring the degradation of the methylene blue (MB) dye in aqueous suspensions containing TiO_2 nanopowders under UV-radiation exposure. A 50 mL of aqueous suspension was prepared by completely dissolving 0.0159 gm of the MB dye in the deionized water. The MB dye placed in a quartz tube with TiO_2 nanopowder and stirred in the dark (without UV-radiation exposure) for one hour to stabilize the adsorption of the MB dye over the surface of TiO_2 nanoparticles.

The aqueous suspension was then exposed to the UV radiation; whose wavelength is in the range 300-410 nm. The UV radiation source was placed at a distance of 10 cm from the quartz tube. Following UV radiation exposure, 3 mL of aqueous suspension was taken out of the test chamber after each 30 min of UV-radiation exposure to record the absorption spectrum.

The intensity of the main absorption peak (A) of the MB dye solution was taken as a measure of the residual MB dye concentration (C). The UV-visible absorption spectrum of the MB dye solution, without the addition of TiO_2 nanopowder and the UV-radiation exposure, was also recorded as a reference spectrum corresponding to the initial MB dye concentration (C_0). The normalized residual MB dye concentration was calculated using the following relationship [16]:

$$\left(\frac{C}{C_O}\right)_{MB} = \left(\frac{A_{time=t}}{A_{time=0}}\right)_{656\,nm} \quad (1)$$

where $A_{time=0}$ is the initial intensity of main absorption peak located at 656 nm, $A_{time=t}$ is the intensity after exposure time of t, C_0 is the initial concentration of MB dye before adding the TiO_2 nanoparticles to the solution, and C is the residual concentration of MB dye after exposure time (t)

It is observed that the kinetics of the photocatalytic activity is measured in terms of the degradation of the MB dye.

3. Results and Discussion

Figure (1) shows the solution samples prepared in this work after 30 min of irradiation with UV source. The effect of catalytic activity of TiO_2 nanoparticles on the degradation of the MB dye solution is generally clear. However, slight differences can be observed due to the structure of these nanoparticles. Also, the degradation of the MB dye solution is increased with irradiation time.

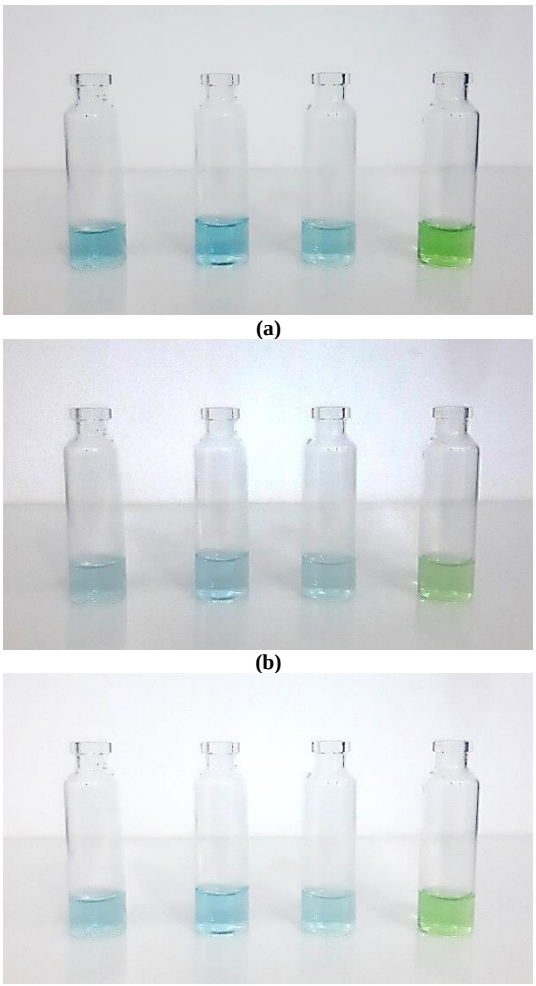

(a)

(b)

(c)

Fig. (1) Prepared solution samples (a) before irradiation, (b) after 30min irradiation, and (c) after 120min irradiation (from left to right: MB with (2:1) TiO_2 NPs, MB with (1:1) TiO_2 NPs, MB with anatase TiO_2 NPs, and MB only)

Figure (2) shows the absorbance decay of methylene blue (MB) dye with UV irradiation time in presence of anatase TiO_2 nanoparticles in the MB solutions. It shows that after two hours, the absorbance was decreased to about 72% of its initial value soon after irradiation of the dye solution with UV radiation. This decrease is obviously attributed to the effect of anatase TiO_2 nanoparticles in the MB solution. The dye solution containing anatase:rutile (2:1) TiO_2 nanoparticles showed a decrease by 65% while the green-synthesized TiO_2 nanoparticles (1:1) showed 71% decrease in absorbance.

The packing factor (PF) concept was developed to evaluate inherently existing internal fields that can be used to rank the charge separation abilities among oxide materials. Due to the lower value of PF for anatase TiO_2 (0.6455) when compared to that of rutile TiO_2 (0.7045), the loosely packed structure of anatase TiO_2 is favorable for photocatalytic activity. However, the mixed-phase (1:1) TiO_2 nanoparticles can be better for the MB degradation. This may be attributed to the synergetic effect originated from the existence of both structural phases in the final sample.

 ISSN (print) 1813-2065, (online) 2309-1673

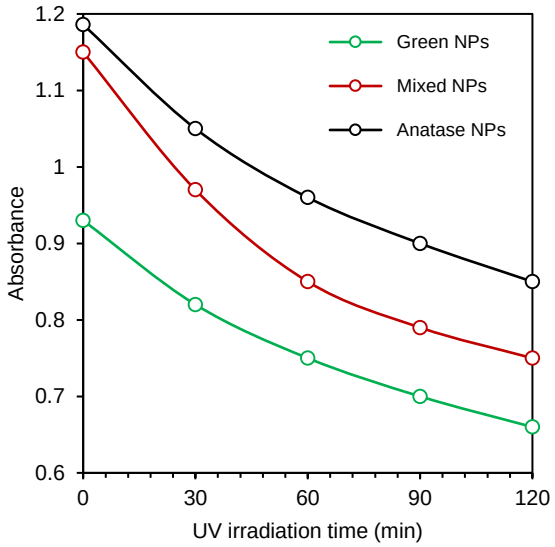

Fig. (2) Absorbance decay of methylene blue (MB) dye with UV irradiation time in presence of TiO_2 nanoparticles in the MB solutions

Typical variation in the normalized residual MB dye concentration as a function of UV radiation exposure time for the TiO_2 nanoparticles is presented in Fig. (3). It is observed that the kinetics of the photocatalytic activity, measured in terms of the degradation of the MB dye, is enhanced by about 33% for the anatase TiO_2 nanoparticles, 34% for the green synthesized nanoparticles, and 43% for the mixed-phase nanoparticles. The values of the apparent first-order reaction rate constant (k_{app}) were obtained using the data presented in Fig. (2). The k_{app} values for the (1:1), (2:1) and anatase TiO_2 nanoparticles are obtained from the slopes of these fitted straight lines to be $2.8x10^{-3}$, $3.5x10^{-3}$ and $2.7x10^{-3}$ min^{-1}, respectively, which reflects the rate of degradation of the photocatalyst against the pollutant.

The photocatalytic activity of the TiO_2 nanoparticles was introduced by monitoring the degradation of methylene blue (MB) dye in an aqueous solution containing these nanoparticles under UV-radiation exposure. The normalized residual MB dye concentration [$(C/C_0)_{MB}$] was given by Eq. (1).

The kinetics of the photocatalytic activity measured in terms of the degradation of the MB dye are observed. So, after this process, the mixed-phase (2:1) TiO_2 nanoparticles showed much more degradation than the green-synthesized (1:1) and anatase TiO_2 nanoparticles, as shown in Fig. (4).

This can be ascribed to a strong electronic interaction between the rutile and anatase TiO_2 structures, which may result in an improvement in the kinetics of the photocatalytic activity of mixed-phase (2:1) TiO_2 nanostructures. A photocatalysis experiment was also carried out in the absence of TiO_2 nanoparticles as photocatalysts to confirm the stability of MB dye in an aqueous solution under continuous exposure by UV radiation. Under this condition, the initial concentration (C_0) of MB dye remained constant even after irradiation time of 210 min.

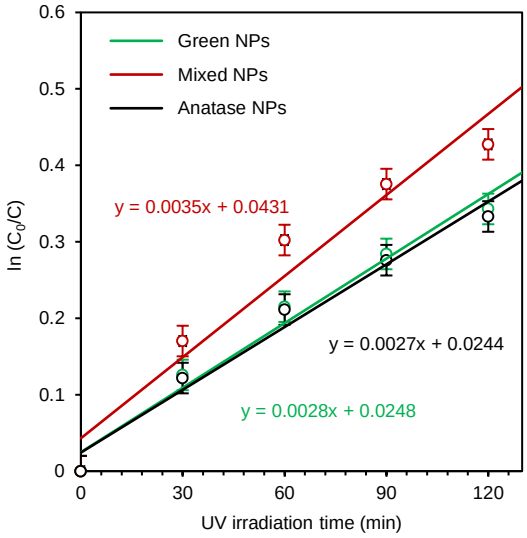

Fig. (3) Typical variation in the normalized residual MB dye concentration as a function of UV radiation exposure time for the TiO_2 nanoparticles

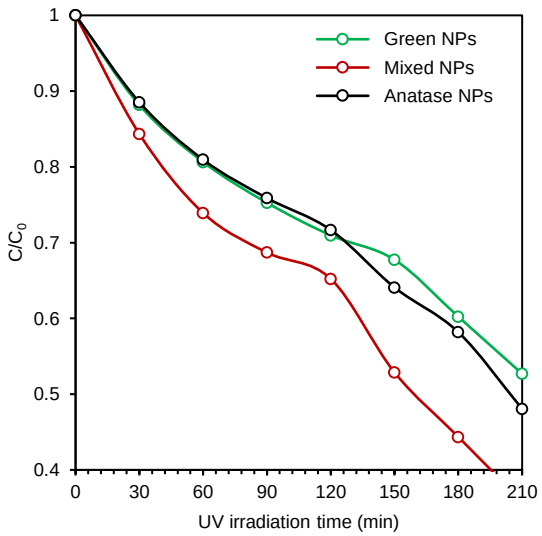

Fig. (4) The photocatalytic activity of the TiO_2 nanoparticles in MB dye aqueous solution under UV-radiation exposure

4. Conclusion

In this work, the effect of structure on the photocatalytic activity of titanium dioxide nanoparticles for the degradation of methylene blue dye in aqueous solution was introduced. The titanium dioxide nanoparticles were prepared by two different methods (solvothermal and dc reactive sputtering) with three different structures (anatase only, anatase:rutile with 2:1 and 1:1). According to the obtained results, the TiO_2 nanoparticles prepared by solvothermal method showed lower photocatalytic activity than the mixed-phase (2:1) TiO_2 nanoparticles prepared by dc reactive sputtering but better than the anatase TiO_2 nanoparticles prepared by

dc reactive sputtering. The solvothermal method can be described as a green method to prepare nanoparticles as photocatalysts for environmental and biomedical applications.

References

[1] S. Rehman et al., "Strategies of making TiO_2 and ZnO visible light active", *J. Hazard. Mater.*, 170(2-3) (2009) 560-569.
[2] A.L. Linsebigler, G. Lu, and J.T. Yates, "Photocatalysis on TiO_2 Surfaces: Principles, Mechanisms, and Selected Results", *Chem. Rev.*, 95(3) (1995) 735-758.
[3] N.T. Nolan, "Sol-Gel Synthesis and Characterization of Novel Metal Oxide Nano-materials for Photocatalytic Applications", Ph.D. thesis, Dublin Institute of Technology, Ireland (2010).
[4] K. Eufinger, "Effect of deposition conditions and doping on the structure, optical properties and photocatalytic activity of d.c. magnetron sputtered TiO_2 thin films", Ph.D. thesis, Ghent University, Belgium (2007).
[5] O. Carp, C.L. Huisman and A. Reller, "Photoinduced reactivity of titanium dioxide", *Prog. Sol. Stat. Chem.*, 32 (2004) 33-117.
[6] O.A. Hammadi, F.J. Kadhim and E.A. Al-Oubidy, "Photocatalytic Activity of Nitrogen-Doped Titanium Dioxide Nanostructures Synthesized by DC Reactive Magnetron Sputtering Technique", *Nonl. Opt. Quantum Opt.*, 51(1-2) (2019) 67-78.
[7] E.A. Al-Oubidy and F.J. Al-Maliki, "Photocatalytic activity of anatase titanium dioxide nanostructures prepared by reactive magnetron sputtering technique", *Opt. Quantum Electron.*, 51(1-2) (2019) 23.
[8] Z.H. Zaidan, K.H. Mahmood and O.A. Hammadi, "Using Banana Peels for Green Synthesis of Mixed-Phase Titanium Dioxide Nanopowders", *Iraqi J. Appl. Phys.*, 18(4) (2022) 27-30.
[9] E.A. Al-Oubidy and F.J. Al-Maliki, "Effect of Gas Mixing Ratio on Energy Band Gap of Mixed-Phase Titanium Dioxide Nanostructures Prepared by Reactive Magnetron Sputtering Technique", *Iraqi J. Appl. Phys.*, 14(4) (2018) 19-23.
[10] F.J. Al-Maliki, O.A. Hammadi and E.A. Al-Oubidy, "Optimization of Rutile/Anatase Ratio in Titanium Dioxide Nanostructures prepared by DC Magnetron Sputtering Technique", *Iraqi J. Sci.*, 60(special issue) (2019) 91-98.
[11] F.J. Al-Maliki and E.A. Al-Oubidy, "Effect of gas mixing ratio on structural characteristics of titanium dioxide nanostructures synthesized by DC reactive magnetron sputtering", *Physica B: Cond. Matter*, 555 (2019) 18-20
[12] F.J. Al-Maliki, O.A. Hammadi, B.T. Chiad and E.A. Al-Oubidy, "Enhanced photocatalytic activity of Ag-doped TiO_2 nanoparticles synthesized by DC Reactive Magnetron Co-Sputtering Technique", *Opt. Quantum Electron.*, 52 (2020) 188.
[13] R.A.H. Hassan and F.T. Ibrahim, "Preparation and Characterization of Anatase Titanium Dioxide Nanostructures as Smart and Self-Cleaned Surfaces", *Iraqi J. Appl. Phys.*, 16(4) (2020) 13-18.
[14] M.A. Hameed, S.H. Faisal, R.H. Turki, "Characterization of Multilayer Highly-Pure Metal Oxide Structures Prepared by DC Reactive Magnetron Sputtering Technique", *Iraqi J. Appl. Phys.*, 16(4) (2020) 25-30
[15] O.A. Hammadi, "Production of Nanopowders from Physical Vapor Deposited Films on Nonmetallic Substrates by Conjunctional Freezing-Assisted Ultrasonic Extraction Method", *Proc. IMechE, Part N, J. Nanomater. Nanoeng. Nanosys.*, 232(4) (2018) 135-140.
[16] A. Zachariah et al., "Synergistic Effect in Photocatalysis As Observed for Mixed-Phase Nanocrystalline Titania Processed via Sol-Gel Solvent Mixing and Calcination", *J. Phys. Chem. C*, 112 (2008) 11345-11356.

 ISSN (print) 1813-2065, (online) 2309-1673 PRINTED IN IRAQ

IRAQI JOURNAL OF APPLIED PHYSICS
Vol. 19, No. 3A, July-August 2023, pp. 59-62

Green Synthesis and Characterization of Silver Nanoparticles for Biological Applications

Hala H. Ali
Farah T. Mohammed Noori

Department of Physics,
College of Science
University of Baghdad,
Baghdad, IRAQ

In this study, silver nanoparticles were biosynthesized using garlic extraction and their main structural characteristics were characterized. The x-ray diffraction (XRD) pattern showed four diffraction peaks at 32.10°, 38.34°, 45.68° and 77.59°, which match the silver crystalline planes of (111), (200), (220), and (311) planes, respectively. The field-emission scanning electron microscopy (FE-SEM) revealed that the prepared Ag NPs were agglomerated spheres. The energy-dispersive x-ray spectroscopy (EDX) showed reasonable structural purity of the prepared nanoparticles as a result of biosynthesis method. These results show can be considered promising for many applications, such as medicinal therapies, wastewater treatment, and other industries.

Keywords: Nanotechnology; Nanoparticles; Biosynthesis; Green synthesis
Received: 23 February 2023; **Revised:** 01 May 2023; **Accepted:** 08 May 2023

1. Introduction

Novel nanomaterials and nanoparticles represent the numerous potential scientific and technological uses of nanotechnology, a field that has just recently emerged as an academic discipline. Particles between (1 and 100 nm) in size are considered nanoparticles (NPs) [1,3]. Biomedicine, agriculture, pharmaceutics, textiles, food technology, catalysis, sensors, mechanics, electronics, and optics are just a few of the sectors that could benefit from their use, therefore they have involved a lot of attention from the scientific community. Silver, gold, zinc, cadmium sulfide, copper, iron, titanium dioxide, etc. are only a few of the many materials that can be found in nanoparticles [3-8]. Silver nanoparticles (Ag NPs) have been one of the most studied nanoparticles in recent decades [9-13] due to their would-be uses in biomedical science. These applications include their use as (an antibacterial, antifungal, antioxidant, anti-cancer, anti-inflammatory, drug delivery, wound dressing, biosensor, and biocatalyst) also used in Wastewater treatment, Wastewater is 99.9% water, with the materials that must be removed accounting for only 0.1 percent by volume. This solid substance is a mixture of feces, food particles, grease, oils, soap, salts, metals, detergents, plastic, sand, and grit. The organic fraction is primarily composed of proteins, carbohydrates, and fats [14]. Recent research indicates that green-produced silver nanoparticles have potent antibacterial, antioxidant, and anti-cancer properties [11-15].

These nanoparticles (Ag NPs) can be synthesized using a wide range of physical and chemical techniques, including chemical reactions, photochemical processes, thermal degradation of different silver compounds, electrochemical processes, radiation, and microwave-assisted methods [16]. Using poisonous substances, spending a lot of money, using a lot of labor-intensive equipment, and producing hazardous byproducts are the main downsides of these approaches [3,6,17]. Because of the limitations of physicochemical techniques, scientists are increasingly interested in biological methods for the green which are non-toxic, cheap, and eco-friendly instead of using pricey harmful chemicals, green synthesis makes use of natural substances such as reducing, capping, and stabilizing agents. The green production of bioactive nanoparticles [18-21] could make use of a wide variety of biological resources, including plants and plant components (roots, plants, fruit, etc.), bacteria, fungi, algae, etc. Antimicrobial properties and green production of silver nanoparticles utilizing plant extracts or microorganisms have received a lot of attention as of late. This global health dilemma is significant because multidrug-resistant bacteria are the root cause of many serious infectious illnesses.

2. 2. Material and Method

Introducing the morphology, size, shape, limpidness, and chemical appearance of the silver nanoparticles is a crucial step to achieve green synthesis. UV-visible spectrophotometry, x-ray diffraction (XRD), field-emission scanning electron microscopy (FE-SEM), and energy-dispersive x-ray spectroscopy (EDX) have been used to characterize green-synthesized silver nanoparticles. These tests showed that good results were obtained as the garlic plant extract was used for biosynthesis of silver

nanoparticles, which were then employed in a wide variety of medical uses.

Allium sativum (garlic) bulbs, sodium hydroxide (NaOH), distilled water, and silver nitrate ($AgNO_3$) were used as the raw and starting materials. They were supplied from the local market. The garlic cloves were peeled and washed with distilled water to remove any remaining debris and dirt. The aqueous extract was then set by pounding 10 g of garlic pieces with a pestle and mortar, then combining this mixture with 100 mL of distilled water. The extract was filtered using filtration paper and the resulting filtrate was stored in the refrigerator at 4 °C to be used later.

To neutralize the silver ions, an aqueous extract of garlic was produced using a full pipet and 100 mL of 2 mg $AgNO_3$ with the addition of 2 pieces of sodium hydroxide (NaOH) to balance the pH solution. A magnetic stirrer was used to continually agitate the reaction mixture at 650 rpm. After few seconds (less than 5 s), the colorless solution began to become yellow-brown, representing the creation of a silver colloid. After 15 minutes, the color saturation reached a maximum. The UV-Visible spectroscopy revealed this phenomenon to be occurring at 380 nm.

3. Results and Discussion

The main idea of this work is to prepare nanomaterials in a short time from plant extracts that are cheap and available in nature, using green synthesis, which is an environmentally friendly method that does not cause any pollution and gives good and fast results.

The first visible sign of the formation of silver nanoparticles is the change in color. In most cases, the synthesis of silver nanoparticles can be identified by the presence of a dark brown color in the reaction mixture. UV-visible spectrophotometry is then used to verify the formation of silver nanoparticles. In UV-visible spectrophotometry, the synthesized silver nanoparticles exhibit an absorption peak at 380 nm, as shown in Fig. (1). The size and form of biosynthesized silver nanoparticles can determine their absorption spectra [22].

In order to determine the crystalline structure of the synthesized nanoparticles, the XRD pattern shown in Fig. (2) was introduced. Four diffraction peaks can be clearly seen at 2θ of 32.10°, 38.34°, 45.68° and 77.59°, corresponding to the (111), (200), (220) and (311) crystalline surfaces of silver. This result confirmed the polycrystalline structure of the biosynthesized silver nanoparticles [18,23,24]. Ordinarily, other peaks seen in this pattern belong to other materials used in the synthesis process as the plant extract and precursor of the silver nanoparticles contain different elements and compounds. As the synthesized nanoparticles would be employed in some applications those not very sensitive to other materials than the silver nanoparticles, then this result can be accepted well. For the applications with high sensitivity to other materials in the final sample, additional purification methods may be required to obtain highly-pure silver nanoparticles. However, this may add cost, time and complexity to the synthesis process.

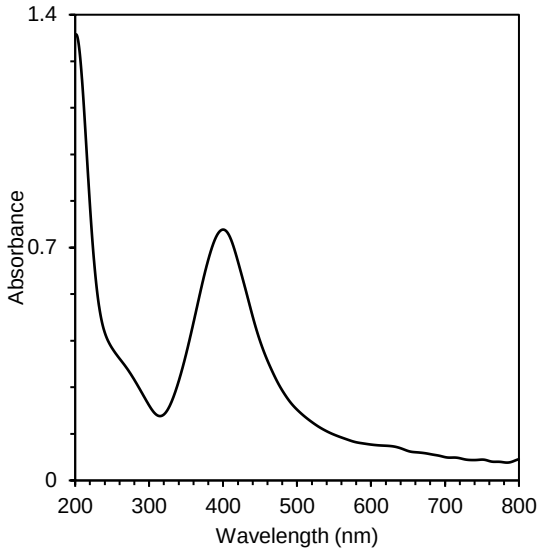

Fig. (1) UV-Visible absorption spectrum of silver nanoparticles biosynthesized in this work

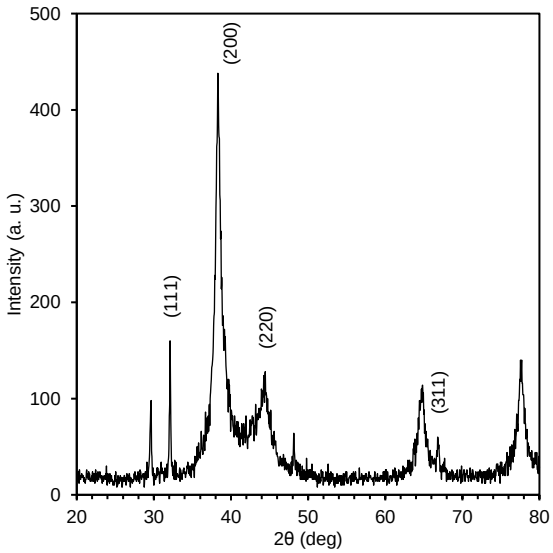

Fig. (2) XRD pattern of silver nanoparticles biosynthesized in this work

In order to introduce the surface morphology of the prepared silver nanoparticles, the FE-SEM was used, as shown in Fig. (3). The silver nanoparticles are shown to have spherical shapes with highly uniform distribution. The minimum particle size can be determined to be 23.21 nm. No aggregation is seen, which can be considered as an advantage of the synthesis method as the formed nanoparticles were sufficiently dispersed in the liquid preparation medium [19,25,26]. The EDX spectrum showed that no other elements were found in the final sample other than silver, which may show the reliability of

 ISSN (print) 1813-2065, (online) 2309-1673

the biosynthesis process used in this work to produce silver nanoparticles with reasonable purity.

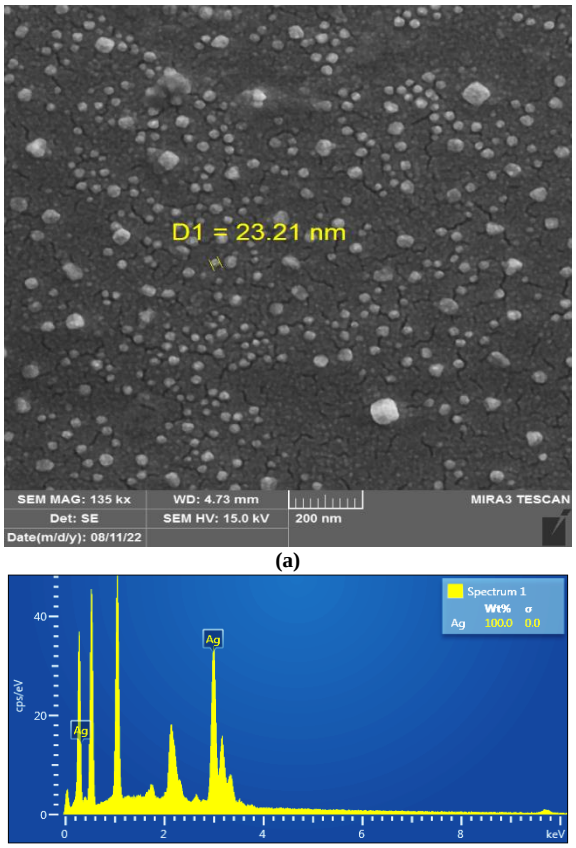

Fig. (3) FE-SEM microimage and EDX spectrum of silver nanoparticles biosynthesized in this work

4. Conclusion

Silver nanoparticles were synthesized by an environmentally friendly (green) biosynthesis method. This method includes the employment of garlic plant extract for the reduction of silver from silver nitrate aqueous solution. Microorganisms produce many main and minor metabolites that act as reducing agents, capping and stabilizing agents, enzymes, and amino acids in biomolecule production. This method is effective, simple and fast. The synthesized nanoparticles were polycrystalline and spherical shaped with no aggregation and minimum particle size of 23.21 nm. These nanoparticles showed an absorption peak at 380 nm, which gives them an ability to absorb the UV radiation when used in the practical application requiring the absorption in this region of electromagnetic spectrum. The silver nanoparticles synthesized in this work can be successfully employed in wastewater treatment and medical and medicinal applications, such as cancer treatment and drug delivery.

References

[1] R.K. Bachheti et al., "Biogenic fabrication of nanomaterials from flower-based chemical compounds, characterization, and their various applications: a review", *Saudi J. Biol. Sci.*, 27(10) (2020) 2551-2562.

[2] Z.H. Zaidan, Q.H. Mahmood and O.A. Hammadi, "Using Banana Peels for Green Synthesis of Mixed-Phase Titanium Dioxide Nanopowders", Iraqi J. Appl. Phys., 18(4) (2022) 27-30.

[3] A. Shahina, and Md.A. Huq, "Biologically rapid synthesis of silver nanoparticles by Sphingobium sp. MAH-11T and their antibacterial activity and investigation mechanisms against drug-resistant pathogenic microbes", *Artif. Cells, Nanomed. Biotech.*, 48(1) (2020) 672-682.

[4] R.A. Hamouda et al., "Synthesis and biological characterization of silver nanoparticles derived from the cyanobacterium Oscillatoria limnetic", *Sci. Rep.*, 9(1) (2019) 1-17.

[5] N. Kulkarni and U. Muddapur, "Biosynthesis of metal nanoparticles: a review", *J. Nanotech.*, 2014 (2014) Article ID 510246.

[6] P.G. Jamkhande et al., "Metal nanoparticles synthesis: An overview on methods of preparation, advantages and disadvantages, and applications", *J. Drug Del. Sci. Technol.*, 53 (2019) 101174.

[7] O.A. Hamadi, R.A. Markub and A.A.K. Hadi, "Heat-annealed enhanced-diffusion of silver in gallium arsenide", J Edu. Al-Mustansiriya Univ., 3 (2001) 35-44.

[8] O.A. Hamadi and K.Z. Yahiya, "Optical and electrical properties of selenium-antimony heterojunction formed on silicon substrate", *UoS J. Pure Appl. Sci.*, 4(2) (2007) 1-11.

[9] G.M. Saleh, "Green synthesis concept of nanoparticles from environmental bacteria and their effects on pathogenic bacteria", *Iraqi J. Sci.*, 61(6) (2020) 1289-1297.

[10] A.J. Haider, A.L. Abed and D.S. Ahmed, "Formation Silver Nanoparticles of Different Sizes Using Different Reductants with $AgNO_3$ Solution", *Iraqi J. Sci.*, 57(2B) (2016) 1203-1209.

[11] Md.A. Huq, "Green synthesis of silver nanoparticles using Pseudoduganella 61burnean MAHUQ-39 and their antimicrobial mechanisms investigation against drug-resistant human pathogens", *Int. J. Mol. Sci.*, 21(4) (2020) 1510.

[12] Ph.B.E. Kedi et al., "Eco-friendly synthesis, characterization, in vitro and in vivo anti-inflammatory activity of silver nanoparticle-mediated Selaginella measures aqueous extract", *Int. J. Nanomed.*, 13 (2018) 8537.

[13] N.E. El-Naggar, M.H. Hussein and A.A. El-Sawah, "Bio-fabrication of silver nanoparticles by phycocyanin, characterization, in vitro anticancer activity against breast cancer cell line and in vivo cytotoxicity", *Sci. Rep.*, 7(1) (2017) 10844.

[14] M.Q. Qader and Y.A. Shekha, "Using Microalga Scenedesmus quadricauda for the Improvement

of Municipal Wastewater Quality", *Iraqi J. Sci.*, 64(5) (2023) 2178-2188.
[15] F.J. Al-Maliki, O.A. Hammadi, B.T. Chiad and E.A. Al-Oubidy, "Enhanced photocatalytic activity of Ag-doped TiO_2 nanoparticles synthesized by DC Reactive Magnetron Co-Sputtering Technique", Opt. Quantum Electron., 52 (2020) 188.
[16] D.R. Ibraheem, N.N. Hussein and G.M. Sulaiman, "Antibacterial Activity of Silver Nanoparticles against Pathogenic Bacterial Isolates from Diabetic Foot Patients", *Iraqi J. Sci.*, 64(5) (2023) 2223-2239.
[17] S. Iravani et al., "Synthesis of silver nanoparticles: chemical, physical and biological methods", *Res. Pharmaceut. Sci.*, 9(6) (2014) 385.
[18] Sh. Akter et al., "Ecofriendly synthesis of silver nanoparticles by Terrabacter humi sp. Nov. and their antibacterial application against antibiotic-resistant pathogens", *Int. J. Mol. Sci.*, 21(24) (2020) 9746.
[19] Du. Juan, H. Singh and T.-H. Yi, "Antibacterial, anti-biofilm and anticancer potentials of green synthesized silver nanoparticles using benzoin gum (Styrax benzoin) extract", *Biopro. Biosys. Eng.*, 39 (2016) 1923-1931.
[20] N. Vigneshwaran et al., "Silver-protein (core-shell) nanoparticle production using spent mushroom substrate", *Langmuir*, 23(13) (2007) 7113-7117.
[21] H.Md. Amdadul, "Paenibacillus anseongense sp. Nov. a silver nanoparticle producing bacterium isolated from rhizospheric soil", *Cur. Microbiol.*, 77 (2020) 2023-2030.
[22] E. Tomaszewska et al., "Detection limits of DLS and UV-Vis spectroscopy in the characterization of polydisperse nanoparticles colloids", *J. Nanomater.*, 2013 (2013) 60-60.
[23] E. Ibrahim et al., "Green-synthesization of silver nanoparticles using endophytic bacteria isolated from garlic and its antifungal activity against wheat Fusarium head blight pathogen Fusarium graminearum", *Nanomater.*, 10(2) (2020) 219.
[24] J.M.M. Mohamed et al., "Superfast synthesis of stabilized silver nanoparticles using aqueous Allium sativum (garlic) extract and isoniazid hydrazide conjugates: molecular docking and in-vitro characterizations", *Molecules*, 27(1) (2021) 110.
[25] P. Singh et al., "Silver nanoparticles produced from Cedecea sp. Exhibit antibiofilm activity and remarkable stability", *Sci. Rep.*, 11(1) (2021) 1-13.
[26] Md.A. Huq, "Biogenic silver nanoparticles synthesized by Lysinibacillus xylanolytic MAHUQ-40 to control antibiotic-resistant human pathogens Vibrio parahaemolyticus and Salmonella Typhimurium", *Front. Bioeng. Biotech.*, 8 (2020) 597502.

 ISSN (print) 1813-2065, (online) 2309-1673

IRAQI JOURNAL OF APPLIED PHYSICS
EDITORIAL BOARD

COPYRIGHT RELEASE FORM
IRAQI JOURNAL OF APPLIED PHYSICS (IJAP)

We, the undersigned, the author/authors of the article titled

……
……
……
……
……
……
……

that is submitted to the Iraqi Journal of Applied Physics (IJAP) for publication, declare that we have neither taken part or full text from any published work by others, nor presented or published it elsewhere in any other journal. We also declare transferring copyrights and conduct of this article to the Iraqi Journal of Applied Physics (IJAP) after accepting it for publication.

The authors will keep the following rights:

1. Possession of the article such as patent rights.
2. Free of charge use of the article or part of it in any future work by the authors such as books and lecture notes after informing IJAP editorial board.
3. Republishing the article for any personal purposes of the authors after taking journal permission.

To be signed by all authors:

Signature:……..date: ……
Printed name: ……

Signature:……..date: ……
Printed name: ……

Signature:……..date: ……
Printed name: ……

Correspondence author:……..……...……...
……
Address:……..……
……
Telephone:……..……..email: ……

Note: Complete and sign this form and mail it to the below address with your finally revised manuscript

The Iraqi Journal of Applied Physics
P. O. Box 88052, Baghdad 12631, IRAQ
www.iraqiphysicsjournal.com
Email: info@iraqiphysicsjournal.com
Email: editor_ijap@yahoo.co.uk
Email: ijap.editor@gmail.com

IRAQI JOURNAL OF APPLIED PHYSICS

Volume (19) Issue (3A) July-August 2023

CONTENTS